Advancements of Shutdown Dose Rate Analysis Tools for Accelerator-Driven Systems

by

Nancy Granda Duarte

Dissertation submitted in partial fulfillment of
the requirements for the degree of

Doctor of Philosophy

(Nuclear Engineering and Engineering Physics)

at the

UNIVERSITY OF WISCONSIN–MADISON

2024

Date of oral examination: 2024-08-26

Thesis Committee:

Paul P.H. Wilson, Professor, Engineering Physics
Adrian Couet, Professor, Engineering Physics
Ben Lindley, Professor, Engineering Physics
Bryan Bednarz, Professor, Medical Physics
Franz X. Gallmeier, SNS Staff Member, Oak Ridge National Lab

Dedicated to my parents, Sara and Miguel.

Acknowledgments

I would like to express my gratitude to the many people whose support, guidance, and encouragement have been pivotal in helping me navigate and complete my Ph.D. journey.

First, I would like to thank my parents, Sara and Miguel, whose love and memories I will always cherish. Though they are no longer with me, their presence in my life is ever felt. To my second set of parents, Robyn and Eddie, who came later in life, thank you for your guidance and encouragement to attend college and pursue a career in STEM. To my siblings, whose love and support have always been the foundation of my strength.

To my partner, Jose, for his steadfast support and love throughout every stage of this journey. Your presence has been a constant source of comfort and motivation.

I would like to extend my sincerest thanks to my advisor, Professor Paul Wilson, for his unwavering support, invaluable expertise, and thoughtful guidance throughout my Ph.D. Thank you for your advice, mentorship, and belief in my work, which was instrumental in shaping the direction of my research and fostering my academic growth.

I am deeply grateful for the support and camaraderie of the CNERG team. Our shared conversations, research discussions, and moments of joy outside the lab made this experience not only productive but deeply rewarding. I want to give special thanks to YoungHui Park for his immense patience throughout the years when introducing me to new Nuclear Engineering topics and helping me with homework. His kindness will remain with me even in his absence.

Lastly, I would like to express my appreciation to my dissertation committee and the members of the Spallation Neutron Source team at Oak-Ridge National Lab for their feedback, guidance, and support throughout this process. Your collective wisdom has been invaluable to the completion of this dissertation.

Contents

List of Tables

List of Figures

Abstract

In accelerator-driven systems, high-energy charged particles initiate nuclear reactions in target areas, producing secondary particles, including high-energy neutrons. High-energy neutrons interact with the system's components, activating their materials and producing unstable radionuclides. These unstable radionuclides release photons as they decay, which can persist even after the system has been shut down. It is important to quantify the SDR from these photons as a function of space and time after shutdown to ensure the safety of maintenance operators. The SDR can be calculated computationally using the R2S method. The R2S workflow for accelerator-driven systems currently uses physics models to quantify interactions in energy regions beyond the domain of nuclear data libraries. A special tally in MCNP collects the production and destruction rates at the resolution of a volumetric cell from physics models during the first transport. The use of this tally means that the resolution for the R2S calculation is limited to the size of a volume. Analysts often have to divide geometric volumes into smaller volumes to gain more detail in R2S calculation. Dividing the geometry into smaller pieces can be cumbersome, depending on its complexity and the expertise of the analyst.

The complexity of accelerator-driven systems necessitates the use of MCNP for transport, which has a statistical uncertainty associated with it. This uncertainty becomes greater when the problem has areas of high attenuation. To mitigate the high uncertainty, VR methods are often used. The current methods like the CADIS or FW-CADIS are only able to optimize the last transport step in an R2S calculation. Furthermore, these methods can only be applied to low neutron energies due to the lack of cross-section libraries. The MS-CADIS is another VR technique used to optimize the first transport step of a multi-step process. To optimize the neutron transport step in an R2S workflow, an adjoint neutron source is needed. The adjoint neutron source requires that T be defined. An analytical solution of T only exists under specific conditions. The GT-CADIS method defines an analytical solution for T under the SNILB criteria. If the SNILB criteria are violated, T becomes an approximation. The GT-CADIS method is currently implemented for use with fusion systems.

The work in this thesis aims to improve the R2S workflow for accelerator-driven systems in two ways. First, the R2S workflow is improved upon by adding meshing capability to the special tally used for collecting high-energy production and destruction rates. A full R2S workflow is developed, verified, and demonstrated. Second, an implementation of MS-CADIS for generating VR parameters for accelerator-driven systems is created. The high-energy GT-CADIS workflow provides a way to obtain T, taking into account the high-energy interactions outside the energy range of cross-section libraries. This work validates and demonstrates the high-energy GT-CADIS workflow. Promising results show that the application of high-energy GT-CADIS VR parameters to accelerator-driven systems can significantly reduce the computational resources needed to calculate the SDR.

Chapter 1

Introduction

During the operation of accelerator-driven systems, the nuclear reactions happening in the system produce high-energy particles, including high-energy neutrons. These high-energy particles can interact with other nuclei, including the system's components. The interaction with the high-energy particles can activate the components' materials and release high-energy photons, which can persist even after the system is shut down. These photons contribute to the dose rate and can negatively impact the health of the human body. Quantifying the dose rate is essential to keeping personnel safe when they come in close contact with the system, like during maintenance procedures. Quantifying the dose rate after system shutdown, also known as SDR, has traditionally been performed computationally, and workflows exist to aid the calculation. A methodology used to obtain the SDR for these systems is the R2S method [1], which requires separate neutron and photon transport simulations coupled with an activation calculation.

Current implementations of the R2S method used for SDR analysis of accelerator-driven systems rely on physics models during the primary radiation step to obtain information on interactions with charged particles and high-energy neutrons. Low-energy neutron interactions are described using tabulated cross-section data tables.

A special tally, RNUCS, collects the radionuclide production and destruction rates from the interactions of high-energy neutrons and other particles [2]. The use of this tally poses limitations to the workflow as the tally can only tally information on a volumetric cell. This subsequently means the photon emission density is averaged over a volumetric cell. In order to obtain results with high accuracy, an analyst is often tasked with dividing the

geometry into small volumes to avoid averaging over regions of high importance. Dividing up the geometry can be a cumbersome task for simple geometries and even impractical for complex designs like those typical of large-scale systems. Chapter 3 puts forth an R2S implementation that includes an extension of the RNUCS tally to function at the resolution of an arbitrary Cartesian mesh and develops a mesh-based RNUCS-R2S workflow for high-fidelity SDR analysis for accelerator-driven facilities. This workflow bypasses the need to divide the geometry, requiring less work from the analyst during the problem setup step. Chapter 3 discusses the full implementation of the workflow, a verification problem, a full production model, and its benefits and limitations.

Using a Cartesian mesh to define the photon source is helpful to the workflow to calculate the SDR. Still, other limitations exist when performing analysis in accelerator-driven systems. Performing the radiation transport steps in complex systems can be computationally expensive, and often, the results do not have satisfactory statistical uncertainties. The statistical uncertainty is a quantity associated with the tallies results from a MC transport. The statistical uncertainties are often high for highly attenuating geometries, like those in a typical accelerator-driven system. This is because particles are often unable to reach important regions in space as they are being attenuated and unable to pass through thick shields. VR techniques are often used to reduce the statistical uncertainty to a satisfactory point. Various VR techniques aim to preferentially simulate particle behavior that contributes to a response of interest. VR techniques include source biasing and population control via splitting and stochastic termination.

One VR method known as CADIS uses a deterministic adjoint function to provide biasing parameters for MC transport [3]. The CADIS method uses an adjoint deterministic transport to define the regions of importance to a detector of interest. This method is useful when an importance function that represents a particle's importance to the result of interest can be defined. The CADIS method is used to reduce the variance of one-step transport problems. Applying the CADIS method to an R2S calculation is a more complicated process as both

steps contribute to the final response. The MS-CADIS method was developed to optimize the primary radiation transport of a multi-step process [4]. The basis of MS-CADIS is to define an importance function for each step that represents the importance of transported particles to some final response. Application of the MS-CADIS to an R2S calculation requires that an adjoint neutron source be defined, for which the adjoint solution represents the importance of neutrons to the final SDR response. The adjoint neutron source can be defined if the relationship between the photon emission density and the neutron flux can be defined via some activation operator that describes this relationship.

A VR method, known as the GT-CADIS method, provides a way to approximate the true relationship between the photon emission density and the neutron flux by using a set of assumptions that linearizes the relationship between the two. This relationship is defined with a linearized activation operator T. The set of assumptions used to linearize the exponentials appearing on the equations required to relate the photon emission density and the neutron flux are referred to as the SNILB criteria [5]. The GT-CADIS method relies on using a series of irradiations with neutrons in a single energy group to solve for the linearized activation operator T. This method has been validated for SDR on fusion devices.

This work expands the GT-CADIS implementation to account for contributions of higher energy neutrons, namely neutrons outside the energy range of cross-section libraries. Chapter 4 describes the mathematical basis for implementing MS-CADIS for accelerator-driven systems. The high-energy GT-CADIS set forth in Chapter 4 provides a way to calculate the linearized activation operator, T, using the neutron flux and the net nuclide production rate. Chapter 4 also presents a way to quantify the efficacy of the high-energy GT-CADIS VR parameters. Chapter 5 describes the software implementation of the high-energy GT-CADIS and the SNILB criteria.

Chapter 6 explores the extent to which the SNILB criteria are met for materials and irradiation scenarios typical of accelerator-driven systems. This is done by calculating an approximation factor, η, which is a ratio between the true photon emission density and

the photon emission density obtained with the linearized activation operator T. This ratio helps quantify how good of an approximation is the SNILB solution to the true solution. A simple problem is designed, and the approximation factor η is calculated per material in the problem. This chapter showed that the SNILB criteria are met or only slightly violated for materials in accelerator-driven systems and realistic irradiation scenarios.

Chapter 7 and Chapter 8 demonstrate the advantages of using high-energy GT-CADIS VR parameters for a simple problem. For the simple problem, it is shown that the use of high-energy GT-CADIS VR parameters can result in a significant speed-up when compared to an analog run. Chapter 7 also explores the implication of implementing GT-CADIS for neutrons up to 25 MeV only. This chapter shows that the implementation of low-energy GT-CADIS is prone to long-history problems and can cause transport calculations to be unable to finish within a reasonable time.

Lastly, Chapter 9 discusses the use of high-energy GT-CADIS VR parameters in a full production problem. For this problem, a neutron source was generated from the original SNS proton source due to limitations of ADVANTG to calculate VR parameters for proton sources. The high-energy GT-CADIS VR parameters were applied to a MC transport with the neutron source and to a MC transport with the original proton source. Only the weight window lower bounds were used for the MC transport with the original source. The SDR was calculated at several detectors placed around an out-of-service SNS target assembly. The results were compared to the experimental values obtained from Popova et al. [6]. The application of VR parameters for this full production problem showed an increase in the neutron transport FOM in important regions compared to the analog FOM.

Chapter 2

Background

This work focuses on advancing the workflow used to calculate the SDR and optimizing the first transport step in a R2S workflow for accelerator-driven systems. Chapter Chapter 2 provides theoretical background information on topics related to the work in this thesis. First, general radiation transport is discussed, including MC and deterministic solution methods. Radiation transport for accelerator-driven systems is also discussed. This chapter then delves into the nuclear inventory analysis theory, followed by the general SDR analysis and accelerator-driven systems SDR methods. This chapter concludes with a discussion of various hybrid MC/deterministic VR techniques.

2.1 Radiation Transport

Radiation transport is an important concept in studying the flux distribution throughout a nuclear system. Radiation transport is an essential step in the calculation of the SDR. In an SDR analysis, the neutron flux distribution is necessary to quantify the nuclear activation of system components. The photon flux distribution is also needed to quantify the dose rate resulting from activated components.

2.1.1 Linear Boltzmann Equation

The transport of particles in a steady-state problem can be described with the linear Boltzmann equation [7] presented in Equation 2.1.

$$\left[\widehat{\Omega}\cdot\vec{\nabla}+\Sigma(\vec{r},E)\right]\psi(\vec{r},E,\widehat{\Omega})= \int_{E'}dE'\int_{4\pi}d\Omega'\Sigma_s(\vec{r},E'\rightarrow E,\widehat{\Omega}'\cdot\widehat{\Omega})\psi(\vec{r},E,\widehat{\Omega})+q(\vec{r},E,\widehat{\Omega}) \quad (2.1)$$

In Equation 2.1, $\psi(\vec{r},E,\widehat{\Omega})$ represents the particle flux as a function of position, angle, and energy, $\Sigma(\vec{r},E)$ is the total macroscopic cross-section, $\Sigma_s(\vec{r},E'\rightarrow E,\widehat{\Omega}'\cdot\widehat{\Omega})$ is the double differential scattering cross-section, and $q(\vec{r},E,\widehat{\Omega})$ is a fixed external source. Equation 2.1 is often written in operator notation as

$$\mathcal{H}\psi(\vec{r},E,\widehat{\Omega})=q(\vec{r},E,\widehat{\Omega}), \quad (2.2)$$

where $\mathcal{H}$ captures the particle behavior in all interactions in a single term given by:

$$\mathcal{H}=\widehat{\Omega}\cdot\vec{\nabla}+\Sigma(\vec{r},E)-\int_{E'}dE'\int_{4\pi}d\Omega'\Sigma_s(\vec{r},E'\rightarrow E,\widehat{\Omega}'\cdot\widehat{\Omega}) \quad (2.3)$$

2.1.2 Adjoint Radiation Transport

The adjoint radiation transport equation describes the transport of adjoint particles from a region of interest to the source. The adjoint transport equation is important because, under the appropriate circumstances, the adjoint flux ($\Psi^\dagger$) has a physical meaning as the importance of a particle to a response. This physical interpretation of $\Psi^\dagger$ allows the development of some MC VR methods, which are discussed later in this chapter. The adjoint transport is defined by Equation 2.4.

$$\mathcal{H}^\dagger\psi^\dagger=q^\dagger, \quad (2.4)$$

where $\mathcal{H}^\dagger$ is the adjoint transport operator analogous to the forward operator, and $q^\dagger$ is the adjoint source. The adjoint identity is defined by Equation 2.5.

$$\langle\psi^\dagger\mathcal{H}\psi\rangle=\langle\psi\mathcal{H}^\dagger\psi^\dagger\rangle, \quad (2.5)$$

where $\langle \cdot \rangle$ denotes the integration over all phase space. The adjoint identity given by Equation 2.5 can be simplified using Equation 2.2 and Equation 2.4 as shown in Equation 2.6.

$$\langle q^\dagger \psi \rangle = \langle q \psi^\dagger \rangle \tag{2.6}$$

The selection of an appropriate $q^\dagger$ is necessary as this definition gives the basis for the adjoint flux to have a physical meaning. Suppose $q^\dagger$ is selected to be equivalent to the forward detector response function σ_d. In that case, the resulting adjoint flux has the physical meaning as the importance of a region of phase space to the detector response [8]. The detector response equation is given by Equation 2.7.

$$R = \langle \psi \sigma_d \rangle \tag{2.7}$$

An alternative response equation can be formulated using $q^\dagger = \sigma_d$ and Equation 2.6 as shown in Equation 2.8.

$$R = \langle \psi^\dagger q \rangle \tag{2.8}$$

Equation 2.8 shows that obtaining the response is possible if the adjoint flux is known for any given source.

2.1.3 Deterministic Radiation Transport

Though the Boltzmann equation can be solved analytically for simple problems, as problems become more complex and realistic, the transport equation becomes more complicated, and the analytical solution is harder to obtain. The complexity of nuclear systems has necessitated the development of numerical techniques to solve the radiation transport problem. The deterministic method requires the discretization of space, energy, and direction to obtain an approximate solution to the transport equation. Several deterministic methods have been developed, with the most prominent method being the S_n method [7]. The S_n method solves the transport equation in discrete angular directions. Most deterministic methods use the energy-discretized multigroup approximation equation. The flux for each energy group g is given by Equation 2.9.

$$\psi_g(\vec{r},\widehat{\Omega}) = \int_{E_{g+1}}^{E_g} \psi(\vec{r},\widehat{\Omega},E)dE \tag{2.9}$$

A similar equation can be written for the multigroup scattering cross-sections and the external source term, respectively, leading to Equation 2.10.

$$\left[\widehat{\Omega}\cdot\vec{\nabla}+\Sigma_g(\vec{r})\right]\psi_g(\vec{r},\widehat{\Omega}) = \sum_{g'=1}^{G}\int_{4\pi} d\widehat{\Omega}'\Sigma_{s,gg'}(\vec{r},\widehat{\Omega}'\cdot\widehat{\Omega})\psi_{g'}(\vec{r},\widehat{\Omega}') \tag{2.10}$$

Due to the discretization, the S_n method sacrifices accuracy, but this method can be used to obtain global flux distributions quickly.

2.1.4 Monte Carlo Radiation Transport

Another technique to solve the transport equation is the Monte Carlo (MC) method. The MC method is a stochastic method, which typically involves simulating a finite number of particles using pseudo-random numbers to sample the PDF of the physical behavior of the particle. The MC method is considered more accurate than deterministic methods because it does not discretize the physical space, angle, and energy. The MC method is widely used in nuclear system analysis because of its capability to treat more complex systems and its high fidelity.

The MC method records the scores in tallies to quantify a response of interest [9]. MC simulations have an associated statistical error typically quantified using the relative error R given by Equation 2.11.

$$R = \frac{1}{\bar{x}}\frac{S_x}{\sqrt{N_{scores}}}, \tag{2.11}$$

where $\bar{x}$ is the mean of the tally scores S_x is the standard deviation of the tally scores, and N_{scores} is the number of tally scores. The FOM is another important quantity in the performance of the MC method. The FOM is given by:

$$FOM = \frac{1}{R^2 t_{proc}}, \tag{2.12}$$

where t_{proc} is the processor time needed to reach a low R.

In accelerator-driven systems, the high degree of analysis accuracy necessitates the use of MC radiation transport. The high degree of accuracy obtained with MC comes with the cost of long convergence times compared to deterministic methods. The high uncertainty that arises from having limited time is mitigated through VR methods, which are discussed in Section 2.4.

This work utilizes MCNP6 transport code, which was developed by Los Alamos National Laboratory [9]. MCNP6 is a general-purpose and continuous-energy MC radiation transport code for neutron, photon, and electron transport. In MCNP6, a text-based Constructive Solid Geometry (CSG) language is used to define geometry cells and surfaces. However, in this work, geometries will mainly be created using CAD software. All radiation transport calculations are done directly on a CAD geometry using DAG-MCNP6, which uses the DAGMC toolkit. DAGMC [10] is a toolkit that facilitates ray tracing on a CAD geometry used for particle tracking during transport. A DAGMC geometry is a CAD geometry that has been faceted.

2.1.5 Radiation Transport in Accelerator-Driven Systems

In accelerator-driven systems, the spallation process is the dominant process. The spallation process involves energetic charged particles interacting with an atomic nucleus. The spallation process can be thought of as having two stages: the intranuclear cascade and evaporation. In the first stage, a high-energy charged particle interacts with nucleons inside the target nucleus. The reactions from this interaction create a cascade of high-energy particles (i.e., protons, neutrons, pions). Some of these high-energy particles escape the nucleus and move on to start their own reaction with other nuclei. Other high-energy particles deposit kinetic energy in the nucleus, leaving it in an excited state. The second stage of the spallation process is the evaporation or nuclear de-excitation stage. In this stage, the excited nucleus releases other low-energy particles like neutrons and alpha particles to be-

come de-excited [11]. The majority of particles released during this stage are neutrons. The low-energy neutrons remaining from this stage can be moderated to be used as sources for research. The leftover nucleus can be radioactive and might release gamma rays.

The release of high-energy particles, including neutrons, requires that the transport of these particles be modeled. Radiation transport codes often rely on cross-section data to represent the probability of interaction between the transported particles and the medium in which they are being transported. The cross-section data libraries are often limited in information for some particles and for neutrons of energies above some threshold. The limited cross-section data available means that nuclear physics models are necessary to model the interactions between high-energy particles and the medium in which they are being transported. Nuclear physics models typically exist in radiation software codes like MCNP and can be used to describe the interactions between particles and medium. Typical physics interaction models included in MCNP are Bertini, ISABEL, CEM, and LAQGSM [9]. In radiation transport for accelerator-driven systems, a combination of cross-section data tables and nuclear physics models are used to describe all interactions. For a given particle at some energy E, if data cross-section tables are unavailable, nuclear physics models are used to model the interaction between this particle and the medium in which it is being transported. From here on out, the energy domain outside the cross-section data tables will be referred to as the high-energy domain, which for this work are groups above above 25 MeV. Energy groups below 25 MeV will be referred to as the low-energy domain. For this work, nuclear physics models describe the probability of interactions of all charged particles and neutrons in the high-energy domain, and cross-section data tables are used to describe the probability of interaction for neutrons in the low-energy domain.

2.2 Nuclear Inventory

When materials in nuclear systems are exposed to neutron flux, a chain of events occurs, producing radionuclides that emit radiation. These radionuclides can be produced via interaction with neutrons, which occur during the operation of the system, and via decay processes, which can occur both during the operation of the systems or after they have been shut down.

To describe the nuclear inventory that is present when these materials become activated, one can start with the rate of change of nuclear concentration, which is given by Equation 2.13.

$$\frac{dN_i(t)}{dt} = \sum_j N_j(t) P_{j\to i} - \sum_j N_i(t) P_{i\to j} \tag{2.13}$$

In equation 2.13, N_i is the nuclide concentration for nuclide i, and P is a production constant. The first term in Equation 2.13 represents the production of nuclide i from all other nuclides j. The second term represents the destruction of nuclide i into other nuclides j. The production rate constant, P, for nuclear reactions is given by Equation 2.14.

$$P_{i\to j,reaction} = \int_{E_n} \sigma_{i\to j}(E_n)\phi_n(E_n)dE_n, \tag{2.14}$$

where $\sigma_{i\to j}(E_n)$ is the microscopic cross-section for the reaction that takes nuclide i to nuclide j, and $\phi_n(E_n)$ is the neutron flux, both a function of neutron energy E_n. For the decay process, the production rate constant is given by Equation 2.15.

$$P_{i\to j,decay} = \lambda_i b_{i\to j}, \tag{2.15}$$

where λ_i is the decay constant for nuclide i, and $b_{i\to j}$ is the branching ratio for the pathway that takes nuclide i to nuclide j. The total production rate constant in Equation 2.13 is obtained by adding the production constant from nuclear reactions and the production constant from decay processes as shown in Equation 2.16.

$$P_{i\to j,total} = P_{i\to j,reaction} + P_{i\to j,decay} \tag{2.16}$$

For multiple nuclides, Equation 2.13 becomes a system of first-order linear differential equations and can be represented in the vector notation as shown in Equation 2.17.

$$\frac{d\vec{N}(t)}{dt} = \boldsymbol{A}\vec{N}(t) \tag{2.17}$$

Equation 2.18 gives the solution to the first-order linear differential equations system.

$$\vec{N}(t) = \vec{N}_o e^{\boldsymbol{A}t} \tag{2.18}$$

One way that Equation 2.18 can be resolved is by breaking the transmutation network into a collection of linear chains so that each nuclide has one production term and one destruction term, making the $\boldsymbol{A}$ a bidiagonal matrix, thus allowing a solution in the form of the Bateman Equation shown in Equation 2.19 [12].

$$N_i(t) = \sum_{j=1}^{i} N_j(0) \left[\left(\prod_{k=j}^{i-1} P_k \right) \sum_{k=j}^{i} \frac{e^{-d_k t}}{\prod\limits_{l=j,\neq k}^{i} (d_l - d_k)} \right] \tag{2.19}$$

where P and d represent the production and destruction rates.

2.2.1 Nuclear Inventory in Accelerator-Driven Systems

Equation 2.19 relies on activation cross-section tables to obtain the production and destruction rates. In accelerator-driven systems, cross-section tables are limited to some energy threshold, and production and destruction rates must be supplied for this high-energy domain. The nuclide concentration rate equation must include an additional term to account for the production and destruction rates in the high-energy domain. Equation 2.20 shows the rate of change in nuclide concentration, including the extra term.

$$\frac{dN_i(t)}{dt} = \sum_j N_j(t) P_{j \to i,total} - \sum_j N_i(t) P_{i \to j,total} + Y_i, \tag{2.20}$$

where the first and second terms represent the production and destruction of nuclides. Both terms account for the nuclear interaction in the energy domain of cross-section tables and

the decay process. The third term, Y_i, is a production/destruction constant that accounts for the interactions above the energy domain of cross-section tables.

When many nuclides are involved, a system of linear equations is created. This is given by Equation 2.21 with the corresponding solution given by Equation 2.22.

$$\frac{d\vec{N}(t)}{dt} = \boldsymbol{A}\vec{N}(t) + \vec{Y} \tag{2.21}$$

$$\vec{N}(t) = \vec{N}_o e^{\boldsymbol{A}t} - \boldsymbol{A^{-1}}\vec{Y}(1 - e^{\boldsymbol{A}t}) \tag{2.22}$$

The complexity of the transfer matrix, $\boldsymbol{A}$, can be solved with the Bateman equations. The solution for nuclide concentration, N_i, is given by Equation 2.23:

$$\begin{aligned} N_i(t) = &\sum_{j=1}^{i} N_j(0) \left[\left(\prod_{k=j}^{i-1} P_k \right) \sum_{k=j}^{i} \frac{e^{-d_k t}}{\prod\limits_{l=j,\neq k}^{i} (d_l - d_k)} \right] + \\ &\sum_{j=1}^{i} Y_j \left[\left(\prod_{k=j}^{i-1} P_k \right) \left(\frac{1}{\prod\limits_{m=j}^{i} d_m} - \sum_{k=j}^{i} \frac{e^{-d_k t}}{d_k \prod\limits_{l=j,\neq k}^{i} (d_l - d_k)} \right) \right], \end{aligned} \tag{2.23}$$

where P and d are production and destruction terms from low-energy nuclear interactions that are not included in the Y term.

2.2.2 Activation Software

The photon emission density is typically calculated with nuclear inventory software. Various nuclear inventory codes can be used in an R2S calculation. For accelerator-driven systems, the chosen code must have the ability to use high-energy interaction information.

Various codes are often used for high-energy activation analysis. CINDER is an activation code initially developed for reactor calculations, and later, the ability to work with accelerator-driven systems transmutation problems was developed in the code [13]. CINDER is able to take in a constant term to account for production and destruction rates associated with reactions outside the nuclear data cross-sections tables. FISPACT is a nuclear inventory code included in the EASY. FISPACT was first developed for calculations of

neutron-induced material activation in fusion devices [14]. SP-FISPACT is an extension of the FISPACT software that is able to perform activation calculations for accelerator-driven problems [15]. Like CINDER, SP-FISPACT can take in production and destruction information from reactions above the nuclear cross-section data limits. Another code that is used for accelerator-driven systems is the ORIHET3. This activation software takes nuclide production and destruction information for all energy groups [16]. The setup requires that the neutron flux for low energies interactions are folded with nuclear cross-section data to obtain the nuclide production and destruction rates.

In this work, CINDER is used to model the activation step. CINDER was chosen because of its ability to take in high-energy interaction information and because the analysis in this work is often compared to analysis previously done using CINDER to model the activation step.

2.3 Shutdown Dose Rate

In accelerator-driven systems, the biological dose rate from the photons emitted must be quantified as a function of position and time after shutdown. One of the predominant processes to calculate the shutdown dose rate (SDR) for a nuclear system is Rigorous Two-Step (R2S) [1]. This process couples particle transports and nuclear inventory analysis to solve for the SDR.

2.3.1 R2S Method

The R2S method involves a separate neutron and photon transport coupled by nuclear activation analysis. This method starts with a neutron transport to tally the neutron flux using some spatial and energy discretization. The neutron flux is used along with an irradiation schedule to carry out an activation calculation using a nuclear inventory analysis code. The nuclear inventory analysis code provides a photon emission density, which can be used as a

source for photon transport. The SDR is tallied in the photon transport using flux-to-dose conversion factors. A typical R2S workflow is shown in Figure 2.1.

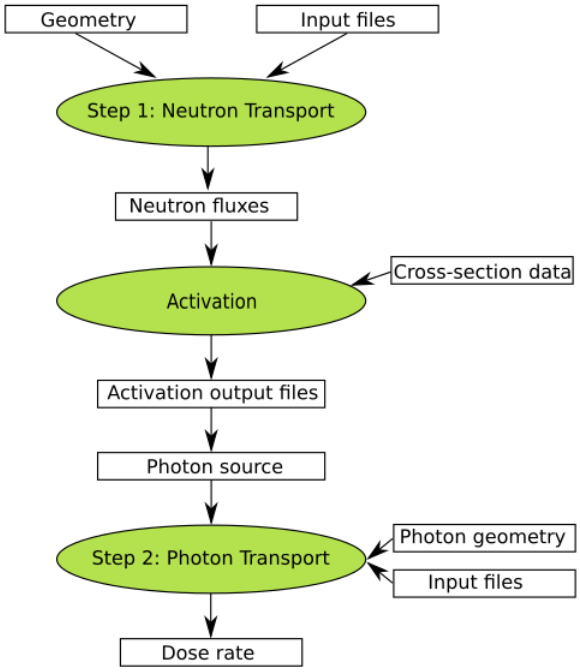

Figure 2.1: R2S workflow

2.3.2 Radionuclide Tally

In an R2S analysis for accelerator-driven systems, the activation step is limited by the available nuclear cross-section data. In the transport step, neutrons are created with high energies, even higher than what is typically seen in nuclear cross-section data tables. Nuclear cross-section data tables have historically existed for neutrons of energy up to 25 MeV and more recently for neutrons of energy up to 150 MeV. The nuclear cross-sections are needed to solve Equation 2.14 in the activation calculation. The cross-section data limitation necessitated the use of physics models in the transport step to calculate the reaction production and destruction rates from high-energy interactions before moving into the activation step. These production and destruction rates of high-energy interactions were historically calculated using a history file from an MCNP calculation. These history files recorded information from nuclear interactions in the physics model domain. These history files were then post-

processed to obtain the production and destruction rates at these high energies [17]. In more recent years, a tally has been implemented in MCNPX to collect the production and destruction rates from the physics model domain [2]. This tally, RNUCS, collects production and destruction rates for any given volume and reports the results directly on the MCNP output file. These production and destruction rates and the neutron flux for less than 20 MeV interactions are passed to an activation software to obtain the photon emission density.

2.3.3 RNUCS-R2S Method

A full workflow to calculate SDR in accelerator-driven systems has been implemented with scripts (written in Perl) to automate pieces of the work. Figure 2.2 shows the steps needed to run this workflow. The activation script collects the nuclide production/destruction rates and the neutron flux and formats this information into the appropriate activation input files [18]. This script creates input files for several activation calculation software, including CINDER'90, ORIHET, and FISTPACT. The output of the activation calculation is post-processed with a gamma flux script. This gamma flux script uses the activation calculation output to construct a photon source, which is defined for given geometric volumes.

2.4 Variance Reduction Methods

The MC method discussed in section 2.1.4 has limitations when dealing with highly attenuating or heavily shielded problems. In analog MC transport, the characteristics of a particle and its behavior are sampled from an unbiased probability density function (PDF). This unbiased PDF represents the natural probability that some event occurs [19]. Sampling from an unbiased PDF can lead to low convergence rates for tallies placed outside highly attenuated areas. This is because only a small fraction of particles reach the region of interest, leading to high uncertainty/variance in the tally.

The relative error, given in Equation 2.11, can be reduced by either increasing the number

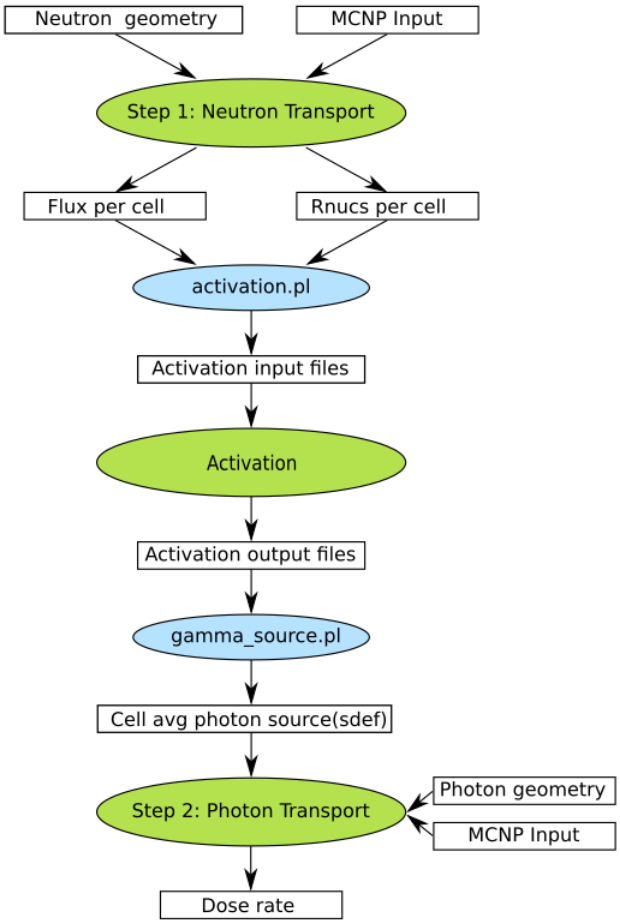

Figure 2.2: RNUCS-R2S workflow for accelerator-driven nuclear systems

of particles N or decreasing the standard deviation S_x. Increasing N has the disadvantage of increasing the time to convergence, leading to a decrease of the FOM, which quantifies the efficiency of the MC calculation.

In order to reduce the variance and improve the efficiency of the MC transport, variance reduction (VR) techniques are used to preferentially sample particles and behaviors that lead to a score on the tally of interest. The use of a biased PDF to modify the physical laws of the transport leads to the concept of particle weights. Modifying the particle weights compensates for the use of biased PDF. Equation 2.24 gives a relationship between biased and unbiased PDFs with corresponding weights.

$$w_{unbiased} p_{unbiased} = w_{biased} p_{biased}, \tag{2.24}$$

VR techniques for MC can use these biased PDFs. Biasing techniques can be thought of in three categories: source biasing, transport biasing, and collision biasing. In this work, source and transport biasing are used. Transport biasing is done using population control methods such as particle splitting and stochastic termination.

2.4.1 Source and Transport Biasing

In an MC transport calculation, the source is sampled from a PDF. In a non-analog MC transport, a biased PDF can be used to sample source particles. The source particles sampled from the biased PDF must be born with weight defined by Equation 2.24.

Population control is a transport biasing technique that increases the number of particles in areas important to a detector response. In MCNP, the weight window method is an implementation of population control in which particles are split in regions of high importance and stochastically terminated in regions of low importance. The weights of the particles are modified so that the total weight is conserved. Weight windows are implemented as a set lower weight window parameter that represents the importance of the region. When a particle moves from a region of low importance to a region of high importance, the particle is split into n particles, and the weight is modified to $1/n$ of the original weight. If a particle moves from a more important region to a less important region, the particle is terminated with some statistical probability p. If the particle survives termination, the weight of the particle is increased. Automated weight window lower bound parameters can be defined using problem-specific information.

2.4.2 CADIS

The CADIS method is a hybrid workflow that uses deterministic methods to generate MC VR parameters. The CADIS method uses an estimate of the adjoint flux to formulate weight window lower bounds for transport biasing, which is made consistent with source biasing [3].

In Section 2.1.2, it was shown that if the response function σ_d is chosen to be equivalent to the adjoint source, then the response can be written as

$$R = \int_{4\pi}\int_{E}\int_{V} \psi^{\dagger}(\vec{r}, E, \widehat{\Omega}) q(\vec{r}, E, \widehat{\Omega}) d\vec{r} dE d\widehat{\Omega} \tag{2.25}$$

In Equation 2.25, the adjoint flux, $\psi^{\dagger}$, has physical meaning as the expected contribution to the response.

The adjoint flux, $\psi^{\dagger}$, can be used to define the weight of particle using Equation 2.26

$$\omega(\vec{r}, E) = \frac{R}{\psi^{\dagger}(\vec{r}, E, \widehat{\Omega})} \tag{2.26}$$

Adjusting the weight of a particle biases the transport, and for consistency, the source is also biased to satisfy Equation 2.27.

$$\omega(\vec{r}, E, \widehat{\Omega}) \widehat{q}(\vec{r}, E, \widehat{\Omega}) = \omega_0 q(\vec{r}, E, \widehat{\Omega}) \tag{2.27}$$

In Equation 2.27, ω_0 is the unbiased particle weight, which is often set equal to 1. Substituting Equation 2.26 into Equation 2.27 leads to Equation 2.28 for biased source.

$$\widehat{q}(\vec{r}, E, \widehat{\Omega}) = \frac{\psi^{\dagger}(\vec{r}, E, \widehat{\Omega}) q(\vec{r}, E, \widehat{\Omega})}{R} \tag{2.28}$$

In MCNP, the weight window technique is applied by using the lower bound weight windows, ω_l, such that the statistical weight from Equation 2.26 is at the center of the weight window. The lower bound weight window is given by Equation 2.29.

$$\omega_l(\vec{r}, E) = \frac{R}{\left(\frac{1+C_u}{2}\right)\psi^{\dagger}(\vec{r}, E)}, \tag{2.29}$$

where C_u is the ratio between the upper and lower weight window values as shown in Equation 2.30.

$$C_u = \frac{W_u}{W_l} \tag{2.30}$$

The CADIS method is useful for one-step problems that aim to reduce the variance on a single detector response. Sometimes, global VR might be desired. The FW-CADIS method

is a deterministic method that provides VR parameters for global VR. FW-CADIS uses the results of a forward deterministic transport to develop an adjoint source that is used to define an importance function that optimizes for a global quantity.

2.4.3 MS-CADIS

In an R2S calculation, it is often useful to reduce the variance in both transport steps: the neutron transport and the photon transport. If the optimization of a single detector is needed, then the CADIS method can be used for the photon step. Optimizing the neutron step is more complicated because it is necessary to define how the neutrons contribute to the SDR. That is to say, it is necessary to define an importance function that describes the importance of neutrons to the final response SDR. This importance function is not easily defined since the neutrons do not directly contribute to the SDR.

The MS-CADIS method was developed to optimize the primary step of a coupled multi-physics problem. The basis of MS-CADIS is that an approximate importance function can be defined that describes the expected contribution of each step to a final response of interest [4]. The importance function describing the expected contribution from the primary step is found by using a primary physics adjoint source that captures the relationship between the primary solution and the source of the secondary step. The relationship between the primary physics solution, ϕ_1, and the source used for the secondary physics, q_2 can be described by the Equation 2.31.

$$q_2 = f(\phi_1) \tag{2.31}$$

When MS-CADIS is applied to SDR, it provides a way to define an adjoint neutron source that captures the probability of regions to become activated and emit photons that contribute to the SDR detector.

The SDR detector response from the photons is given by Equation 2.32.

$$SDR = \langle \sigma_d(\vec{r}, E_p)\phi_p(\vec{r}, E_p) \rangle \tag{2.32}$$

If adjoint photon source $q_p^\dagger$ is set equal to the response function σ_d and the adjoint identity applied, then the SDR is given by Equation 2.33.

$$SDR = \langle \phi_p(\vec{r}, E_p), q_p^\dagger(\vec{r}, E_p) \rangle = \langle \phi_p^\dagger(\vec{r}, E_p), q_p(\vec{r}, E_p) \rangle \tag{2.33}$$

For the neutron transport, the MS-CADIS method requires an adjoint neutron source that satisfies the neutron response being equivalent to the final response.

$$SDR = \langle \phi_n(\vec{r}, E_n), q_n^\dagger(\vec{r}, E_n) \rangle = \langle \phi_n^\dagger(\vec{r}, E_n), q_n(\vec{r}, E_n) \rangle \tag{2.34}$$

From Equations 2.33 and 2.34, it follows that:

$$\langle \phi_n(\vec{r}, E_n), q_n^\dagger(\vec{r}, E_n) \rangle = \langle \phi_p^\dagger(\vec{r}, E_p), q_p(\vec{r}, E_p) \rangle \tag{2.35}$$

To solve for $q_n^\dagger(\vec{r}, E_n)$ in Equation 2.35, a relationship between the neutron flux and the photon emission density must be defined. This relationship is often complicated due to the intrinsic nature of the transmutation process. The complicated relationship between the photon emission density and the neutron flux can be approximated with a linear form by defining a linearized activation operator. This linear relationship is shown in Equation 2.36, where $T(\vec{r}, E_n, E_p)$ is the linearized activation operator.

$$q_p(\vec{r}, E_p) = \langle T(\vec{r}, E_n, E_p), \phi_n(\vec{r}, E_n) \rangle \tag{2.36}$$

If a linear form of Equation 2.36 can be defined, then Equation 2.36 can be substituted into Equation 2.35 to obtain Equation 2.37.

$$\langle\ \phi_n(\vec{r}, E_n)\ , q_n^\dagger(\vec{r}, E_n)\ \rangle = \langle\ \phi_p^\dagger(\vec{r}, E_p)\ , \langle\ T(\vec{r}, E_n, E_p)\ , \phi_n(\vec{r}, E_n)\ \rangle\ \rangle \tag{2.37}$$

Switching the order of integration allows for the following expression:

$$\langle\ \phi_n(\vec{r}, E_n)\ , q_n^\dagger(\vec{r}, E_n)\ \rangle = \langle\ \langle\ T(\vec{r}, E_n, E_p)\ , \phi_p^\dagger\ \rangle\ , \phi_n(\vec{r}, E_n)\ \rangle \tag{2.38}$$

Solving for the adjoint neutron source in Equation 2.38 and expressing in integral form leads to the following expression:

$$q_n^\dagger(\vec{r}, E_n) = \int_{E_p} T(\vec{r}, E_n, E_p) \phi_p^\dagger dE_p \tag{2.39}$$

In Equation 2.39, the adjoint photon flux ($\phi_p^\dagger$) can be estimated with a deterministic transport run, given that the dose-response function, σ_d, is used as the adjoint photon source. If $T(\vec{r}, E_n, E_p)$ can be defined, then a solution for $q_n^\dagger(\vec{r}, E_n)$ can be obtained using Equation 2.39. The $q_n^\dagger(\vec{r}, E_n)$ can then be used to calculate the adjoint neutron flux. The adjoint neutron flux is used with the CADIS method to optimize the neutron transport in a multi-step problem.

2.4.4 GT-CADIS

GT-CADIS is an implementation of the MS-CADIS method for SDR analysis of fusions systems. GT-CADIS provides a way to calculate $T(E_n, E_p)$, which is necessary for calculating the adjoint neutron flux [5].

The GT-CADIS method seeks to define a linear relationship between the photon emission density and the neutron flux as given in Equation 2.36. In order to find this relationship, the transmutation problem is defined in terms of independent transmutation chains. The photon emission density for a simple irradiation and decay scenario consisting of one irradiation time (t_{irr}) followed by a decay period (t_{dec}), can be expressed as a sum of contributions from the last nuclide i_c in transmutation chain c as shown in Equation 2.40.

$$q_p(E_p, t_{tot}) = \sum_c \lambda_{c,i_c} b_{c,i_c}(E_p) N_{c,i_c}(t_{tot}) \tag{2.40}$$

In this equation, λ_{c,i_c} is the decay constant, and $b_{c,i_c}(E_p)$ is the branching function for nuclide i_c in chain c. The flux dependent term, $N_{c,i_c}(t_{tot})$, is defined by Equation 2.41.

$$\begin{aligned} N_{c,i_c}(t_tot) =& N_{c,i_c}(t_{irr}) e^{-d_{c,i_c} t_{dec}} + \\ & \sum_{j=1}^{i_c} \left[N_{c,j}(t_{irr}) \sum_{k=j}^{i_c-1} \left(\frac{P_{k+1}(e^{-d_{c,k} t_{dec}} - e^{-d_{c,i_c} t_{de}})}{d_{c,i_c} - d_{c,k}} \prod_{l=j,\neq k}^{i_c-1} \frac{P_{c,l+1}}{d_{c,l} - d_{c,k}} \right) \right] \end{aligned} \tag{2.41}$$

In Equation 2.41, the production terms P and destruction terms d only represent production and destruction during the decay interval. These production and destruction terms are not flux-dependent.

The flux-dependent term, $N_{c,(t_{irr})}$, can be expressed with the Bateman equation. To simplify the Bateman equation and account for modeling each transmutation chain separately, only the first nuclide N_1 is present at the beginning of irradiation, and all other concentrations are zero.

$$N_i(t_{irr}) = \begin{cases} N_i(0)e^{-d_i t_{irr}} \qquad i = 1, & \text{(2.42a)} \\ N_1(0)\sum_{k=1}^{i-1}\left(\frac{P_{k+1}(e^{-d_k t_{irr}} - e^{-d_i t_{irr}})}{d_i - d_k}\prod_{l=j,\neq k}^{i-1}\frac{P_{l+1}}{d_l - d_k}\right) \quad i > 1, & \text{(2.42b)} \end{cases}$$

Some of the production and destruction terms in Equation 2.42, which might be flux dependent, are in exponential form. To cast this equation into a linear form, an approximation of the exponentials is made using a Taylor expansion. Truncation of the exponential term to obtain a linear relationship to the flux leads to criteria for which the linearization holds. The criteria, referred to as the SNILB criteria, is detailed in Equation 2.43.

$$\left|(d_k^{i-2} - d_i^{i-1})\frac{(-t_{irr})^{i-2}}{(i-1)!}\right| >> \left|(d_k^i - d_i^i)\frac{(-t_{irr})^i}{i!}\right| \text{ for } i \,\epsilon\, [2, i_c],\ k \,\epsilon\, [1, i-1] \tag{2.43a}$$

$$P_2 = \int_{E_{n1}} \sigma_{1\to 2}(E_{n1})\phi_n(E_{n1})dE_{n1} \tag{2.43b}$$

$$P_j \neq P_j(\phi_n(E_{n1})) \text{ for } j \,\epsilon\, [3,\, i_c] \tag{2.43c}$$

If the SNILB criteria are met, then $T(E_n, E_p)$ can be found in the form given by Equation 2.44.

$$T(E_n, E_p) = \sum_c \lambda_{c,i_c} b_{c,i_c}(E_p) N_{c,1}(0)\left[\left[\sigma_{c,1\to 2}(E_n)\frac{t_{irr}^{i_c-1}}{(i_c-1)!}\prod_{j=3}^{i_c} P_{c,j}\right]e^{-d_{c,i_c}t_{dec}} + \sum_{j=2}^{i_c-1}\left[\sigma_{c,1\to 2}(E_n)\frac{t_{irr}^{j-1}}{(j-1)!}\prod_{k=3}^{j} P_{c,k}\right]B_{c,i_c,j}(t_{dec})\right] \tag{2.44}$$

The GT-CADIS method poses that $T(E_n, E_p)$ can be calculated by performing multiple irradiation calculations, each with single group flux $\phi_n(E_g)$. $T(E_g, E_h)$ can be calculated with Equation 2.45 for neutron energy group g and photon energy group h.

$$T(E_g, E_h) = \frac{q_p(E_h, \phi_n(E_g))}{\phi_n(E_g)} \tag{2.45}$$

GT-CADIS also provides a way to assess the efficacy of the VR parameters generated using the GT-CADIS method. Using the discrete form of Equation 2.36 as shown in Equation 2.46, it states that when the SNILB criteria are met, the photon emission density in photon energy group h resulting from irradiation with some flux ϕ_n can be expressed as the summation of contributions resulting from irradiation with each constituent neutron energy group.

$$q_p(E_h) = \sum_g T(E_g, E_h)\phi_n(E_g) \tag{2.46}$$

Equation 2.46 can also be written as Equation 2.47.

$$q_p(E_h) = \sum_g q_p(\phi_n(E_g)) \tag{2.47}$$

This expression is true when the SNILB criteria are met but will not hold true when the SNILB criteria are violated. Equation 2.47 can be used to assess the extent to which the SNILB criteria are met by rearranging it as a ratio to define an approximation factor η. This is shown in Equation 2.48

$$\eta_h = \frac{\sum_g q_p(\phi_n(E_g))}{q_p(E_h)} \tag{2.48}$$

2.5 Evaluating the Performance of VR parameters in R2S Calculations

Generally, in order to assess the performance advantages of using VR in MC calculations, the FOM can be used. This section provides background information for evaluating the VR performance as it pertains to VR parameters generated with GT-CADIS to optimize the neutron transport.

The FOM, initially introduced in Section 2.1.4, is a metric to inform the computational performance of a MC transport calculation. Recalling that FOM is inversely proportional to the relative error squared, R^2, and the processor time t_{proc}, a high FOM indicates a low relative error and/or low processor time. One way to increase the FOM is by decreasing the

relative error R. R^2 can be decreased by increasing the number of histories, N as they are inversely proportional as shown in Equation 2.49.

$$R^2 = \frac{C_R}{N} \tag{2.49}$$

However, t_{proc} is proportional to N as shown in Equation 2.50, and VR methods that reduce R could increase C_t, thus not necessarily increasing the FOM.

$$t_{proc} = C_t N \tag{2.50}$$

Using Equations 2.50 and 2.49, Equation 2.12 can be rewritten as Equation 2.51. C_R and C_t are constants of proportionality. Efficient VR methods will decrease C_R faster than C_t increases.

$$FOM = \frac{1}{C_R C_t} \tag{2.51}$$

2.5.1 Error in the Flux and the Source

When the VR parameters are generated to optimize the neutron transport of an R2S calculation, the neutron flux statistical error is an important metric to help understand the performance of the VR parameters on the specific problem. If directly compared to an analog calculation, this statistical error informs which energy-space areas are affected by the VR parameters.

The photon transport will also generate a statistical error. This statistical error does not account for errors in the photon source and only represents the error in the photon transport. For R2S calculations, the photon transport has some error associated with it as the source is generated using neutron fluxes with statistical errors.

The work in Harb et al. [20] sets forth a way to propagate the error in neutron flux to the photon source using the neutron flux error and the linearized activation operator $T(E_n, E_p)$.

$$\sigma^2_{q_{v,p}(E_h)} = \sum_g T^2_v(E_g, E_h)\sigma^2_{\phi_{v,n}(E_g)} + 2\sum_{\substack{g,g' \\ g<g}} T_v(E_g, E_h)\sigma_{\phi_{v,n}(E_g)} T_v(E_{g'}, E_h)\sigma_{\phi_{v,n}(E_{g'})}\rho(\phi_{v,n}(E_g), \phi_{v,n}(E_{g'})) \tag{2.52}$$

Where $\sigma_{q_{v,p}(E_h)}$ is the standard deviation of the photon emission density in mesh voxel v and photon energy group h, $\sigma_{\phi_{v,n}(E_g)}$ is the standard deviation of the neutron flux in mesh voxel v and neutron energy group g or g', and $\rho(\phi_{v,n}(E_g), \phi_{v,n}(E_{g'}))$ is the correlation between the neutron flux in groups g and g' in mesh voxel v.

The correlation between neutron fluxes in different energy groups is complicated and has been extensively studied in Harb et al. [20]. In this work, only the minimum and maximum photon source error will be calculated by setting $\rho(\phi_{v,n}(E_g), \phi_{v,n}(E_{g'}))$ to zero and one, respectively.

Chapter 3

Mesh-based RNUCS-R2S Workflow

The operation of accelerator-driven systems often requires quantification of values like the SDR for a component that has reached end of life. The SDR can be calculated via the R2S method. An existing implementation of the R2S method for accelerator-driven systems, introduced in Section 2.3.3, determines the photon emission density at the resolution of a geometric cell. This implementation uses a special tally, RNUCS, to collect radionuclide production rates from reactions simulated by event generator models existing in transport codes [2]. These production rates are collected per geometric cell and in energy regions where neutron activation cross-section tables are non-existent. The neutron flux is tallied for low-energy regions, where the activation cross-section tables are present. In this cell-based RNUCS-R2S workflow, the nuclear inventory changes, and subsequently, the photon emission density is averaged over a geometric cell. This limitation often means that analysts must divide the geometry into small volumes to avoid averaging fluxes over large gradients. Splitting the geometry is not an easy task and even impractical for complex designs. A more efficient option is to use a superimposed mesh to calculate more locally accurate quantities. Work has been done to utilize mesh flux tally capabilities of MCNP to calculate SDR in fusion devices [21].

This chapter discusses the work to extend the nuclear inventory tally, RNUCS, to function at the resolution of an arbitrary Cartesian mesh and develops a mesh-based RNUCS-R2S workflow for high fidelity SDR analysis for accelerator-driven systems. This workflow bypasses the need to split geometry, requiring less work from the analyst during the problem set up step. The use of meshes also allows analysts to try multiple meshes with little effort,

albeit at a more significant computational effort. The use of Cartesian meshes has its limitations, namely the fact that they are not conformal to the geometry, requiring some over or underestimation of quantities. Another limitation is the material mixing that might be necessary, which can also lead to significant changes in estimation.

The implementation of the mesh-based RNUCS-R2S workflow is described in Section 3.1. A set of verification problems and the limitations of the workflow are discussed in Section 3.2. A full production problem and validation of the workflow are discussed in Section 3.3.

3.1 Implementation

The mesh-based RNUCS-R2S workflow for accelerator-driven systems is a collection of scripts that form a sequential workflow to perform an SDR analysis. Figure 3.1b shows a flowchart representation of this workflow. In contrast, Figure 3.1a shows the cell-based RNUCS- R2S workflow, including a geometry splitting step.

3.1.1 Particle Transport and Geometries

In this work, all transport calculations are done directly on a CAD geometry using DAGMC. DAGMC [10] is a toolkit that facilitates ray tracing on a CAD geometry used for particle tracking during transport. A DAGMC geometry is a CAD geometry that has been faceted. The DAGMC toolkit can be coupled with various MC physics codes [22]. In this work, DAGMC is used in conjunction with MCNP6 [9].

3.1.2 Step 1: Full Radiation Transport

The first step of the mesh-based RNUCS-R2S workflow for accelerator-driven systems is a full three-dimensional radiation transport. In this step, the neutron flux with energy less than 20 MeV and the nuclide production and destruction rates from interactions with neutrons

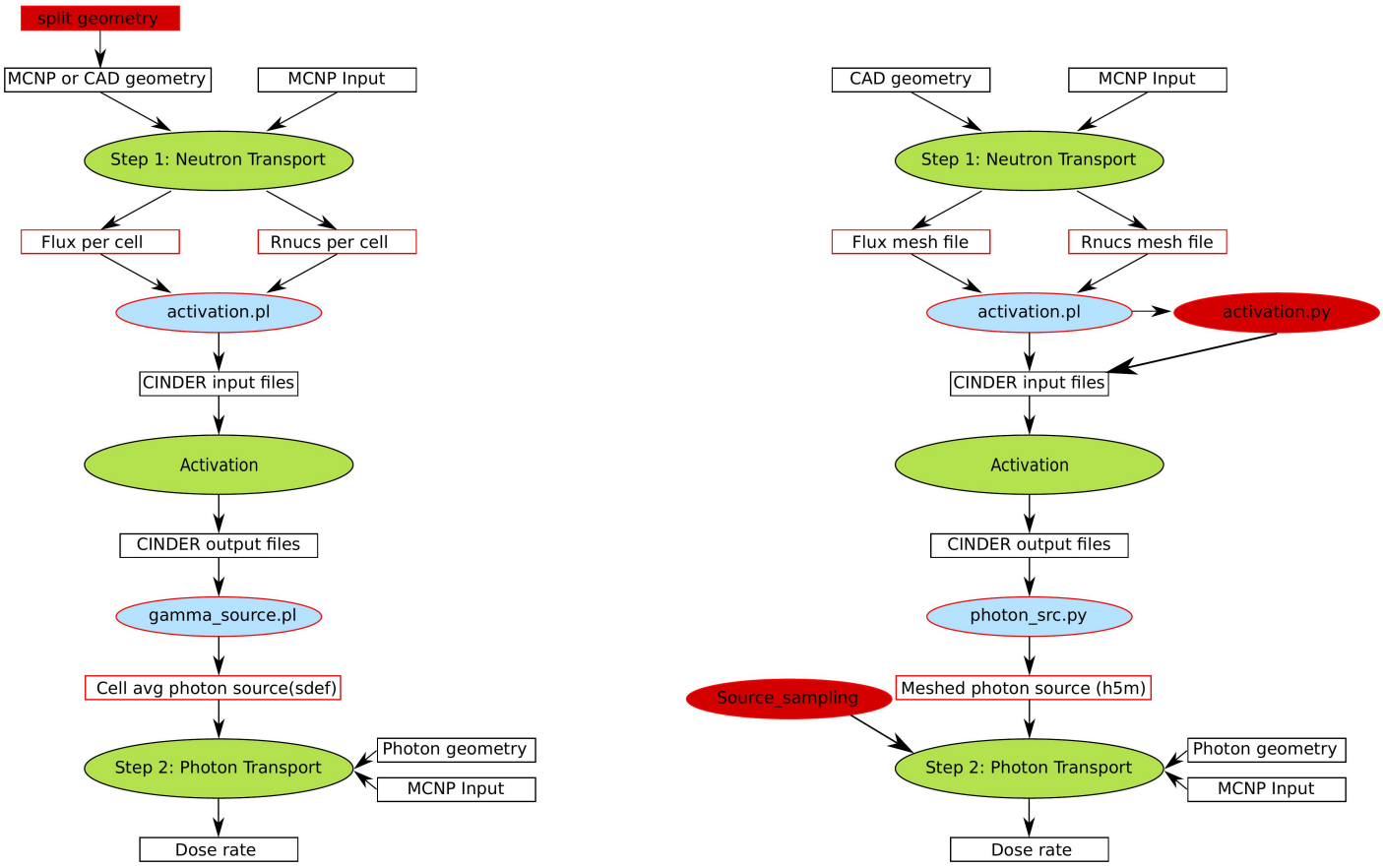

Figure 3.1: RNUCS-R2S workflow for accelerator-driven systems: a cell-based b mesh-based

of energy greater than 20 MeV and charged particle interactions are tallied in a Cartesian mesh superimposed in a region of interest.

The MCNP track length tally is able to tally flux in an arbitrary Cartesian mesh, while the original special tally, RNUCS, did not have this capability. Changes to the MCNP source code were made to extend this tally to function with an arbitrary Cartesian mesh. This implementation tallies information at each high-energy particle collision which is described by the collision estimate of a reaction rate for reaction type x given by Equation 3.1.

$$R_x = \frac{1}{W} \sum_{i \in A} \sum_{g} \frac{w_i \Sigma_x(E_{i,g})}{\Sigma_t(E_{i,g})}, \tag{3.1}$$

where W is the total starting weight, w_i is the weight of the particle before the collision, A

is the set of all events resulting in reaction x, g is the energy group of interest, $\Sigma_x(E_i)$ is the macroscopic cross-section for reaction x at the incoming energy of the particle, $\Sigma_t(E_i)$ is the total macroscopic cross-section at particle incoming energy E_i. The macroscopic cross-sections, in Equation 3.1, are collected via physics models existing in MCNP.

The nuclide production and destruction rate tallied per nuclide are written into a file, *r_mesh*, analogous to the *meshtal* MCNP file. This tally is currently implemented in MCNP6.1 and MCNP6.2. In this implementation, it is possible to specify the geometric cell(s) to select materials in which to collect production and destruction rates. This, in turn, means that it is possible to tally information from interactions occurring at specific materials within the mesh. If no geometric cell is specified, then production and destruction rates are collected for all space covered by the Cartesian mesh and all materials present. When two or more geometric cells are specified that have different materials, only one superset of nuclides produced or destroyed will be reported by the tally.

3.1.3 Coupling Step: Activation

An activation calculation is done for each mesh volume element of the mesh defined in the full transport. A mesh-based photon source is constructed from the results of the activation calculation. This mesh-based photon source is used in the second transport step. A python script has been written to automate this step. This script collects the neutron flux, and the nuclide production and destruction information from the MCNP output. It also obtains material composition, writes CINDER'90 input files, and runs an activation calculation for each mesh volume element.

It is important to note that the material composition for each mesh volume element might be a homogeneous mixture of two or more materials. This homogenization happens because superimposed Cartesian meshes are not typically conformal to the geometric volumes; therefore, a mesh volume element can have multiple geometric volumes and multiple materials. The PyNE toolkit [23] is used to determine the material composition of any given

mesh. PyNE calculates the cell volume fractions of each mesh volume element using ray tracing with DAGMC. It uses these fractions to create a homogenized material definition for the volume element.

The activation script has been written to work with CINDER'90, which is an activation code that can take an extra term to account for nuclear inventory produced or destroyed in energies outside the domain of nuclear data libraries [13].

3.1.4 Step 2: Decay Photon Source Construction and Decay Photon Transport

In the photon transport step of the mesh-based RNUCS-R2S workflow for accelerator-driven systems, photon emission densities are defined on a mesh. A *photon_source* script has been written to construct the photon source in the mesh. This script reads in the output of the activation calculation per volume element and writes the appropriately formatted information to an HDF5 file. This HDF5 representation of the source mesh is used in conjunction with the PyNE sampling module in lieu of a traditional MCNP source card [23].

3.2 Verification Problem

A suite of verification runs has been performed to ensure the correct implementation of the mesh-based RNUCS-R2S workflow. The geometries, source, irradiation history, and other features used in the verification problem were modeled after similar conditions seen in accelerator-driven systems. The SDR results were compared to the SDR results from the cell-based RNUCS-R2S workflow.

Two geometries were used for the verification runs. The geometry used for the mesh-based RNUCS-R2S workflow is shown in Figure 3.2. This geometry represents a simplified model of a steel target vessel filled with mercury. The geometry used for the cell-based

RNUCS-R2S workflow is shown in Figure 3.3. This geometry is the same geometry seen in Figure 3.2 but split into smaller volumes.

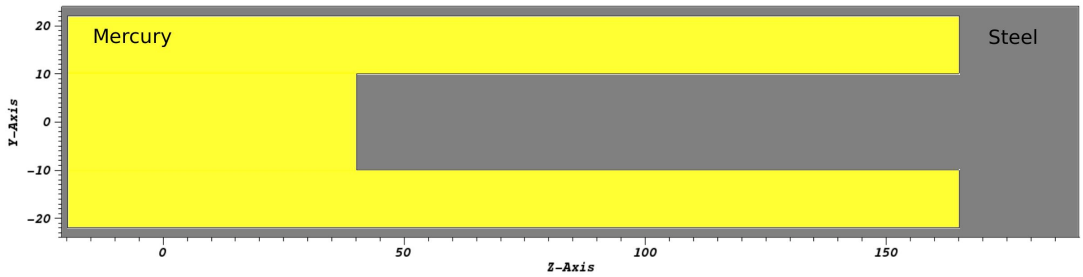

Figure 3.2: Cross-sectional cut at x = 0 of mesh-based RNUCS-R2S workflow geometry

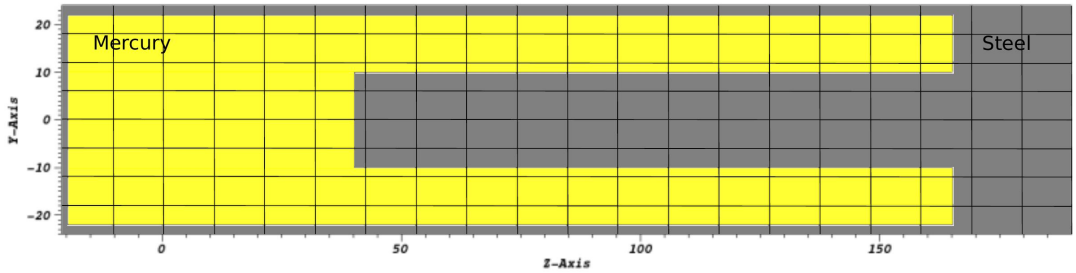

Figure 3.3: Cross-sectional cut at x = 0 of cell-based RNUCS-R2S workflow geometry

In both problems, the source used was the full source typically used on a full SNS analysis. This source is a 1.0 MW proton beam incident on the geometry with Gaussian energy distribution centered at 1 GeV and positioned on the left side of the geometry in the XY plane at z = -257 cm.

Three different meshes were used with the mesh-based workflow: coarse, medium, and fine mesh. The coarse mesh was arbitrarily chosen to be a uniform Cartesian mesh of 4x8x20 mesh volume elements. The medium mesh is based on the coarse mesh with extra fidelity near the mercury and steel boundary where flux gradients are high. The fine mesh adds even more fidelity to these material boundaries. A material-aligned mesh is not typically possible with a Cartesian mesh for complex geometries. Although it is easy to choose a Cartesian mesh that aligns with material boundaries for this simple geometry, the meshes were chosen to mimic how an analyst might choose an appropriate mesh for more complex geometries.

Table 3.1: Irradiation Schedule used for activation

Period (days)	Mean Power (kW)	Period (days) cont.	Mean Power (kW) cont.
14	0.00	7	0.00
7	682.23	7	0.00
7	731.39	7	0.00
7	770.78	7	0.00
7	770.93	7	0.00
7	675.72	7	185.59
7	533.22	7	888.73
7	1002.40	7	821.50
7	1158.50	7	1116.80
7	1118.00	7	811.60
7	1007.80	7	1083.60
7	875.56	7	1173.70
7	0.00		

For the cell-based workflow, the split geometry (Figure 3.3) was used. This split geometry aligns with the coarse mesh. An activation calculation was performed using the 38-week irradiation schedule given in Table 3.1. The photon transport step used a reduced-density mercury model to mimic the trace mercury left after mercury drainage, which typically occurs for spent targets after shutdown. The photon emission density from the activated trace mercury contributions, is ignored in this problem because these contributions are negligible compared to the steel contributions. Only the contribution from the activated steel at 106 days after shutdown is used to construct a photon source for each of the four problems. The SDR is obtained using SNS specific flux-to-dose conversion factors [24] with the tallied photon flux.

3.2.1 Full Radiation Transport

The neutron flux below 20 MeV, and the nuclide production and destruction rates from neutron interactions above 20 MeV and from charged particle interactions were collected during the neutron transport. The nuclide production and destruction from interactions above 20 MeV were tallied separately for the mercury and the steel materials.

Figure 3.4 shows the production rates collected from interactions in the mercury target

in the cell-based and mesh-based workflow. The production rates shown in Figure 3.4 are from the mercury geometry volumes and the coarse mesh. Figures 3.4a and 3.4b show the

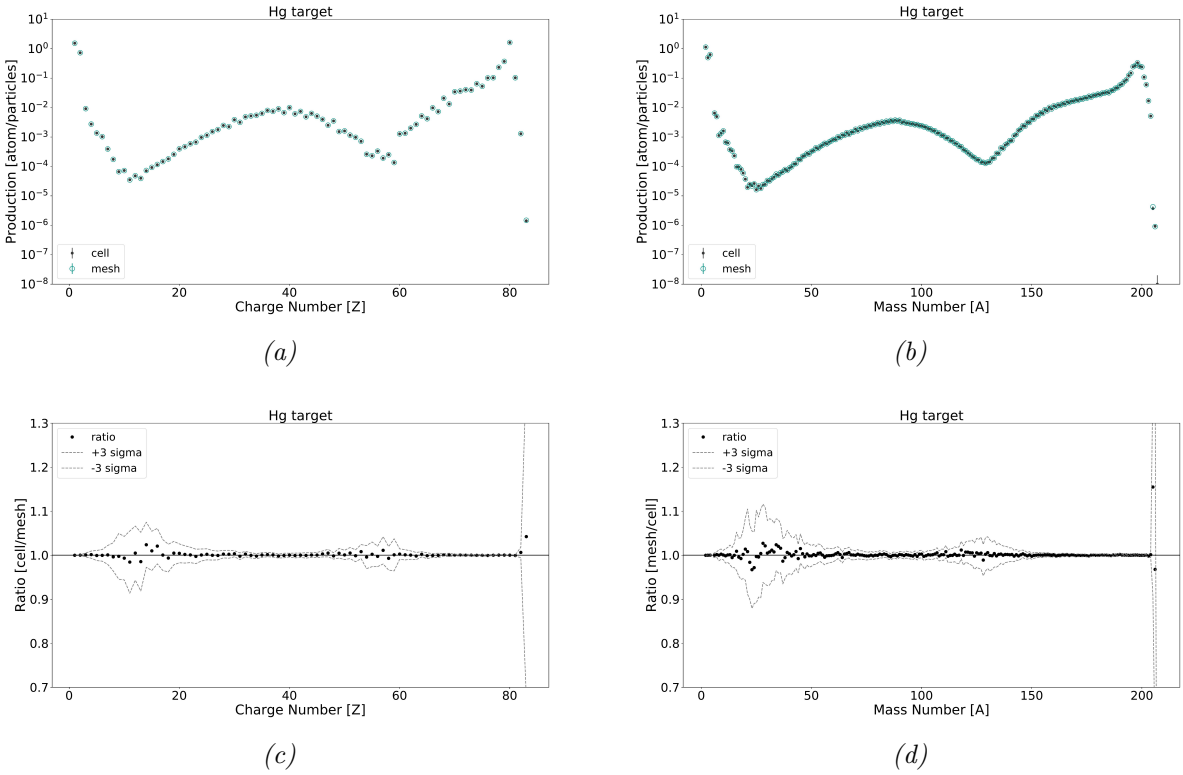

Figure 3.4: Distribution of charge and mass number of production rates of nuclides in Hg target

distribution of charge number (Z) and the mass number (A). Figures 3.4c and 3.4d show the ratio between the coarse mesh and cell-based results. The ratio between the mesh-based and cell-based workflows indicates good agreement for the production rate obtained with both workflows. Figure 3.5 shows a histogram of the nuclide production distribution ratio (mesh/cell) of all nuclides created in the mercury volume. This histogram also shows how each of the nuclides created compares between the workflows, and indicates good agreement between the mesh-based and cell-based workflow results. This histogram shows that the ratio of most nuclides is close to one. Some nuclides show a ratio of zero; these nuclides account for seven percent of all nuclides and arise from rare event outcomes of low-probability radionuclides. A ratio of zero means that a nuclide was produced in one workflow but not produced for the other. It is also important to note that the ratio axis was cut off at a ratio

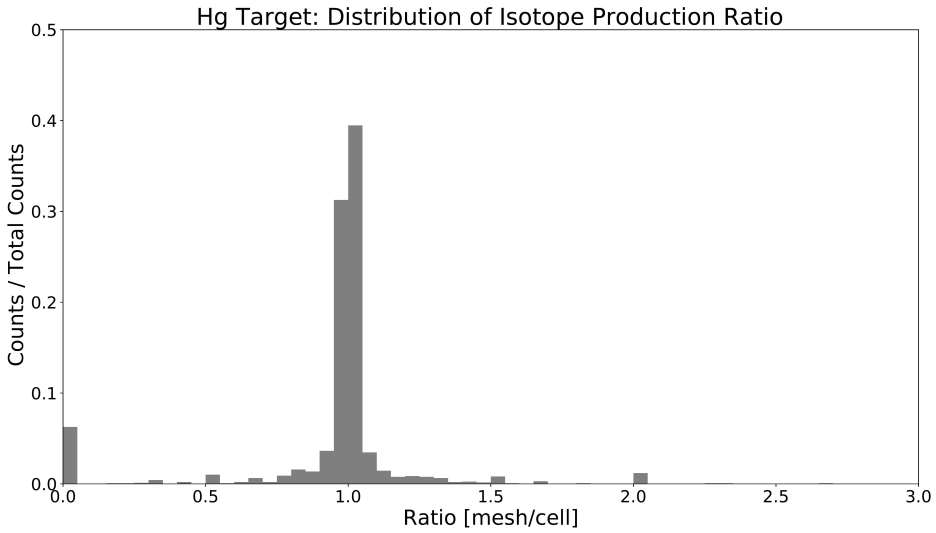

Figure 3.5: Nuclide production ratio [mesh/cell] for Hg target

of three. Five out of 2331 nuclides have a ratio greater than three and are out of the bounds of Figure 3.5.

Figure 3.6 shows the charge number and mass number distribution for nuclides created from interactions in the steel volume. A similar trend is seen in these plots as seen in the mercury volume. The ratio in Figures 3.6c and 3.6d show good agreement between the mesh-based workflow and the cell-based workflow. Figure 3.7 shows the ratio distribution of all nuclides produced in the steel volumes. The distribution is mainly centered at a ratio of one, with some nuclides showing a ratio of zero. In this plot, the ratio axis was also cut off at a ratio of three. There are 5 out of 633 total nuclides with a ratio larger than three and therefore outside the bounds of Figure 3.7.

The neutron flux was tallied for all volumes in the cell-based workflow and over the entire mesh in the mesh-based workflow. Figure 3.8 shows the neutron flux along the X, Y, and Z-axis for the cell-based workflow and each of the three meshes. The tallies used for the neutron flux are track length tallies, and the neutron flux is averaged over the geometric volume and the mesh volume element. Figure 3.8 shows that a finer mesh is better able to catch flux gradients.

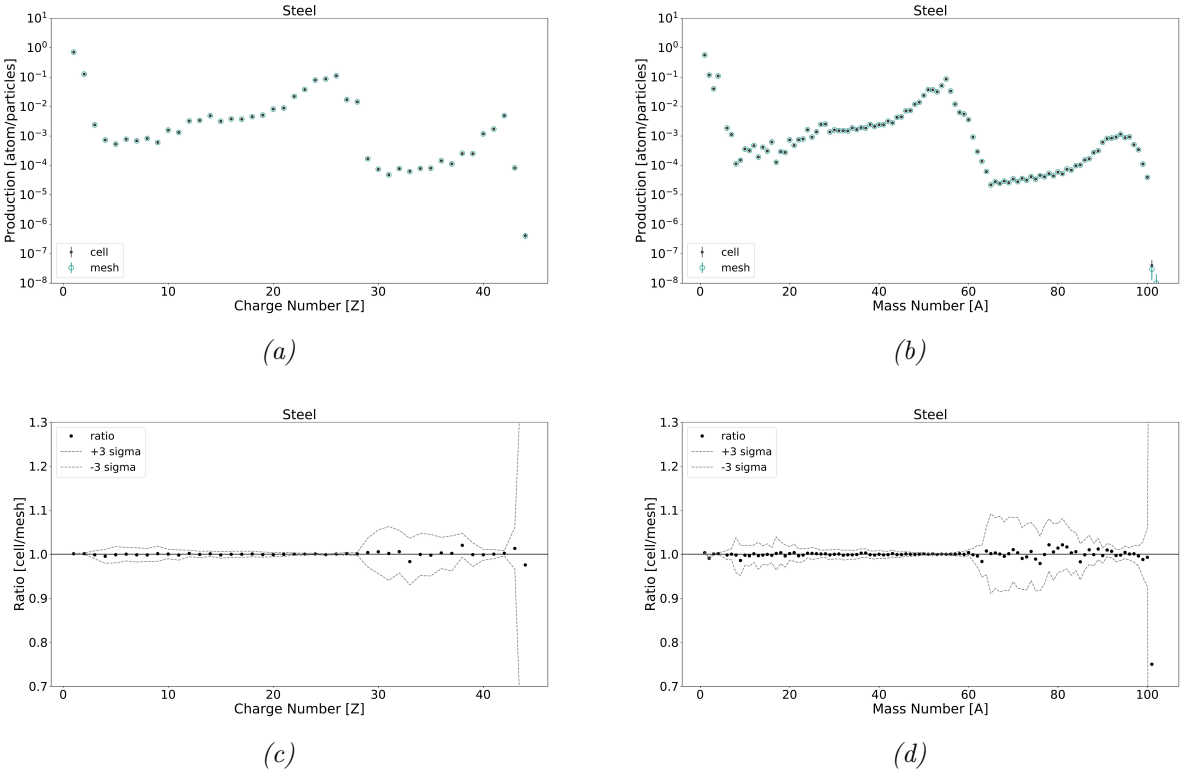

Figure 3.6: Distribution of charge and mass number of production rates of nuclides in the steel volume

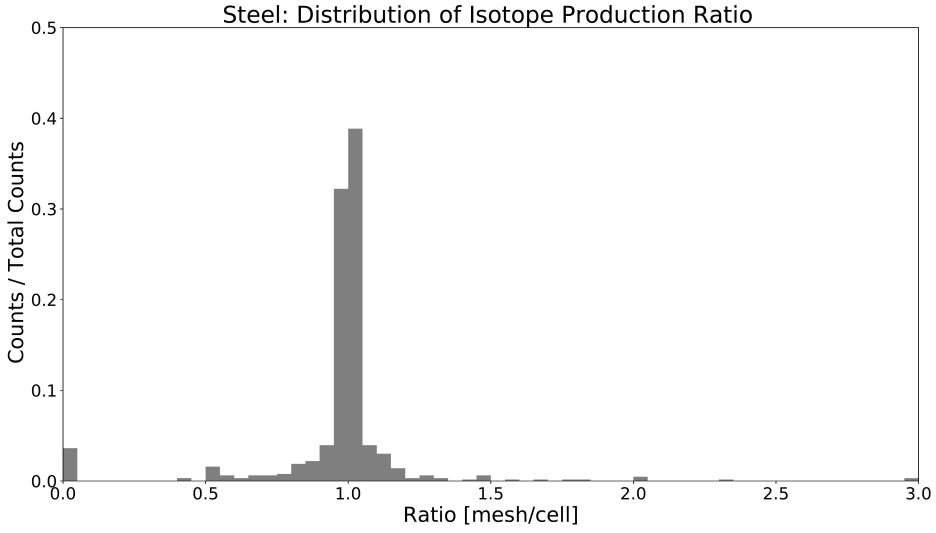

Figure 3.7: Nuclide production ratio [mesh/cell] for steel volume

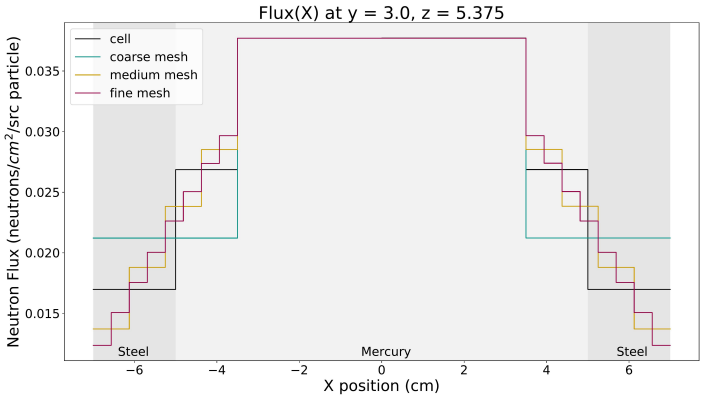

(a)

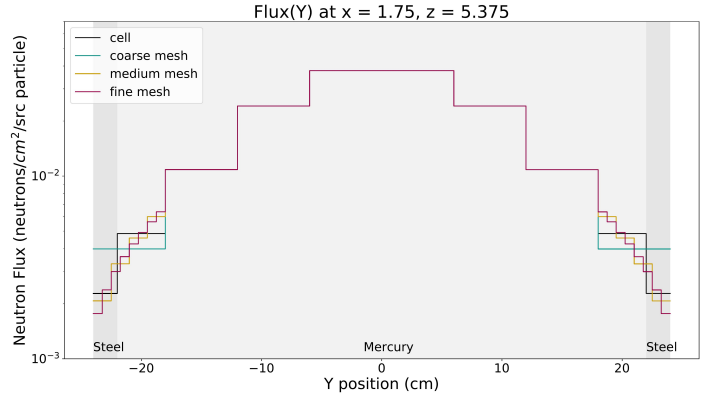

(b)

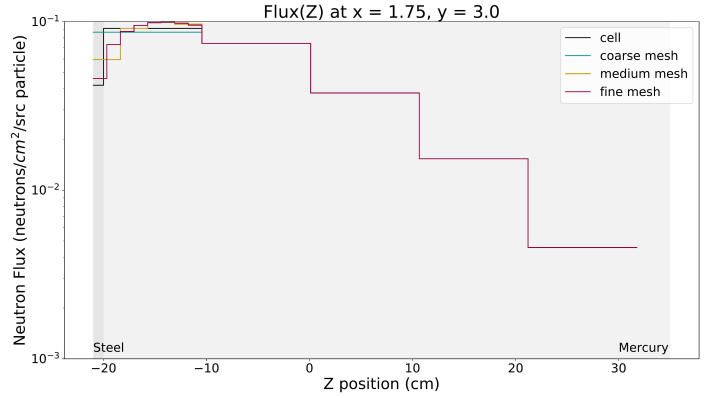

(c)

Figure 3.8: Neutron flux from cell-based and mesh-based workflows

3.2.2 Activation

Steel activation was the primary focus for these problems because the mercury is drained after shutdown, and only trace amounts of mercury are modeled. It is possible to also account for

the mercury contribution, but as they are small, these contributions are not being considered in this problem. An activation calculation was performed for each steel volume in the cell-based workflow, and for each mesh volume element containing steel material for the mesh-based workflow. Mesh volume elements that contained only mercury had a void material definition, and no activation was recorded. For mesh volume elements that contained a mixture of both materials, the mercury volume was defined as void to avoid activating the mercury. The nature of the activation calculation is as if the steel is dispersed over the whole mesh volume element. The flux averaged over the mesh volume element for the less than 20 MeV neutrons was used, and the high-energy production and destruction rates for nuclides created in steel only were used in the activation calculation of mesh volume elements with mixed materials.

Figures 3.9a - 3.9c show the photon emission density at 106 days after shutdown from steel activation for the cell-based workflow and mesh-based workflow. These figures show that the best estimation of the photon emission density occurs when using the fine mesh. The coarse mesh has the most significant difference in photon emission density compared to the results from the cell-based workflow. This significant difference is because, in the coarse mesh, quantities like the neutron flux are averaged over larger volumes. This can lead to smearing out of large flux gradients, which in turn leads to an incorrect photon emission density. Let us take a mesh volume element of the coarse mesh with a small steel volume fraction as an example. In neutron transport, the neutron flux is overestimated compared to the actual value. The amount that the neutron flux is overestimated depends on the flux gradient in the region. The nature of the *rnucs* tally allows for obtaining only the production and destruction rates of nuclides in the steel. In the activation step, the steel material is spread out over the whole mesh volume element since the mercury is turned off during activation and treated as void. This means that the photon emission density is also averaged over this volume. Although a reasonable estimation of the photon source strength is possible, if the neutron flux is a good approximation to the true value, averaging the source

strength over the mesh volume element means we have a lower photon emission density. This becomes important as the photon emission density is used as the source for photon transport.

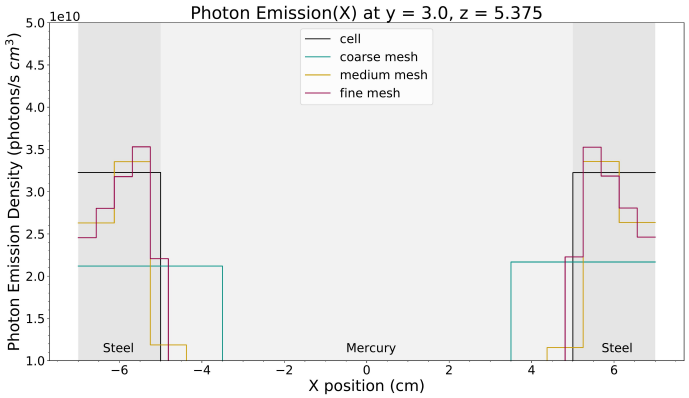

(a)

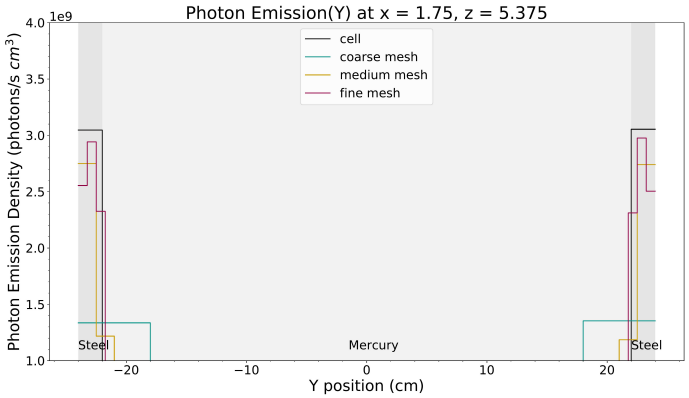

(b)

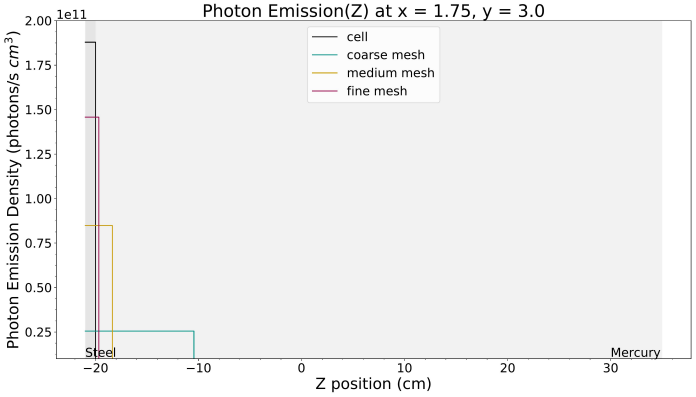

(c)

Figure 3.9: Photon emission density from steel activation 106 days after shutdown

3.2.3 Decay Photon Transport

The results from the steel activation calculation at 106 days after shutdown were used to define a photon source. One source was created for the cell-based workflow, and one source was constructed for each mesh: coarse, medium, and fine mesh. A photon transport calculation was performed with each photon source and the low-density mercury model. The SDR was tallied in two mesh tallies placed above and to the front of the geometry. Figure 3.10 shows the dose rate [mrem/hr] for the cell-based workflow and each of the meshes.

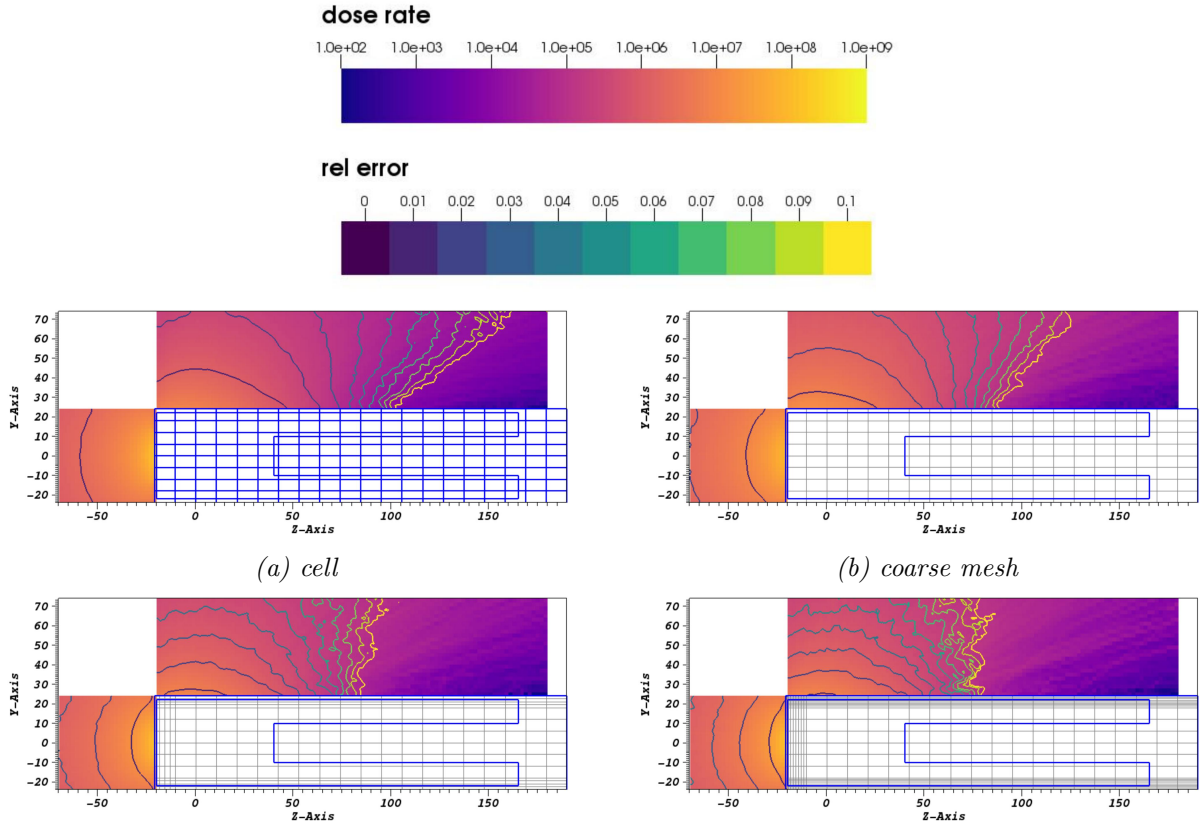

(a) cell *(b) coarse mesh*

(c) medium mesh *(d) fine mesh*

Figure 3.10: SDR from steel source at 106 days after shutdown

Figure 3.11 shows the ratio between the SDR from the mesh-based workflow and the SDR from the cell-based workflow. Figure 3.11a shows significant differences between cell-based and mesh-based workflow SDR for the coarse mesh. A possible explanation for this

significant difference is that the mesh used for the neutron flux is not capturing important differences in the neutron flux of the steel volumes.

The coarse mesh does not have an appropriate resolution to capture the flux gradient near the steel and mercury boundaries. The mesh volume elements of the coarse mesh contain a small steel volume fraction and a larger mercury volume fraction. It is also important to note that, in the cell-based workflow, the neutron flux is averaged over a volume containing only the material of interest. In the mesh-based workflow, the neutron flux can be averaged over a region containing more than one material, leading to overestimation or underestimation of the neutron flux.

When the mesh is selected with the properties of the system in mind, the SDR results between the two workflows are in better agreement. The medium and finer meshes add resolution near the steel and mercury boundaries to better capture the neutron flux gradient. Figure 3.8 shows how each mesh captures the flux gradients.

Figures 3.11b and 3.11c show the SDR ratio between the medium mesh and cell, and between finer mesh and cell. These figures show a significant improvement when comparing the mesh-based workflow to the cell-based workflow. These results suggest that the Cartesian mesh should be chosen carefully. A good mesh would be chosen based on the system and with enough detail in areas of large gradients. These results also show that with the appropriate choice of mesh, a good estimation is possible. In this verification problem, adding the appropriate mesh fidelity was a relatively easy task because of the simplicity of the geometry. A more complex geometry might benefit from an analyst expert on the system to choose the most appropriate mesh. It is relatively easy to try different meshes and choose the best fit for the problem. This is an advantage to splitting the geometry into smaller pieces, which requires knowledge of the system and can be very complicated for a complex system, and labor intensive.

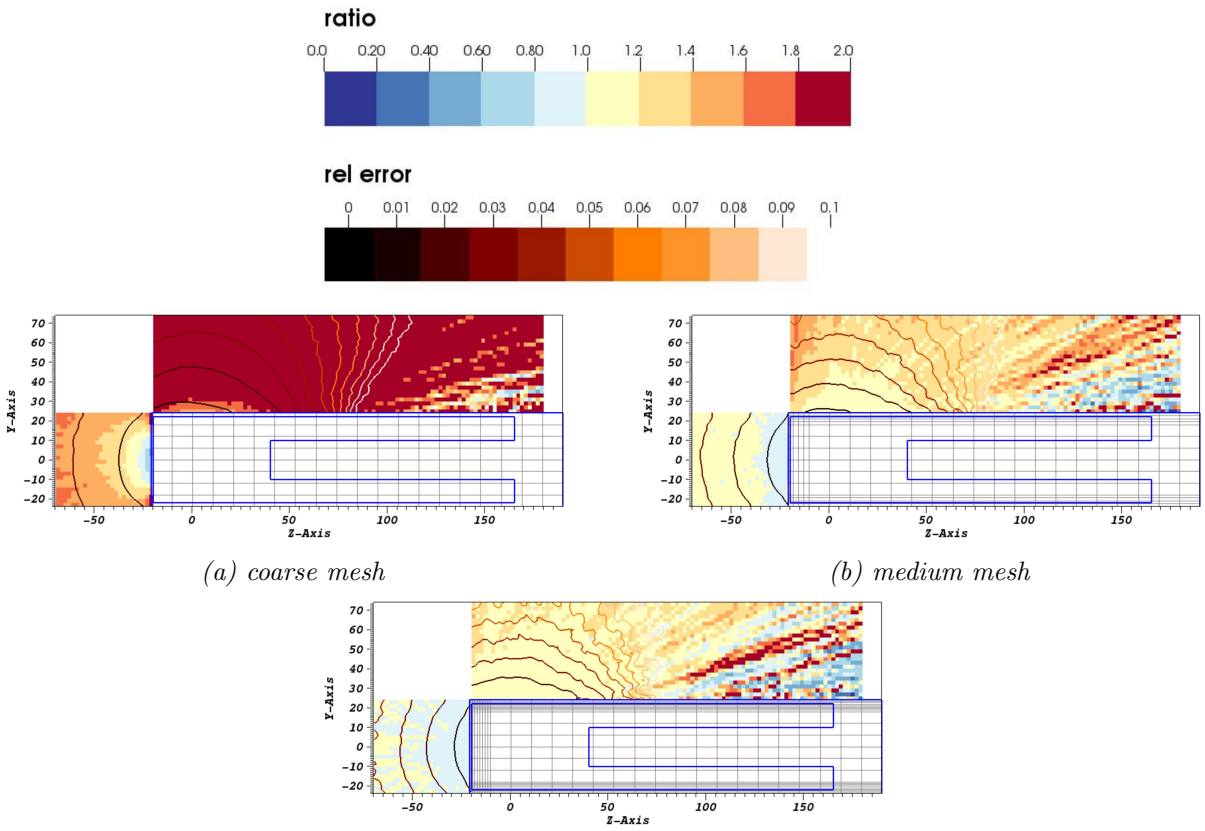

(a) coarse mesh

(b) medium mesh

(c) fine mesh

Figure 3.11: Ratio of dose rates from mesh-based workflow to cell-based workflow

3.2.4 Material Aligned Demonstration

The previous verification problems show that the choice of mesh is important and problem-dependent. A poorly chosen mesh can lead to ill-suited flux estimates leading to over- or under-estimation of final results. A problem has been set up to demonstrate that if a mesh that perfectly matches the cell-based problem is chosen, the final results in both workflows are not significantly different. A slight modification is made to the mesh to demonstrate the effects of a simple mesh alteration.

The problem setup geometry for the mesh-based and cell-based workflows was a smaller version of the geometries shown in Figures 3.2 and 3.3. Both geometries were reduced by 1/32 in volume. A simple disk source uniformly emitting 1 GeV protons was used. The source was placed perpendicular to the z-axis 15 cm away from the geometry. These changes

were made to ensure results with a good statistical error in a reasonable amount of time.

The first mesh used for the mesh-based workflow was chosen so that each mesh volume element corresponded to one geometric cell of the cell-based geometry. Each mesh volume element consisted of only one material. Both workflows were run to obtain the biological dose rate on two tallies: one above and one on the side of the geometry. Figure 3.12 shows the ratio between the mesh-based workflow and the cell-based workflow. This figure shows that the biological dose rate between the two workflows is within a 5% difference and statistical error less than 1%. Furthermore, a Z-value test was performed for both tallies, and the PDF and CDF are shown in Figures 3.13 and 3.14, respectively. The Z-value test shows that about 90% of the results in both tallies are within 2σ and over 98% within 3σ. Table 3.2 contains a summary of these values.

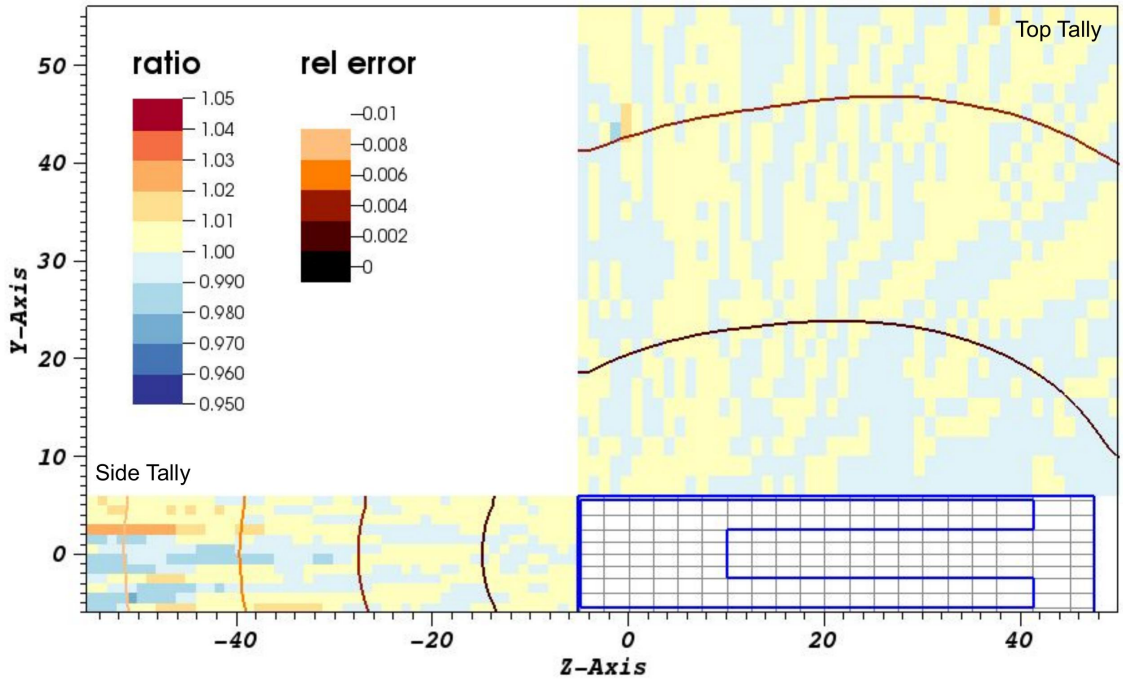

Figure 3.12: Material-aligned dose rate ratio [Mesh/Cell]

The second mesh used was a uniformly distributed mesh with the same number of mesh volume elements as the material-aligned mesh. In this mesh, there is material homogenization as the mesh does not align with volume boundaries. Figure 3.15 shows the ratio between

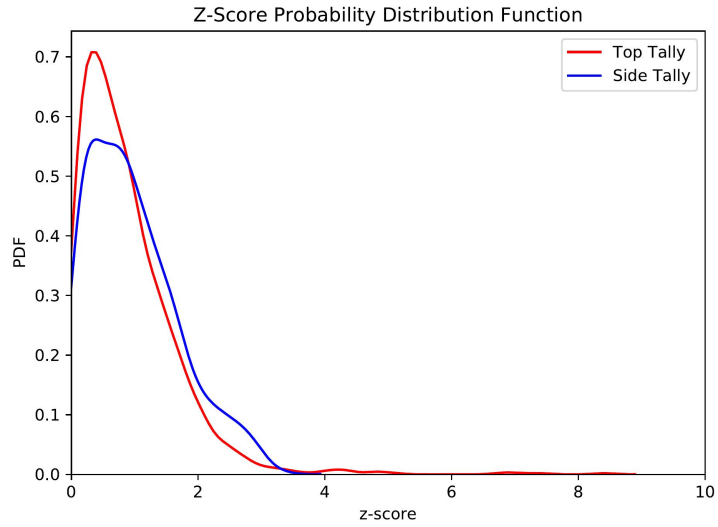

Figure 3.13: Probability Distribution Function

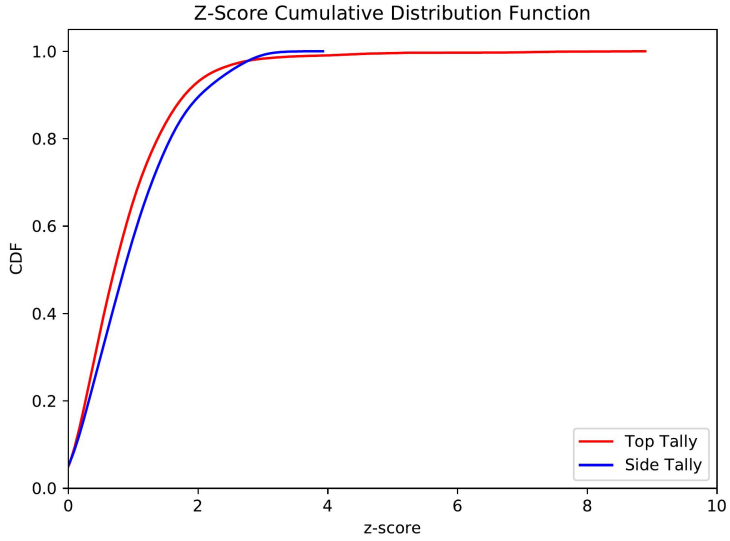

Figure 3.14: Cumulative Distribution Function

	Top Tally	Side Tally
$z \leq 2$	93.1%	89.8%
$z \leq 3$	98.3%	99.7%

Table 3.2: Z-test results

the two workflows for this mesh. This figure shows a discrepancy of up to 40% between the two workflows.

This problem shows that both workflows agree almost perfectly if a good mesh is chosen.

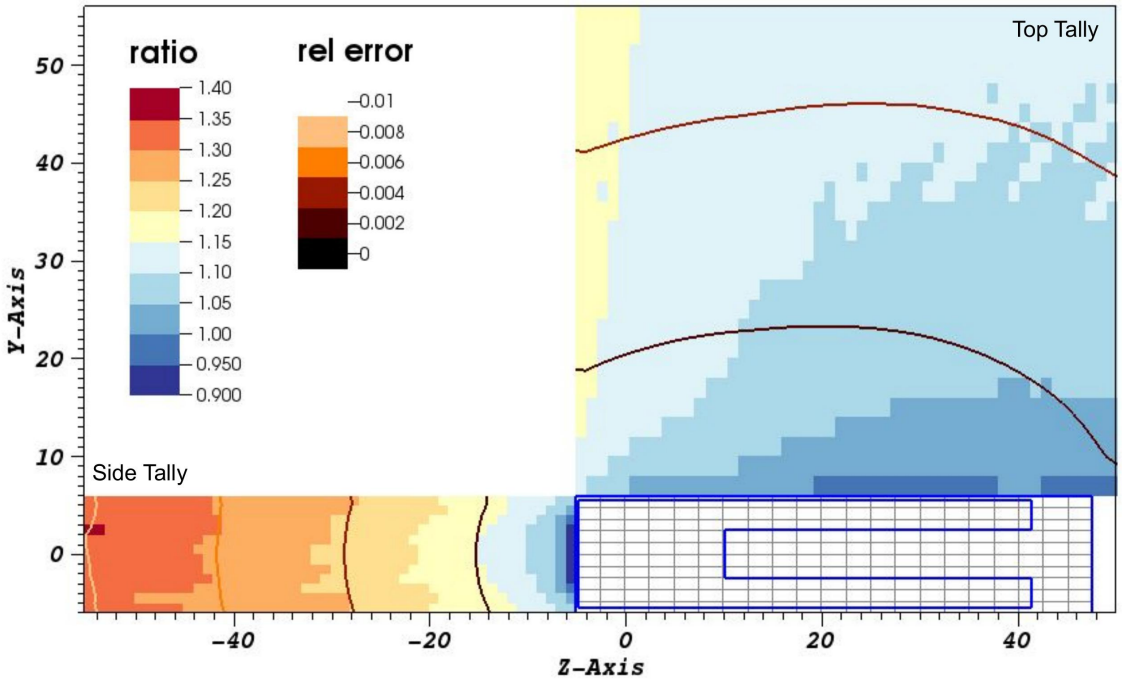

Figure 3.15: Non-material-aligned dose rate ratio [Mesh/Cell]

On the other hand, if a mesh does not perfectly fit the volumes of the cell-based problem, then discrepancies between the two workflows can show up due to material mixing and overestimating fluxes. In this simple problem, a simple change in mesh use led to a change of up to 40%. For more complex problems, a poor choice of mesh can lead to significant differences.

3.3 Demonstration

The mesh-based RNUCS-R2S workflow was also demonstrated using a full production model of the SNS system. A full workflow was completed to obtain SDR at three mesh tallies placed around the drained target assembly. The SDR mesh tally results were compared to tally results from a cell-based RNUCS-R2S workflow. The full production SNS model was also used to do a preliminary validation using SDR results at eleven detectors placed around the target assembly. The SDR results at the detectors were compared to experimental values

obtained from Popova *et al.* [6], and to the SDR results obtained with a cell-based RNUCS-R2S workflow using the setup described in [6].

The full SNS geometry used in this problem can be seen in Figure 3.16. A 1 GeV proton source is positioned on the left side of the system. The region of interest is the target module of the SNS system. A Cartesian mesh with 8256 elements superimposed over the target region was used in this work. The target module geometry used in the cell-based workflow has been divided into 250 small volumes.

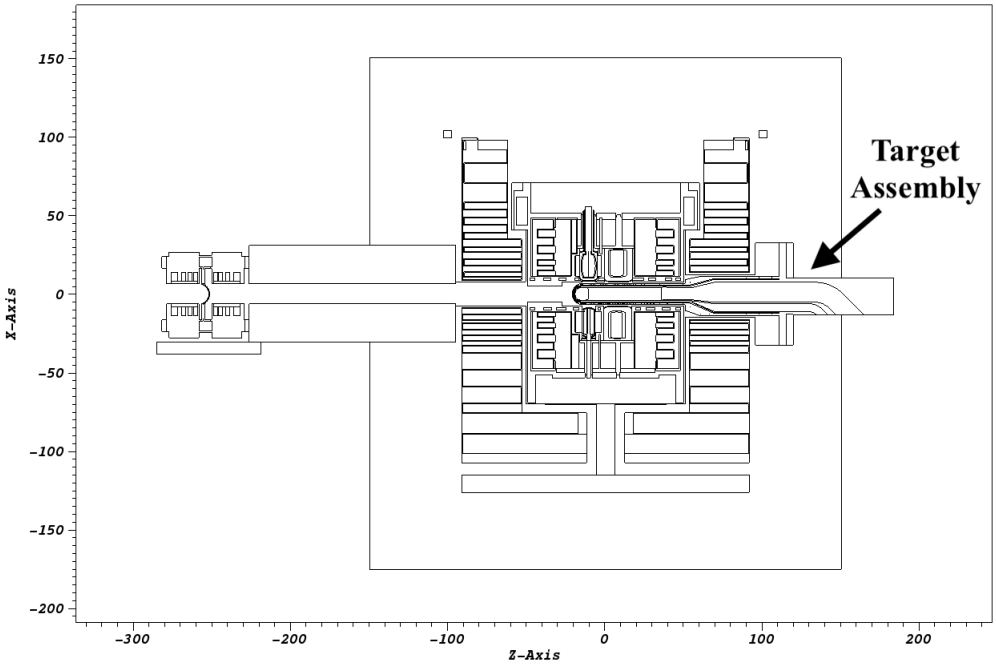

Figure 3.16: Cross-sectional view of SNS geometry at y=0

After an activation calculation, a mesh photon source was constructed from the photon emission density at 106 days after shutdown. This photon source was used for a photon transport calculation for the extracted and drained target vessel. The SDR was tallied in three meshes placed above and to the sides of the target module. One of the mesh tallies is set in the X-Z plane, and two in the Y-Z plane. The figures showing the dose rates in these tallies have been transposed into a 2-D representation. Figure 3.17 shows the coordinate

transposition.

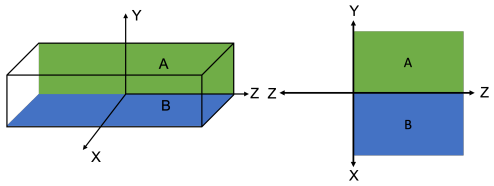

Figure 3.17: Representation of 3D to 2D

Figures 3.18a and 3.18b show the SDR results obtained with the cell-based workflow and with the mesh-based workflow, respectively. Figure 3.19 shows the ratio between the

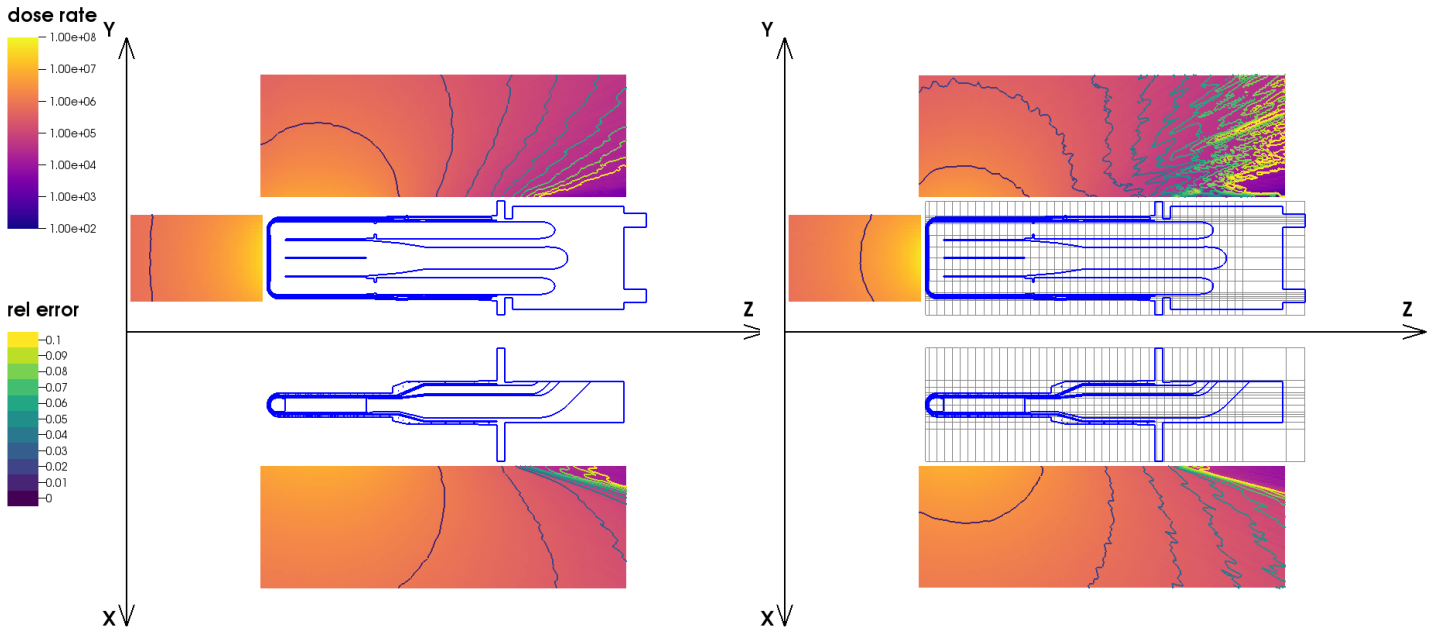

(a) Cell-based workflow *(b) Mesh-based workflow*

Figure 3.18: Biological Dose Rate [mrem/hr]

mesh-based workflow SDR and the cell-based workflow SDR. The SDR in the front tally shows that the mesh-based workflow overestimates the results compared to the cell-based workflow results by about 20%. The tally in the X-Z plane shows a difference between the two workflows of up to 50%. Both of these tallies are within a reasonable agreement.

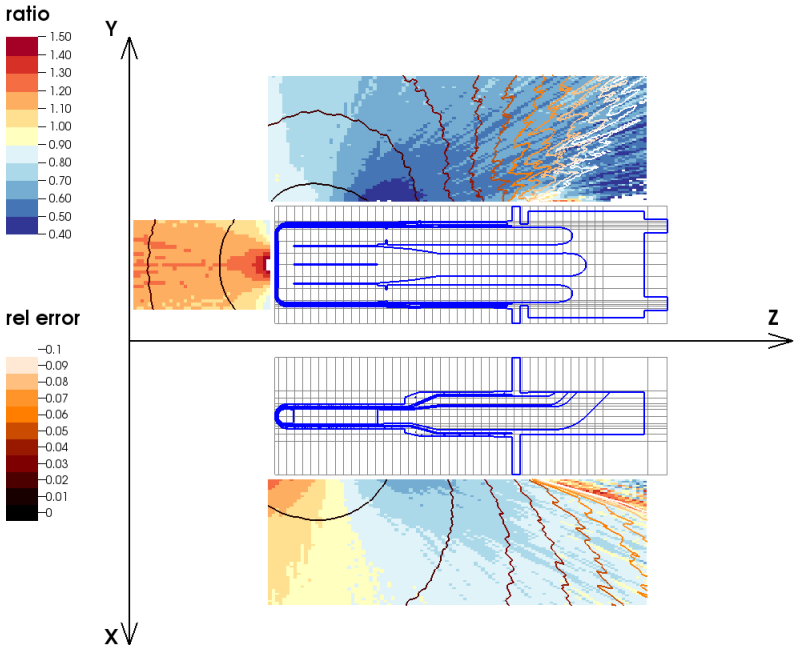

Figure 3.19: Ratio (Mesh/Cell)

The top tally in the Y-Z plane is a little more complicated in that it always underestimates the results and often by a significant amount. The SDR in this tally is always underestimated when compared to the SDR from the cell-based workflow. The best ratios occur near the front of the target, and the ratios decrease as we move towards the back of the target. Many factors could be contributing to this difference. The first contributing factor is the neutron transport mesh choice. This mesh is essential to correctly capture the neutron flux gradient, which affects the photon emission density and, therefore, the SDR results. Furthermore, a Cartesian mesh is not best suited to capture the complexity of the geometry as it is not conformal to the volumes. The SNS geometry consists of rounded components, which are difficult to capture with a Cartesian mesh. Another important difference to note is in geometry used in the two workflows. In the mesh-based workflow, the target module is represented by a CAD model, which is composed of four large volumes, each with a different material. In contrast, in the cell-based workflow, the target module is represented in native

MCNP geometry with around 250 small volumes.

The SDR was also calculated for 11 detectors positioned 30 centimeters away from the target, and Figure 3.20 shows the positions of the detectors. The flux-to-dose conversion rates improved for use with SNS[24] were used with the tallied photon flux to obtain the SDR.

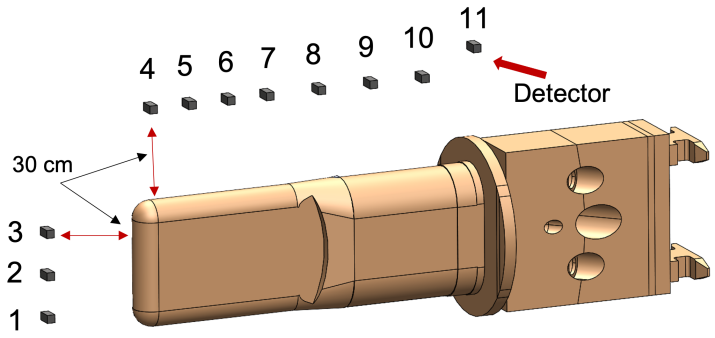

Figure 3.20: Detectors as positioned around the out-of-service target for SDR measurements

Figure 3.21 shows the experimental SDR, the mesh-based RNUCS-R2S SDR results, and the cell-based RNUCS-R2S SDR results. Figure 3.21 shows that the cell-based workflow overestimates the SDR on all detectors while the mesh-based workflow varies in estimation. The mesh-based workflow overestimates the SDR results at the front of the target vessel and underestimates the SDR results at the back of the target vessel. This is further demonstrated in Figure 3.22, which shows the ratio of both workflow results to the experimental values.

The ratio plot shows that the cell-based results overestimate the SDR by 15 % to 55%. The mesh-based workflow overestimates the SDR on the front three detectors by about 40%, which is similar to the cell-based results for the same detectors. Detectors 4 and 5, which are near the front of the target vessel, underestimate the SDR by up to 25%. Furthermore, five out of the eleven detectors are within 50% agreement, and seven out of the eleven detectors are within a factor 2 agreement. The last four detectors underestimate the SDR by a factor greater than 2. Results within a factor of 2 are considered a reasonable agreement, and anything above is regarded as a significant discrepancy. One reason for the large discrepancy

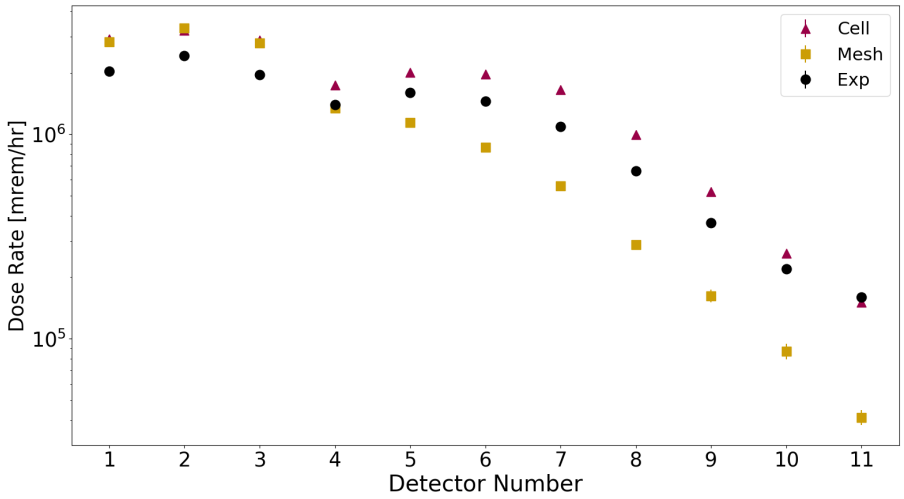

Figure 3.21: SDR at detectors

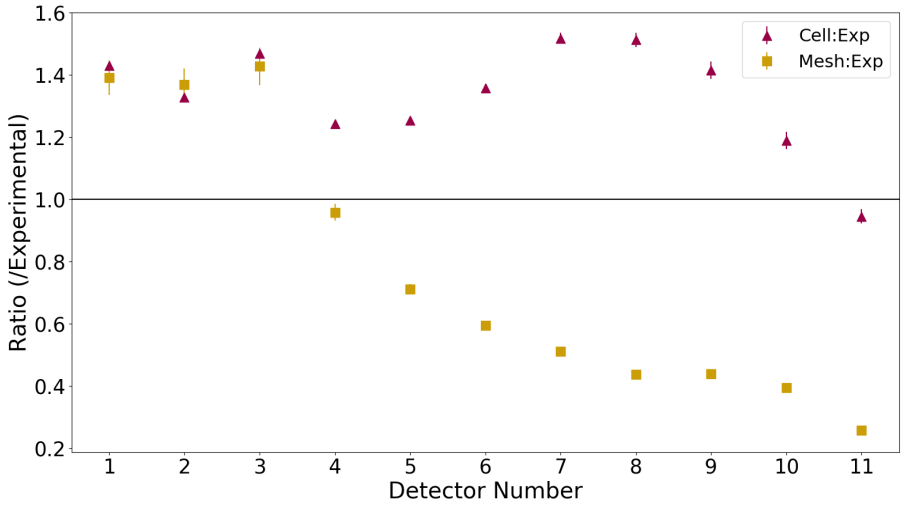

Figure 3.22: Ratio of SDR (Simulation/Experimental)

in the back detectors is the choice of Cartesian mesh. An expert analyst familiar with the system might choose a more appropriate mesh that captures significant flux gradients. It is also worth mentioning that even if the choice of mesh is not immediately clear, an analyst is able to try different meshes or even run a mesh sensitivity analysis with relative ease. Other reasons for the discrepancy include uncertainty in the calibration of the detectors, approximation in geometry definition, and approximation of the geometry materials in the

mesh used in the workflow.

Overall, the mesh-based RNUCS-R2S workflow was able to perform well compared to the cell-based RNUCS-R2S workflow and fair compared to the experimental results. An advantage to using the mesh-based workflow lies within the geometry setup. For the cell-based RNUCS-R2S workflow, an analyst must be familiar with the design of the system to split the geometry into small enough pieces to capture important features. Splitting the geometry into smaller pieces is tedious and time-consuming work. In the mesh-based RNUCS-R2S workflow, the analysts must choose an adequate mesh, which requires less time to set up the problem.

3.4 Conclusion

The mesh-based RNUCS-R2S is a novel Cartesian mesh-based R2S workflow for accelerator-driven systems. This workflow operates directly on CAD geometry and supports the construction of a mesh-based photon source. These new capabilities help reduce human errors that might result from creating a native MCNP geometry and the splitting of this geometry. The mesh-based RNUCS-R2S workflow has been verified against the cell-based RNUCS-R2S workflow. A test problem for each workflow was created containing materials and sources that create high-energy neutrons. The SDR results between these two workflows show agreement within 40%. Additionally, a simple test problem was set up with a carefully aligned mesh and an arbitrary mesh. When the aligned mesh is used, the two workflows show agreement within 5%, and when the arbitrary mesh is used, the two workflows show agreement within 40%.

The workflow was also demonstrated with a full-production model of the SNS system. The SDR was tallied in three mesh tallies around the target assembly, and the results were compared to SDR results obtained with the cell-based workflow. Two of the three tallies were within 50% agreement between the two workflows, and the third tally significantly

underestimates the SDR results. Possible reasons for the significant difference are the choice of mesh and the definition of the geometry in each workflow.

Preliminary validation work was performed using the same full-production model of the SNS system. The SDR was tallied from 11 detectors, which were positioned around the drained target vessel of the SNS system. The SDR detector results were compared to experimental values. Seven out of eleven detectors had an agreement within a factor of 2, which constitutes a satisfactory agreement. The other six detectors had a significantly lower SDR result when compared to the experimental values. These comparisons to the experimental results demonstrated a good starting place for validation, but more numerical and experimental results are needed for a complete validation suite.

Chapter 4

Variance Reduction for Accelerator-Driven Systems

Estimating the SDR in accelerator-based systems often involves calculating the SDR in heavily shielded areas. This shielding can attenuate important particles, which leads to low variance, and therefore necessitates the development of VR methods. In an R2S calculation for these systems, VR is often required for both the neutron and photon transport steps. The photon transport can be optimized using the CADIS method, while the neutron transport is more complicated as the importance of neutrons to the final SDR is not easily defined. The MS-CADIS method was developed to optimize the neutron transport step in an R2S calculation in which we are seeking to optimize the SDR response at some location. The MS-CADIS, discussed in section 2.4.3, requires that a linearized activation operator, $T(\vec{r}, E_n, E_p)$ be defined in order to calculate the adjoint neutron source ($q^{\dagger}(\vec{r}, E_n)$). An implementation of MS-CADIS for use with SDR analysis of fusion systems provides a way to obtain a solution for $T(\vec{r}, E_n, E_p)$. This implementation, introduced as GT-CADIS in Section 2.4.4, has been validated for use with neutron energies typical of a fusion device.

For accelerator-based systems, where neutron energies can reach the GeV region, VR methods are limited. The CADIS and the FW-CADIS methods have been used to generate VR parameters for radiation transport calculations. These methods are often applied to optimize some response from a neutron transport calculation or a photon transport calculation, but generally cannot be applied to coupled transport calculations. The CADIS or FW-CADIS methods are often used to optimize some response from a neutron transport

calculation, and have traditionally been applied to only low-energy neutrons (less than 25 MeV). These methods require an adjoint transport calculation, which requires cross-section data tables. These cross-section data tables are not available for high-energy neutrons, and therefore, the adjoint transport cannot be performed for high-energy neutrons. More recently, a cross-section data library with neutron energies up to 2 GeV has been developed to be used in a deterministic calculation of accelerator-based systems. Recent efforts use these cross-section libraries to expand on the CADIS and FW-CADIS methods to be used with high-energy neutrons [25].

Currently, VR methods to optimize the primary step of an R2S calculation for accelerator-based systems are limited. This chapter aims to put forth an implementation of the MS-CADIS method for optimizing the neutron transport step of an SDR calculation for accelerator-based systems. This implementation is an expansion of the GT-CADIS initially developed for use with fusion systems. The methodology will be derived from first principles as the equations describing the transmutation problem differs from what was used for the original GT-CADIS.

4.1 MS-CADIS for Accelerator-Driven Systems

An implementation of the MS-CADIS method can be used to optimize the primary transport step in accelerator-based systems where neutron energies surpass the energy range for which nuclear cross-section tables exist. This MS-CADIS implementation is an extension of the GT- CADIS method discussed in section 2.4.4. The GT-CADIS method was developed for VR in SDR analysis of fusion systems and verified for such systems [5].

This work aims to develop a version of GT-CADIS that provides a way to resolve $T(\vec{r}, E_n, E_p)$ for accelerator-based applications. Determining $T(\vec{r}, E_n, E_p)$ for accelerator-based applications requires a different nuclide concentration equation, which accounts for nuclide production outside of the energy range of cross-section tables. If a solution of

$T(\vec{r}, E_n, E_p)$ can be found, then a solution for the adjoint neutron source can be found using Equation 2.39.

4.1.1 Photon Emission Density and Neutron Flux

In order to obtain the linearized activation operator, $T(\vec{r}, E_n, E_p)$, the relationship between the photon emission density and neutron flux must be approximated with a linear relationship as described in Equation 2.36. This equation is expressed again below with the position notation suppressed.

$$q_p(E_p) = \int_{E_n} T(E_n, E_p)\phi_n(E_n)dE_n \tag{4.1}$$

To define the photon emission density, consider an irradiation scenario where material is irradiated for time t_{irr} and allowed to decay for time t_{decay}. The photon emission density at the end of the irradiation scenario $t_{total} = t_{irr} + t_{decay}$ is given by the Equation 4.2.

$$q_p(E_p, t_{tot}) = \sum_c \lambda_{c,i_c} b_{c,i_c}(E_p) N_{c,i_c}(t_{tot}), \tag{4.2}$$

where λ_{c,i_c} is the decay constant and $b_{c,i_c}(E_p)$ is the branching ratio. The notation c represents a transmutation chain, and the i_c is the last nuclide in the chain. In Equation 4.2, the only flux-dependent term is the nuclide concentration, $N_{c,i_c}(t_{tot})$. The nuclide concentration must be explicitly expressed in terms of flux to cast Equation 4.2 into Equation 4.1.

The nuclide concentration can be expressed using the Bateman equation as given in Equation 4.3.

$$\begin{aligned} N_{c,i_c}(t) = &\sum_{j=1}^{i_c} \left(\prod_{k=j}^{i_c-1} P_{c,k+1} \right) \left[N_{c,j}(0) \left(\sum_{k=j}^{i_c} \frac{e^{-d_{c,k}t}}{\prod_{l=j,\neq k}^{i_c} (d_{c,l} - d_{c,k})} \right) + \right. \\ &\left. Y_{c,j} \left(\frac{1}{\prod_{l=j}^{i_c} d_{c,l}} - \sum_{k=j}^{i_c} \frac{e^{-d_{c,k}t}}{d_{c,k} \prod_{l=j,\neq k}^{i_c} (d_{c,l} - d_{c,k})} \right) \right] \end{aligned} \tag{4.3}$$

The P and d terms in this equation represent the production and destruction during a given time interval. Y_c is a constant term that describes the nuclide production and destruction during an irradiation interval for the energy domain outside the nuclear data libraries. For

our irradiation scenario of one irradiation time, t_{irr} followed by one decay time, t_{dec}, the nuclide concentration, $N_{c,i_c}(t_{tot})$, at the end of the scenario is defined as

$$N_{c,i_c}(tot) = \sum_{j=1}^{i_c} \left(\prod_{k=j}^{i_c-1} P_{c,k+1} \right) \left[N_{c,j}(t_{irr}) \left(\sum_{k=j}^{i_c} \frac{e^{-d_{c,k}t_{dec}}}{\prod_{l=j,\neq k}^{i_c}(d_{c,l} - d_{c,k})} \right) \right], \tag{4.4}$$

where the P and d terms represent the production and destruction during the decay period and are, therefore, not flux-dependent. The only flux-dependent terms in Equation 4.4 are the $N_{c,j}(t_{irr})$ terms, which can be defined as the production and destruction of nuclides during the irradiation time.

An $N(t_{irr})$ term must be defined that satisfies the linearity with respect to the neutron flux as given in the following equation:

$$N_{c,i}(E_n, t_{irr}) = \int_{E_n} U_{c,i}(E_n, t_{irr}) \phi_n(E_n) dE_n \tag{4.5}$$

If $U_{c,i}(E_n, t_{irr})$ can be defined that satisfies Equation 4.5, then $N_{c,i_c}(t_{tot})$ can be explicitly defined in terms of flux.

Section 4.2 describes the approximations needed to find a suitable $U_{c,i}(E_n, t_{irr})$. Let us assume that $U_{c,i}(E_n, t_{irr})$ exists to satisfy Equation 4.5 and that Equation 4.4 can be defined by Equation 4.6.

$$N_{c,i_c}(tot) = \sum_{j=1}^{i_c} \left[N_{c,j}(t_{irr}) A_{c,i_c,j}(t_{dec}) \right], \tag{4.6}$$

where $A_{c,i_c,j}(t_{dec})$ is given by:

$$A_{c,i_c,j}(t_{dec}) = \left(\prod_{k=j}^{i_c-1} P_{c,k+1} \right) \left(\sum_{k=j}^{i_c} \frac{e^{-d_{c,k}t_{dec}}}{\prod_{l=j,\neq k}^{i_c}(d_{c,l} - d_{c,k})} \right). \tag{4.7}$$

Substituting Equation 4.5 into Equation 4.6 leads to Equation 4.8.

$$N_{c,i_c}(t_{tot}) = \int_{E_n} \left[\sum_{j=1}^{i_c} U_{c,j}(E_n, t_{irr}) A_{c,i_c,j}(t_{dec}) \right] \phi_n(E_n) dE_n, \tag{4.8}$$

where $A_{c,i_c,j}(t_{dec})$ represents the production/destruction rate of nuclide i_c in chain c from nuclide j during the decay interval t_{dec}. Substituting Equation 4.8 into Equation 4.2 leads

to Equation 4.9. This equation shows the relationship between the photon emission density, $q_p(E_p, t_{tot})$, and neutron flux, $\phi_n(E_n)$.

$$q_p(E_p, t_{tot}) = \sum_c \lambda_{c,i_c} b_{c,i_c}(E_p) \left[\int_{E_n} \left[\sum_{j=1}^{i_c} U_{c,j}(E_n, t_{irr}) A_{c,i_c,j}(t_{dec}) \right] \phi_n(E_n) dE_n \right] \tag{4.9}$$

Equation 4.9 can be cast into the form of Equation 4.1. This leads to the following solution for $T(E_n, E_p)$:

$$T(E_n, E_p) = \sum_c \lambda_{c,i_c} b_{c,i_c}(E_p) \left[\sum_{j=1}^{i_c} U_{c,j}(E_n, t_{irr}) A_{c,i_c,j}(t_{dec}) \right] \tag{4.10}$$

If $U_{c,j}(E_n, t_{irr})$ can be found that satisfies Equation 4.5, then a solution for $T(E_n, E_p)$ can be found as given by Equation 4.10. Section 4.2 describes the circumstance in which a suitable $U_{c,j}(E_n, t_{irr})$ can be found.

4.2 Transmutation Approximations

In Section 4.1, it was shown that a solution for $T(E_n, E_p)$ could be found if the concentration of nuclides after irradiation can be described as given by Equation 4.5. The nuclide concentration at the end of the irradiation time t_{irr} can be defined with the Bateman equation given in Equation 4.3. This equation includes a term that represents the production and destruction of radionuclides from interactions in high-energy regions. Due to how a linear transmutation chain is modeled, a few simplifying assumptions can be made to the nuclide concentration equation. First, we assume that only the first nuclide of any given chain is present at the beginning of irradiation. This means that only $N_{c,1}$ is defined at the beginning of the irradiation period. The concentration of all other nuclides in the chain is zero. If other nuclides are present at the beginning of irradiation, they will be modeled by a separate transmutation chain. The second assumption is that the parent nuclide is stable. That is to say that $N_{c,1}$ does not contribute to the nuclide concentration of nuclide i during the decay period. With these assumptions, the nuclide concentration at the end of irradiation can be

defined by Equation 4.11.

$$N_{c,i_c}(t_{irr}) = \left(\prod_{k=1}^{i_c-1} P_{c,k+1}\right)\left[N_{c,1}(0)\left(\sum_{k=1}^{i_c}\frac{e^{-d_{c,k}t_{irr}}}{\prod_{l=1,\neq k}^{i_c}(d_{c,l}-d_{c,k})}\right)+ Y_{c,1}\left(\frac{1}{\prod_{l=1}^{i_c} d_{c,l}} - \sum_{k=1}^{i_c}\frac{e^{-d_{c,k}t_{irr}}}{d_{c,k}\prod_{l=1,\neq k}^{i_c}(d_{c,l}-d_{c,k})}\right)\right] \tag{4.11}$$

Equation 4.11 is comprised of two terms. The first term in the square brackets represents the contributions from the decay and nuclear reactions for low neutron energies during the irradiation time. The second term in the square brackets represents the contribution from high-energy nuclide productions and decay during irradiation time. In this equation, the P and d terms can be flux-dependent terms.

In order to cast Equation 4.11 into the form of Equation 4.5, all the flux-dependent terms must be in linear form. This means that the destruction terms appearing in exponentials must be linearized. We can linearize all the exponential terms in Equation 4.11 by using a Taylor expansion, which is given by Equation 4.12.

$$e^{-dt_{irr}} = \sum_{z=0}^{\infty}\frac{(-dt_{irr})^z}{z!} = \sum_{z=0}^{Z}\frac{(-dt_{irr})^z}{z!}, \tag{4.12}$$

where Z is a truncation variable that defines the number of terms needed to approximate the exponential adequately. When $dt_{irr} < 1$, then the magnitude of the Taylor expansion terms decreases monotonically, as seen in Equation 4.13. A smaller dt_{irr} value leads to a faster decrease of the terms, which means fewer terms are needed to represent the exponential properly.

$$|1| > \left|\frac{(-dt_{irr})^2}{2}\right| > \left|\frac{(-dt_{irr})^3}{6}\right| > ... \tag{4.13}$$

A small value of dt_{irr} occurs when the destruction rate is low and the irradiation time short, representing a low burnup. This means that the lower the burnup, the fewer terms are needed to represent the exponential term in the nuclide concentration equation.

If we apply the Taylor expansion on Equation 4.11, we obtain Equation 4.14.

$$N_{c,i_c}(t_{irr}) = \left(\prod_{k=1}^{i_c-1} P_{c,k+1}\right)\left[N_{c,1}(0)\left(\sum_{k=1}^{i_c} \frac{\sum_{z=0}^{Z} \frac{(-d_{c,k}t)^z}{z!}}{\prod_{l=1,\neq k}^{i_c}(d_{c,l}-d_{c,k})}\right)+ Y_{c,1}\left(\frac{1}{\prod_{l=1}^{i_c} d_{c,l}} - \sum_{k=1}^{i_c} \frac{\sum_{z=0}^{Z} \frac{(-d_{c,k}t)^z}{z!}}{d_{c,k}\prod_{l=1,\neq k}^{i_c}(d_{c,l}-d_{c,k})}\right)\right] \tag{4.14}$$

The Taylor expansion truncation criterion is that the Z term is much greater than the $Z+1$ term.

$$\left|\frac{(-d_k t_{irr})^Z}{Z!}\right| >> \left|\frac{(-d_k t_{irr})^{Z+1}}{(Z+1)!}\right| \tag{4.15}$$

The following three sections discuss cases to understand the extent to which this approximation is valid and allow us to cast Equation 4.11 into Equation 4.5.

4.2.1 Simple Case: i = 2

Imagine a linear transmutation chain where $N_1 \rightarrow N_2$. In this case, the nuclide concentration during irradiation for nuclide $i = 2$ is:

$$N_2(t_{irr}) = P_2\left[N_1(0)\frac{e^{-d_1 t_{irr}} - e^{-d_2 t_{irr}}}{(d_2-d_1)} + Y_1\left[\frac{1}{d_1 d_2} - \frac{1}{d_2-d_1}\left(\frac{e^{-d_1 t_{irr}}}{d_1} - \frac{e^{-d_2 t_{irr}}}{d_2}\right)\right]\right] \tag{4.16}$$

Applying the Taylor expansion to Equation 4.16 leads to

$$N_2(t_{irr}) = P_2\left[N_1(0)\frac{\sum_{z=0}^{Z} \frac{(-t_{irr})^z}{z!}(d_1^z - d_2^z)}{(d_2-d_1)} + Y_1\left[\frac{1}{d_1 d_2} - \frac{1}{d_2-d_1}\left(\frac{\sum_{z=0}^{Z} \frac{(-d_1 t_{irr})^z}{z!}}{d_1} - \frac{\sum_{z=0}^{Z} \frac{(-d_2 t_{irr})^z}{z!}}{d_2}\right)\right]\right] \tag{4.17}$$

If the truncation is allowed to be $Z = 2$, then Equation 4.17 becomes:

$$\begin{aligned} N_2(t_{irr}) &= N_1(0)P_2\left[t_{irr} - \frac{1}{2}(d_1+d_2)t_{irr}^2\right] + \frac{1}{2}Y_1 P_2 t_{irr}^2 \\ &= N_1(0)P_2 t_{irr} - \frac{1}{2}N_1(0)d_1 P_2 t_{irr}^2 - \frac{1}{2}N_1(0)d_2 P_2 t_{irr}^2 + \frac{1}{2}Y_1 P_2 t_{irr}^2 \end{aligned} \tag{4.18}$$

In Equation 4.18, the second and third terms have a production term multiplying a destruction term. The fourth term has the high-energy production term Y multiplying a production term. If the production term is flux-dependent, then so is the destruction term. This means that Equation 4.18 will have quadratic flux terms. It becomes clear then that this equation cannot be cast into the form of Equation 4.5.

If the truncation parameter is $Z = 1$, Equation 4.17 becomes

$$N_2(t_{irr}) = N_1(0)P_2t_{irr} \tag{4.19}$$

Notice that this equation does not include a contribution from the high-energy production term Y. Equation 4.19 has only one production term and could be cast into the form of Equation 2.36 if the production term has the following form:

$$P_2 = \int_{E_n} \sigma_{1\to2}(E_n)\phi_n(E_n)dE_n \tag{4.20}$$

Substituting Equation 4.20 into Equation 4.19 leads to

$$N_2(tirr) = N_1(0)t_{irr}\int_{E_n} \sigma_{1\to2}(E_n)\phi_n(E_n)dE_n \tag{4.21}$$

The contributions from the high-energy production term to the nuclide concentration are not accounted for in Equation 4.21. Contributions to the nuclide concentration from high-energy interactions are accounted for in a separate chain where $N_1(0) = 0$. Imagine a different chain where $N_1 \to N_2$, and this time N_1 is a nuclide not present as parent material, but as high-energy nuclide production. The nuclide concentration for N_2, when $N_1(0) = 0$ is given by:

$$N_2(t_{irr}) = P_2Y_1\Big[\frac{1}{d_1d_2} - \frac{1}{d_2 - d_1}\Big(\frac{e^{-d_1t_{irr}}}{d_1} - \frac{e^{-d_2t_{irr}}}{d_2}\Big)\Big] \tag{4.22}$$

In this equation, the Y term is a flux-dependent term as at least one neutron interaction occured to yield the high-energy production or destruction rate. In order for Equation 4.22 to have the format of Equation 4.5, the production and destruction terms must not be flux dependent. This means that the P and d terms must represent production and destruction rates from decay during irradiation time. This is true when the N_1 is not a stable nuclide, and it is allowed to decay.

4.2.2 General Case

The same procedure as the simple case can be applied to get the nuclide concentration for the i_{th} nuclide in a given transmutation chain. Starting with Equation 4.14 and applying truncation at $Z = i$ to obtain the following equation:

$$N_{c,i_c}(t_{irr}) = N_{c,1}(0)\frac{t_{irr}^{i_c-1}}{i_c!}\Big(i_c - t_{irr}\sum_{j=1}^{i_c} d_{c,j}\Big)\prod_{k=2}^{i_c} P_{c,k} + Y_{c,1}\frac{t_{irr}^{i_c}}{i_c!}\prod_{j=2}^{i_c} P_{c,j} \tag{4.23}$$

In Equation 4.23, the first term is comprised of a production term multiplied by a destruction term. Just like in the simple case, if these terms are flux-dependent, then they will have a quadratic flux. The second term includes the flux-dependent Y term multiplied by a production term, which might also be flux-dependent. This means that Equation 4.23 cannot be cast into the form of Equation 4.5.

If the truncation parameter is $Z = i - 1$, Equation 4.14 becomes

$$N_{c,i_c}(t_{irr}) = N_{c,1}(0)\frac{t_{irr}^{i_c-1}}{(i_c-1)!}\cdot\prod_{j=2}^{i_c} P_{c,j} \tag{4.24}$$

Notice that Equation 4.24 does not account for high-energy contributions. These are accounted for in a different chain and discussed in Section 4.2.3. Equation 4.24 only has production terms. In order for Equation 4.24 to take the form of Equation 4.5, only one production term can be flux-dependent. Because N_1 is assumed to be stable, P_2 must be flux-dependent for transmutation to occur. All the other production terms must have no flux dependency. This means that P_2 is defined by:

$$P_{c,2} = \int_{E_n} \sigma_{c,1\to 2}(E_n)\phi_n(E_n)dE_n \tag{4.25}$$

Substituting Equation 4.25 into Equation 4.24 yields:

$$N_{c,i_c}(t_{irr}, E_n) = N_{c,1}(0)\frac{t_{irr}^{i_c-1}}{(i_c-1)!}\prod_{j=3}^{i_c} P_{c,j}\int_{E_n} \sigma_{c,1\to 2}(E_n)\phi_n(E_n)dE_n \tag{4.26}$$

Equation 4.26 is in the form of Equation 4.5. Casting $N_i(t_{irr})$ into the form of Equation 4.5 led to a set of criteria that must be met to obtain the solution. This set of criteria is defined

as the SNILB criteria and is explicitly defined by Equations 4.27a - 4.27c.

$$\left|\frac{(-d_k t_{irr})^{i-1}}{(i-1)!}\right| >> \left|\frac{(-d_k t_{irr})^{i}}{i!}\right| \quad \text{for } i \,\epsilon\, [2, i_c],\ k \,\epsilon\, [1, i] \tag{4.27a}$$

$$P_2 = \int_{E_n} \sigma_{1\to 2}(E_n)\phi_n(E_n)dE_n \tag{4.27b}$$

$$P_j \neq P_j(\phi_n(E_n)) \text{ for } j \,\epsilon\, [3,\, i_c] \tag{4.27c}$$

Equation 4.27a represents the low burnup criteria. This criterion is met when t_{irr} is short, and/or the destruction rate is low. This criterion must be met for nuclides $i \,\epsilon\, [2, i_c]$. Equations 2.43b and 2.43c denote that nuclide i_c should be created by a transmutation pathway that contains a single neutron interaction, specifically the transmutation from nuclide 1 to nuclide 2.

Equation 4.26 leads to the following definition of $U_i(E_n, t_{irr})$:

$$U_{c,i_c}(E_n, t_{irr}) = N_{c,1}(0)\frac{t_{irr}^{i_c-1}}{(i_c-1)!}\prod_{j=3}^{i} P_{c,j}\sigma_{c,1\to 2}(E_n) \tag{4.28}$$

4.2.3 Case: $N_1(0) = 0$

Now consider a case in which the initial concentration of the first nuclide in the chain is zero, $N_{c,1} = 0$, and only Y_1 is present. The nuclide concentration equation becomes:

$$N_{c,i_c}(t_{irr}) = Y_{c,1}\left(\prod_{k=1}^{i_c-1} P_{c,k+1}\right)\left(\frac{1}{\prod_{l=1}^{i_c} d_{c,l}} - \sum_{k=1}^{i_c}\frac{e^{-d_{c,k}t_{irr}}}{d_{c,k}\prod_{l=1,\neq k}^{i_c}(d_{c,l}-d_{c,k})}\right) \tag{4.29}$$

The Y term is the production and destruction rates due to transmutations during irradiation. This term is a flux-dependent term. The P and d terms in Equation 4.29 must not be flux-dependent for this equation to be cast into the form of 4.5. Therefore, the P and d must only be production and destruction from decay during the irradiation time. For P and d to be able to decay, Y_1 is not a stable nuclide, and it is allowed to decay.

A collision estimate tally collects information on the production and destruction of nuclides from high-energy interactions. The constant production rate term, Y_i, is obtained

from nuclear physics models present in radiation transport software. The Y_i tally can be defined by the following equation:

$$Y_i = \frac{1}{W} \sum_{x \in A} \frac{w_x \Sigma_i(E_n)}{\Sigma_t(E_n)}, \tag{4.30}$$

Equation 4.30 is a rate equation and can be represented as

$$Y_i = \int_{E_n} \sum_j N_j \sigma_j \phi_n(E_n) dE_n \tag{4.31}$$

The flux is given by:

$$\phi_n(E_n) = \frac{1}{W} \sum_{x \in A} \frac{w_x}{\Sigma_t(E_n)} \tag{4.32}$$

In this case, $N_{c,i}(E_n, t_{irr})$ does not have the exact form of Equation 4.5. Instead, it has the following form:

$$N_{c,i}(E_n, t_{irr}) = \int_{E_n} V_{c,i}(E_n, t_{irr}) Y(E_n) dE_n \tag{4.33}$$

Equation 4.33 is dependent on Y, which is a constant term that includes the neutron flux term. The $Y_i(E_n)$ can be defined in terms of flux as given in the following equation:

$$Y_i = \int_{E_n} \left[\sum_{j=1}^{i-1} N_j(0) \sigma_{j \to i}(E_n) \phi_n(E_n) - \sum_{j=1}^{i-1} N_i(0) \sigma_{i \to j}(E_n) \phi_n(E_n) \right] dE_n \tag{4.34}$$

Substituting Equation 4.34 into Equation 4.29 and rearranging the equation, we get

$$\begin{aligned} N_{c,i_c}(t_{irr}) = \int_{E_n} & \left[\sum_{j=1}^{i-1} N_j(0) \sigma_{j \to i}(E_n) - \sum_{j=1}^{i-1} N_i(0) \sigma_{i \to j}(E_n) \right] \left(\prod_{k=1}^{i_c - 1} P_{c,k+1} \right) \\ & \left[\frac{1}{\prod_{l=1}^{i_c} d_{c,l}} - \sum_{k=1}^{i_c} \frac{e^{-d_{c,k} t_{irr}}}{d_{c,k} \prod_{l=1, \neq k}^{i_c} (d_{c,l} - d_{c,k})} \right] \phi_n(E_n) dE_n \end{aligned} \tag{4.35}$$

This equation has the form of 4.5, and therefore, $U_{c,j}(E_n, t_{irr})$ is defined by:

$$\begin{aligned} U_{c,j_c}(E_n, t_{irr}) = & \left[\sum_{j=1}^{i-1} N_j(0) \sigma_{j \to i}(E_n) - \sum_{j=1}^{i-1} N_i(0) \sigma_{i \to j}(E_n) \right] \left(\prod_{k=1}^{i_c - 1} P_{c,k+1} \right) \\ & \left[\frac{1}{\prod_{l=1}^{i_c} d_{c,l}} - \sum_{k=1}^{i_c} \frac{e^{-d_{c,k} t_{irr}}}{d_{c,k} \prod_{l=1, \neq k}^{i_c} (d_{c,l} - d_{c,k})} \right] \end{aligned} \tag{4.36}$$

4.3 Calculating $T(E_n, E_p)$

Section 4.1 stated that if $U_{c,i}(E_n, t_{irr})$ can be found that satisfies Equation 4.5, then a solution for $T(E_n, E_p)$ can be found using Equation 4.10. In Section 4.2, two solutions for $U_{c,i}(E_n, t_{irr})$ were found that satisfy Equation 4.5 in different cases. In the case where $N_1(0)$ is non zero, $U_{c,i}(E_n, t_{irr})$ is given by Equation 4.28. Substituting Equation 4.28 into Equation 4.10 and assuming that N_1 is stable, $T(E_n, E_p)$ is defined by:

$$T(E_n, E_p) = \sum_c \lambda_{c,i_c} b_{c,i_c}(E_p) \left[\sum_{j=2}^{i_c} N_{c,1}(0) \frac{t_{irr}^{j-1}}{(j-1)!} \prod_{k=3}^{i} P_{c,k} \sigma_{c,1\to 2}(E_n) A_{c,i_c,j}(t_{dec}) \right] \tag{4.37}$$

In the case where $N_1(0) = 0$, The nuclide concentration is dependent on the constant production rate, which accounts for production and destruction at high-energy interactions. $U_{c,i}(E_n, t_{irr})$ is given by Equation 4.36. Substituting Equation 4.36 into Equation 4.10, $T(E_n, E_p)$ is defined by:

$$\begin{aligned} T(E_n, E_p) = \sum_c \lambda_{c,i_c} b_{c,i_c}(E_p) & \left[\sum_{j=1}^{i-1} N_j(0) \sigma_{j\to i}(E_n) - \sum_{j=1}^{i-1} N_i(0) \sigma_{i\to j}(E_n) \right] \\ & \sum_{j=1}^{i_c} A_{c,i_c,j}(t_{dec}) \left(\prod_{k=1}^{i_c - 1} P_{c,k+1} \right) \left[\frac{1}{\prod_{l=1}^{i_c} d_{c,l}} - \sum_{k=1}^{i_c} \frac{e^{-d_{c,k} t_{irr}}}{d_{c,k} \prod_{l=1, \neq k}^{i_c} (d_{c,l} - d_{c,k})} \right] \end{aligned} \tag{4.38}$$

The $T(E_n, E_p)$ provided by Equations 4.37 and 4.38 can be substituted into Equation 2.39 to obtain the SNILB solution of the adjoint neutron source required for the MS-CADIS method.

4.4 High-Energy GT-CADIS

As discussed in Section 2.4.3, to apply the CADIS method to the primary step of a high-energy R2S calculation, it is necessary to obtain the quantity $T(E_n, E_p)$, which can then be used to obtain the MS-CADIS adjoint neutron source. Section 4.1 showed an analytical solution for $T(E_n, E_p)$ exists if a quantity $U(E_n, t_{irr})$ can be defined that satisfies Equation 4.5. The high-energy GT-CADIS method poses a procedure to obtain $T(E_n, E_p)$ that can

be applied regardless of the SNILB criteria being met. The adjoint neutron source is given by Equation 2.39 must be cast into a discrete form for this method. Discretizing the adjoint neutron source equation for neutron energy group g, photon energy group h, within volume v, yields the following equation:

$$q^{\dagger}_{v,n}(E_g) = \sum_h T_v(E_g, E_h)\phi^{\dagger}_{v,p}(E_h) \tag{4.39}$$

The discrete adjoint neutron source carries out the deterministic transport to obtain the adjoint neutron source. Equation 4.39 requires that $T_v(E_g, E_h)$ be defined. For this, Equation 4.1 should be discretized.

$$q_{v,p}(E_h) = \sum_g T_v(E_g, E_h)\phi_{v,n}(E_g) \tag{4.40}$$

From Equation 4.40, $T_v(E_g, E_h)$ can be calculated for each neutron and photon energy group.

$$T_v(E_g, E_h) = \frac{q_{v,p}(E_h, \phi_{v,n}(E_g))}{\phi_{v,n}(E_g)} \tag{4.41}$$

$T_v(E_g, E_h)$ can be calculated by performing an irradiation calculation for each neutron energy group g and each photon energy group h. The photon emission density in photon energy group h is recorded from irradiation of mesh volume element v with a single neutron energy group g.

For low neutron energies, less than 25 MeV, the photon emission density is calculated from neutron flux information, but for high neutron energies, higher than 25 MeV, the photon emission density is calculated from the high-energy production rate information. The high-energy production rate constant Y is used for the energy region above 25 MeV because activation cross-section libraries are not readily available for these energies. Because the photon emission density is calculated using different variables depending on the neutron energy group, two separate $T_v(E_g, E_h)$ can be defined. For low energy neutron groups, $T_v(E_g, E_h)$ is defined by Equation 4.42, and for high energy neutron groups, $T_v(E_g, E_h)$ is defined by Equation 4.43.

$$T_v(E_g, E_h) = \frac{q_{v,p}(E_h, \phi_{v,n}(E_g))}{\phi_{v,n}(E_g)} \quad \text{for } g \leq 25 \text{ MeV} \tag{4.42}$$

$$T_v(E_g, E_h) = \frac{q_{v,p}(E_h, Y_{v,n}(E_g))}{\phi_{v,n}(E_g)} \quad \text{for } g > 25 \text{ MeV} \tag{4.43}$$

Equations 4.42 and 4.43 are the linearized activation operators that linearly relate the photon emission density and neutron flux. Although this linear solution is an approximation to the true physics of a problem, these equations can be used whether or not the SNILB criteria are met. This is because the linearized activation operator is used in the GT-CADIS method to generate VR parameters and does not change the actual solution of the problem.

4.5 SNILB Criteria

The high-energy GT-CADIS method provides a way to obtain a solution for the linearized activation operator, $T_v(E_g, E_h)$, by approximating the true physics of the problem with a linear model. This linear relationship is contingent on the SNILB criteria being met. When the SNILB criteria are met, the solution for the linearized activation operator is equivalent to the SNILB solution. When the SNILB criteria are not met, the solution is simply an approximation to the SNILB analytical solution. If the SNILB criteria are not fully met, the approximation for the linearized activation operator can still be used since this quantity is used for the generation of VR parameters, and minor deviation might still result in useful VR. The extent to which the high-energy GT-CADIS method is effective as a VR method depends on the extent to which the SNILB criteria are met. The efficacy of the VR method is not necessarily known, as the accuracy of the approximation is not known. To assess the efficacy of the GT-CADIS method, a measurement of how well the SNILB criteria are met is needed.

When the SNILB criteria are met, the photon emission density resulting from irradiation with neutron flux from all neutron energy groups, $q_{v,p}(E_h, \phi_{v,n}, Y_{v,n})$, equals the sum of the photon emission densities resulting from irradiation with G single neutron energy groups, $q_{v,p}(E_h, \phi_{v,n}(E_g))$. Equation 4.44 represents the above for G number of neutron energy groups

where the last group $g = G$ is the high-energy group outside domain of cross-section tables.

$$q_{v,p}(E_h, \phi_{v,n}, Y_{v,n}) = \sum_{g}^{G-1} q_{v,p}(E_h, \phi_{v,n}(E_g)) + q_{v,p}(E_h, Y_{v,n}(E_G)), \tag{4.44}$$

This relationship is valid when the SNILB criteria are met and not valid when the SNILB criteria are violated. Equation 4.44 can be rearranged into a ratio to define an approximation factor. η, to quantify the extent to which the SNILB criteria are met.

$$\eta_h = \frac{\sum_{g}^{G-1} q_{v,p}(E_h, \phi_{v,n}(E_g)) + q_{v,p}(E_h, Y_{v,n}(E_G))}{q_{v,p}(E_h)(\phi_{v,n}, Y_{v,n})} \tag{4.45}$$

When $\eta_h = 1$, the SNILB criteria are met, and the solution for $T_v(E_g, E_h)$ is equivalent to the analytical SNILB solution. When $\eta_h \neq 1$, the SNILB criteria are violated, and the solution for $T_v(E_g, E_h)$ is just a possible approximation. If $\eta_h > 1$, the contributions of photon emission densities are overestimated, and if $\eta_h < 1$, the contributions are underestimated. This η_h quantity helps define the extent to which the SNILB criteria are met and quantifies of the effectiveness of the high-energy GT-CADIS method.

Chapter 5

Software Implementation

The numerical experiments in this work have required the development and use of several computational tools. A mesh R2S workflow was developed to calculate the SDR in accelerator-driven systems. This workflow takes mesh output from the neutron transport to write input files for an activation calculation with CINDER90 [13]. It then takes the photon emission density output to write a mesh photon source. This mesh photon source is then used in an MCNP photon transport to calculate the SDR at some detector or tally mesh. This R2S workflow implementation and validation is discussed in Chapter 3.

To calculate the VR parameters to optimize the primary transport of an R2S calculation for accelerator-driven systems, the high-energy GT-CADIS, discussed in Chapter 4 was implemented. The high-energy GT-CADIS workflow follows these general steps:

1. Perform deterministic adjoint photon transport to obtain the adjoint photon flux ($\phi_p^\dagger$).

2. Calculate $T(E_n, E_p)$, using Equations 4.42 and 4.43, for each neutron energy group g and photon energy group h via activation calculations.

3. Calculate the adjoint neutron source ($q_n^\dagger$) using Equation 4.39, the linearized activation operator $T(E_n, E_p)$ and the adjoint photon flux ($\phi_p^\dagger$).

4. Perform deterministic adjoint neutron transport to obtain the adjoint neutron flux ($\phi_n^\dagger$).

5. Use the adjoint neutron flux ($\phi_n^\dagger$) with CADIS to generate weight windows and source biasing parameters.

5.1 Deterministic Transport

The deterministic neutron and photon transports are performed using DENOVO integrated into ADVANTG [26]. An input file is generated for ADVANTG 3.2 to calculate the adjoint photon flux. This input file takes in an MCNP input file name, a tally number of the detector of interest, a mesh definition in which to discretize the geometry and a nuclear cross-section library. The adjoint photon source is defined using the tally of interest.

An ADVANTG 3.2 input file is also generated for a preliminary deterministic adjoint neutron transport run. The input parameters are similar to those used in the deterministic adjoint photon input file. An MCNP neutron input file name, an arbitrary tally number, a neutron cross-section library, HILO2K library [27], and the same mesh definition as in the adjoint photon transport were provided. The preliminary run uses an arbitrary adjoint neutron source created from an MCNP mesh or volume tally. The purpose of the run is to obtain a Denovo input file with necessary discretized information. This Denovo input file is modified with a Python script to replace the arbitrary neutron adjoint source for the adjoint neutron source generated with the linearized activation operator and adjoint photon fluxes.

The DENOVO deterministic transport is run again with the new adjoint neutron source to obtain the adjoint neutron flux that can later be used to generate VR parameters.

5.2 Generation of $T(E_n, E_p)$ for high-energy GT-CADIS

In order to calculate $T(E_n, E_p)$, the photon emission density is calculated using CINDER90. A Python script, *T_activation.py*, along with PyNE, and a Perl script are used to generate CINDER90 input files and perform an activation calculation. CINDER90 uses a 64-neutron energy group structure and a 25-photon energy group structure. Another Python script, *calc_T.py*, is used to generate $T(E_n, E_p)$ using a provided neutron flux and the photon

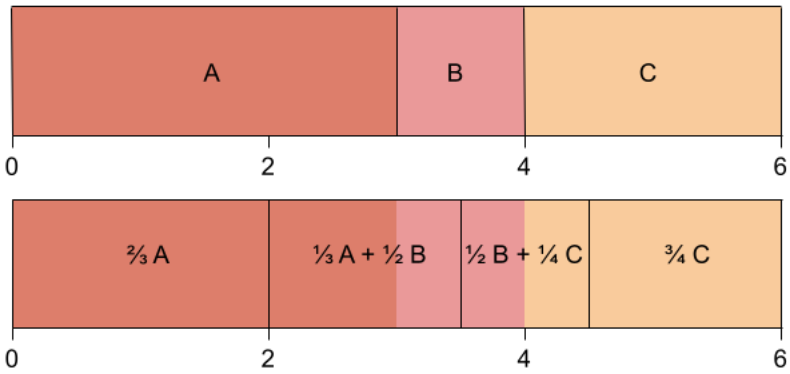

Figure 5.1: Overview of recast of energy group structures

emission density calculated with CINDER90. $T(E_n, E_p)$ is written out in a MOAB formatted mesh file with the neutron and photon energy groups of CINDER90.

5.3 Adjoint Neutron Source

A Python script, *adj_src_calc.py*, was written to use the DENOVO neutron input file, the adjoint photon flux, and $T(E_n, E_p)$ to calculate the adjoint neutron source. This script recasts $T(E_n, E_p)$ from a CINDER90 neutron and photon energy groups to ADVANTG 47 photon energy groups and HILO2K 83 neutron energy groups. The recast from energy group structure X to energy group structure Z is done by weighing sections of each energy group in group structure X to fit sections in group structure Z as shown in Figure 5.1.

Once $T(E_n, E_p)$ is calculated and restructured into the ADVANTG neutron and photon group structures, the script calculates the adjoint neutron source using Equation 4.39. This adjoint neutron source is then used in a deterministic calculation to obtain adjoint neutron fluxes for all neutron energies.

5.4 Generating Weight Windows and Source Biasing Parameters

The generation of weight windows and source biasing parameters is performed using the capabilities of ADVANTG 3.2. ADVANTG 3.2 calculates the weight window lower bounds using Equation 2.29 and the source biasing parameters using Equation 2.28. Both of these equations require an approximation of the response (R). ADVANTG uses Equation 2.25 to approximate a response with the unbiased source and the adjoint flux [26].

ADVANTG 3.2 generates a WWINP file that contains the weight window lower bounds with a response of one. It also outputs anMCNP weight window card, which has several input parameters, including a multiplication factor defined as the total response. The source biasing parameters are output to a source card. The VR parameters generated in this workflow can be used in an MCNP transport run.

5.5 SNILB

In order to quantify the efficacy of the high-energy GT-CADIS VR parameters, the approximation factor,η, must be calculated. A Python script, *eta_activation.py*, was written to read the neutron flux and radionuclide production information and run activation with CINDER90 to obtain the total photon emission and the photon emission per neutron energy group. This script then uses the photon emission density to calculate the approximation factor per material.

Chapter 6

SNILB Criteria Validation for Accelerator-Driven Systems

As shown in chapter 4, the efficacy of the high-energy GT-CADIS is dependent on finding a solution for $T(E_n, E_p)$ that satisfies a linear relationship between the photon emission density and the neutron flux. In order to find this linear relationship, approximations are necessary, leading to the SNILB criteria. This chapter explores the extent to which the SNILB criteria are met for accelerator-driven systems. A simple test problem is designed to have materials and conditions similar to those of an accelerator-driven system. η is calculated for each volume in this problem and for a variety of irradiation decay schedules.

6.1 Evaluation of the SNILB Criteria

The extent to which the GT-CADIS implementation is effective as a VR method depends on the extent to which the SNILB criteria are met. When the SNILB criteria are met, the solution for $T(E_n, E_p)$ is equivalent to the SNILB analytical solution; otherwise, the solution is a possible approximation.

A measurement of how well the SNILB criteria are met is needed to assess the efficacy of the GT-CADIS implementation. When the SNILB criteria are met, the photon emission density resulting from irradiation with neutron flux from all neutron energy groups, $q_{v,p,h}(\phi_{v,n}, Y_{v,n})$, equals the sum of the photon emission densities resulting from irradiation with a single neutron energy group, $q_{v,p,h}(\phi_{v,n,g})$. This is discussed in Chapter 4 and shown in Equation 4.44.

Equation 4.45 is used to calculate η. η allows for quantification of how well the SNILB criteria are met for accelerator-driven systems. η_h can be calculated per each material and photon energy group present in a problem. This chapter will calculate η_h per material in each volume and photon energy group. The final η value presented in plots will be a photon energy group collapsed value.

6.2 Problem Setup

A test problem has been generated using materials and conditions seen in accelerator-driven nuclear systems. Figure 6.1a shows an overall view of the geometry setup. The geometry consists of concentric cylinders divided into four regions along the longitudinal axis: Front, Middle Front, Middle Back, and Back. A 1 GeV monodirectional disk proton source was placed on the left side of the geometry. The concentric cylinders have been further divided to test different material combinations. Figure 6.1b shows a cross-sectional view of the materials used in the problem.

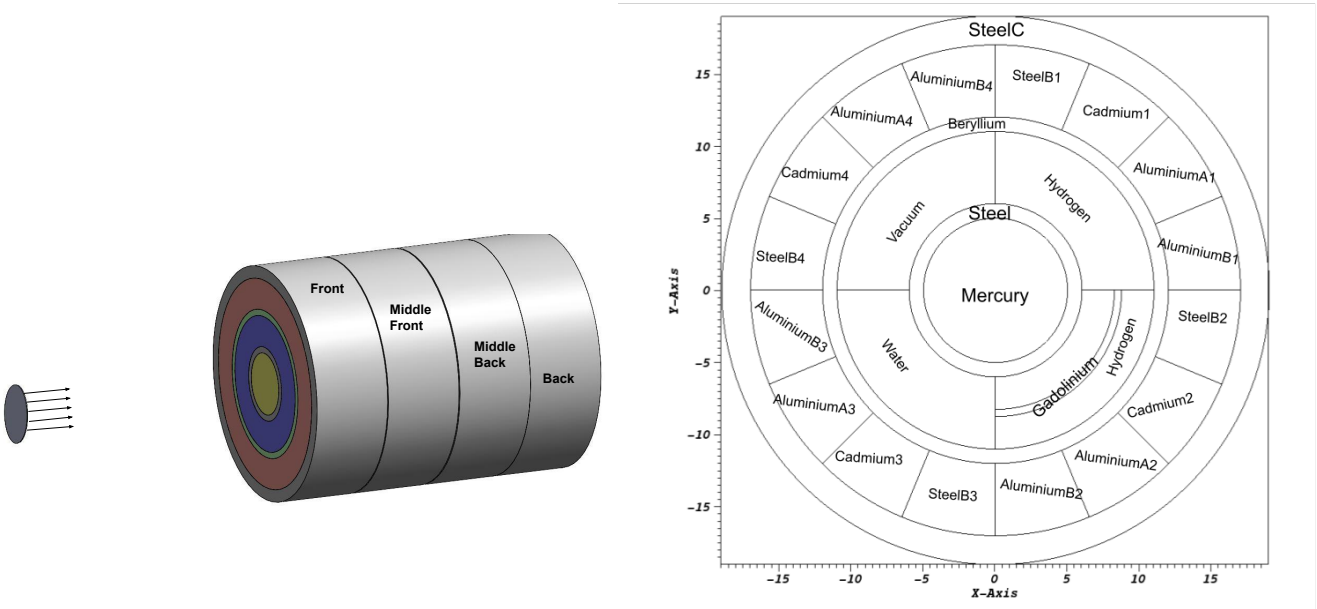

(a) Side view of geometry *(b) XY cutout view of geometry*

Figure 6.1: Overview of test problem

The material setup was chosen so that the third inner cylinder is divided into four quadrants, each with a different material or material combination. The sixth cylinder is divided into 16 parts, and the same four materials are repeated for each of the four quadrants. The materials used in this problem are described in Tables 6.1, 6.2, and 6.3.

Table 6.1: Steel material definitions in weight percent

ZAID (ZZZAAA)	**Steel A (weight percent)**	**Steel B (weight percent)**	**Steel C (weight percent)**
6000	0.0790	0.0140	0.0300
7014	0.0000	0.0000	0.1600
14028	0.9108	0.4310	0.0000
14029	0.0464	0.0222	0.0000
14030	0.0306	0.0145	0.0000
15031	0.0445	0.0215	0.0000
16032	0.0296	0.0140	0.0000
24050	0.7300	7.7162	0.7787
24052	14.0711	14.8808	14.9982
24053	1.5954	1.6872	1.7005
24054	0.3981	0.4206	0.4233
25055	1.9757	0.9347	0.0000
26054	3.7381	3.7408	3.9735
26056	59.1165	59.1550	62.8365
26057	1.4176	1.4189	1.5072
26058	0.1798	0.1804	0.1918
27059	0.0988	0.0000	0.0000
28058	8.0698	6.3636	7.3525
28060	3.1078	2.4518	2.8328
28061	1.3514	0.1066	0.1231
28062	0.4307	0.3393	0.3920
28064	0.1097	0.0869	0.1000
42092	0.3665	0.0000	0.3858
42094	0.2282	0.0000	0.2405
42095	0.3932	0.0000	0.4139
42096	0.4119	0.0000	0.4337
42097	0.2351	0.0000	0.2483
42098	0.5957	0.0000	0.6274
42100	0.2381	0.0000	0.2504

Table 6.2: Material definitions in atomic percent

ZAID (ZZZAAA)	**mercury (atomic %)**	**ZAID (ZZZAAA)**	**gadolinium (atomic %)**	**ZAID (ZZZAAA)**	**water (atomic %)**
80196	0.15	64152	0.20	1001	66.66
80198	9.97	64154	2.18	1002	0.01
80199	16.87	64155	14.80	8016	33.33
80200	23.10	64156	20.47		
80201	13.18	64157	15.65		
80202	29.86	64158	24.84		
80204	6.87	64160	21.86		
ZAID (ZZZAAA)	**cadmium (atomic %)**	**ZAID (ZZZAAA)**	**hydrogen (atomic %)**		
48000	100	1004	100		

Table 6.3: Aluminum and Beryllium material definitions in atomic percent

ZAID (ZZZAAA)	**aluminum B (atomic %)**	**aluminum A (atomic %)**	**ZAID (ZZZAAA)**	**beryllium (atomic %)**
12024	0.7899	0.8784	4009	99.4275
12025	0.1000	0.1112	6000	0.1132
12026	0.1101	0.1224	8016	0.3551
13027	97.1501	98.0875	8017	0.0001
14028	0.5533	0.5325	12024	0.0238
14029	0.0280	0.0270	12025	0.0030
14030	0.0186	0.0179	12026	0.0033
22046	0.0080	0.0000	13027	0.0336
22047	0.0073	0.0000	14028	0.0179
22048	0.0738	0.0000	14029	0.0009
22049	0.0055	0.0000	14030	0.0006
22050	0.0054	0.0000	26054	0.0012
24050	0.0087	0.0045	26056	0.0194
24052	0.1676	0.0871	26057	0.0004
24053	0.0190	0.0099	26058	0.0001
24054	0.0047	0.0025		
25055	0.1000	0.0000		
26054	0.0290	0.0000		
26056	0.4586	0.0824		
26057	0.0110	0.0367		
26058	0.0014	0.0000		
29063	0.2075	0.0000		
29065	0.0925	0.0000		
30000	0.0500	0.0000		

6.3 Calculations Set Up

The quantity η was calculated for all volumes in Figure 6.1b, which consists of 11 different materials. A neutron transport run was set up to obtain the neutron flux for all energy regions and the radionuclides production and destruction rates for the high-energy region.

The irradiation schedule consisted of one irradiation step and one decay step. A range of 20 irradiation and 20 decay intervals logarithmically spaced between 10^0 s and 10^8 s ($\sim$ 3 yrs) were used for the activation calculations. η_h was calculated using Equation 4.45 for each combination of irradiation decay times. Furthermore, to consolidate results, η_h was collapsed over all photon energies groups h as shown in Equation 6.1.

$$\eta = \sum_h \eta_h \tag{6.1}$$

6.4 Results and Discussion

6.4.1 Mercury and Steel

Figures 6.2 and 6.3 show the neutron flux for mercury and steel, respectively, for all energies binned into 64 groups. Both figures show the neutron flux for each of the four regions. These plots show that the neutron flux experienced by front volumes is the greatest and decreases as we move to the back of the geometry. This is the expected behavior as the proton source is at the front of the geometry.

Figures 6.4 and 6.5 show the net isotope production for all mercury and steel volumes. These plots show a similar trend as the mercury and steel fluxes; the isotope production decreases as we move away from the source towards the back of the geometry. The isotope production was used alongside the neutron flux up to 25 MeV for an activation calculation with a given irradiation scenario. The photon emission density obtained from the activation calculation was then used to calculate η_h.

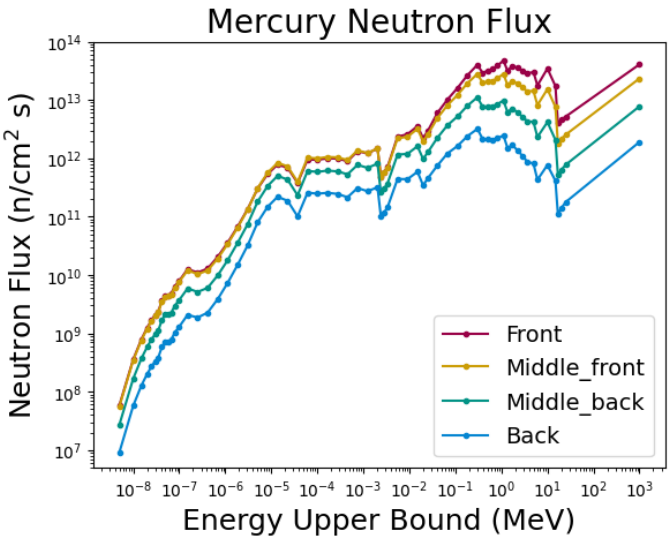

Figure 6.2: Neutron flux for mercury volumes

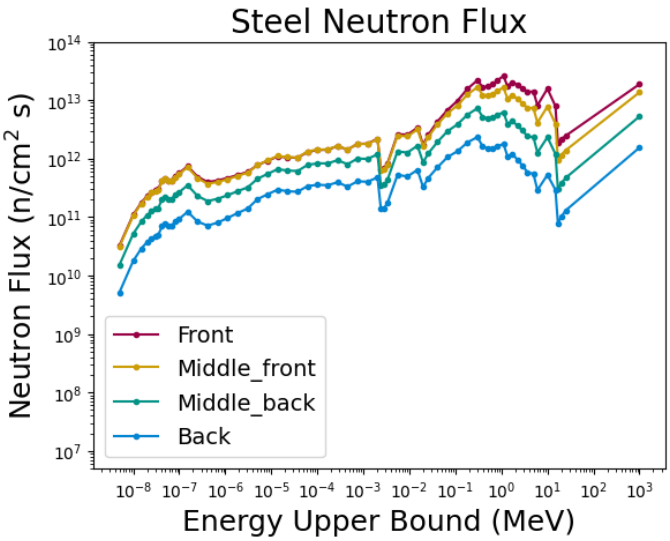

Figure 6.3: Neutron flux for steel volumes

Figure 6.6 shows the total photon energy η values for the mercury and steel volumes in each of the four regions for each of the 400 irradiation/decay scenarios. Overall, most of the η values calculated are close to one with some deviation at high and low irradiation times.

For the mercury volumes sweep, the three front volumes, which are closer to the neutron source, experience $\eta \approx 1$ for irradiation times up to 10^7 s. At higher irradiation times, there is some underestimation of the photon emission density depicted by the light red region. This is consistent with the expectation that the neutron fluence is higher at high irradiation

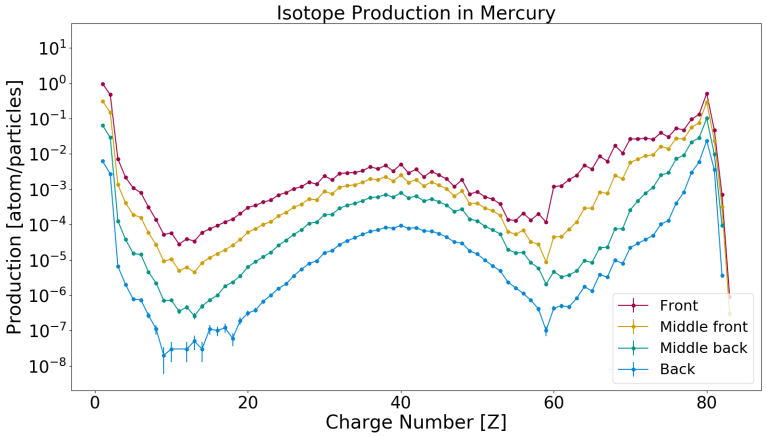

Figure 6.4: Net isotope production for mercury volumes

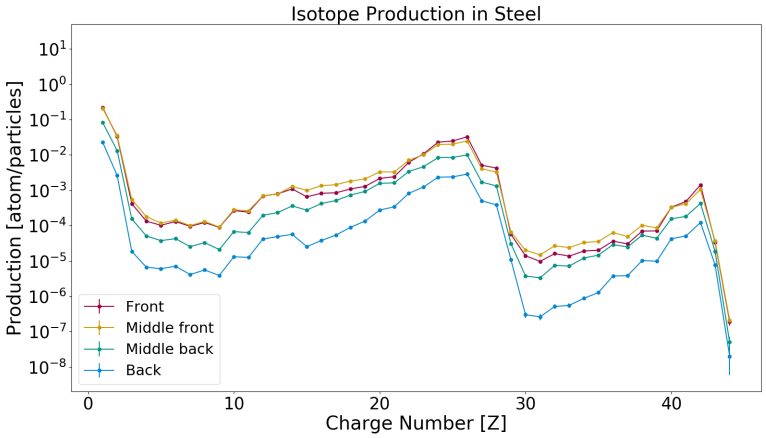

Figure 6.5: Net isotope production for steel volumes

times. Therefore, the material burn-up is higher, and the pathways that involve multiple interactions are more important.

For the three mercury volumes closest to the source, the minimum η is $\eta = 0.96$, and the maximum η is $\eta = 1.01$. This means that the photon emission density is underestimated by at most 4% and overestimated by at most 1%. The mercury volume at the back of the geometry shows high values of η at low irradiation times and high decay times. For this plot, the maximum overestimation is $\eta = 2.7$, which means that for these irradiation/decay scenarios, the photon emission density is overestimated to be over two times higher than the actual photon emission density. This means that the SNILB criteria are violated for that

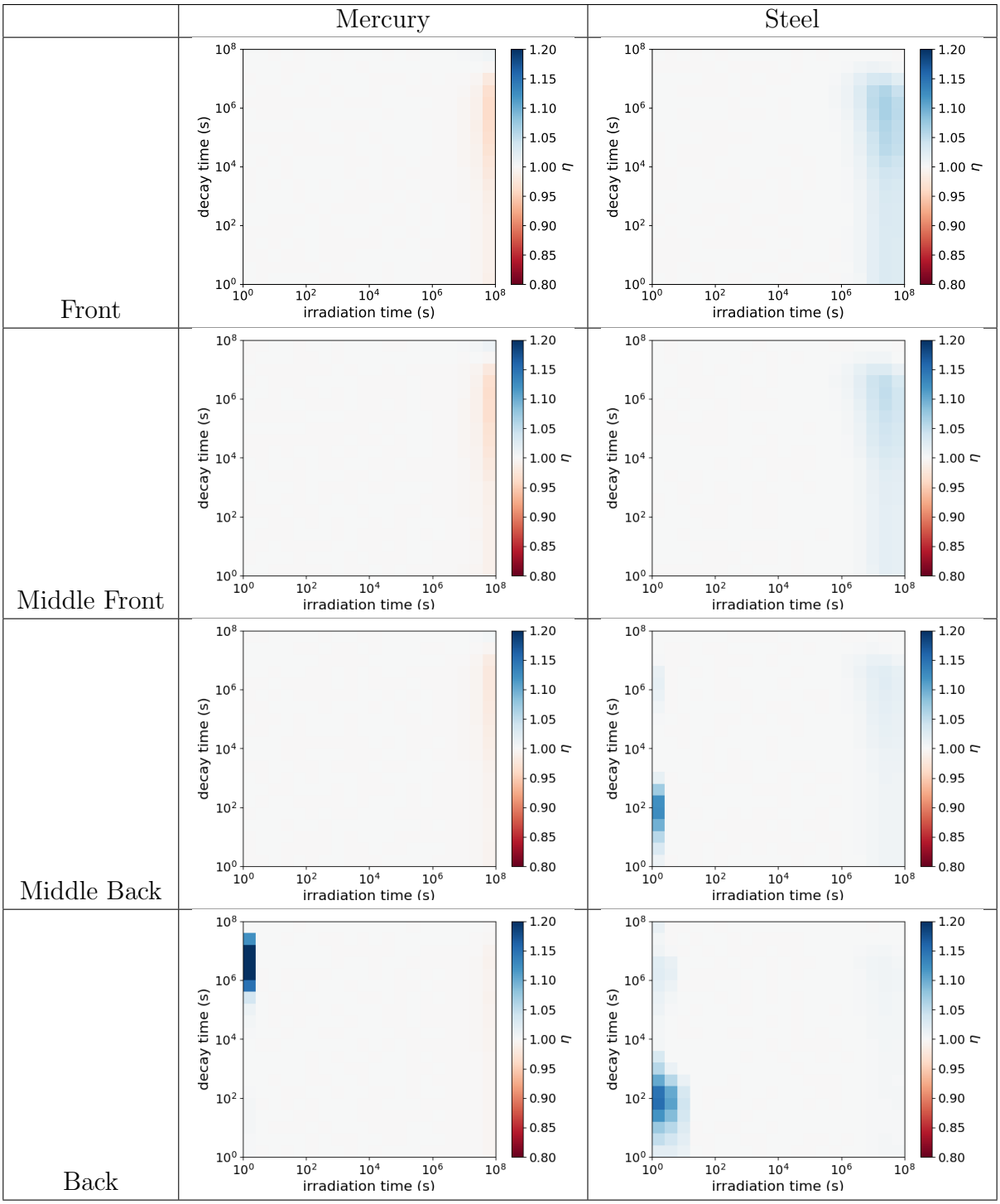

Figure 6.6: η sweep for all mercury and steel volumes

specific scenario and that the GT-CADIS method will overestimate the importance of the material to the SDR response. It is also important to note that these low irradiation times

are highly unlikely to be used in a real irradiation scenario. This gives confidence that the SNILB criteria are met or only slightly violated for likely scenarios.

For the steel volumes, the η sweep shows values of η close to one with some $\eta > 1$ at high and low irradiation times. The maximum overestimation is $\eta = 1.15$. This indicates that the importance of the material to the final response will be overestimated by 15%.

These η values give insight into how much these materials comply with the SNILB criteria or how much they violate it under the specific irradiation/decay scenario. This, in turn, informs the efficacy of the GT-CADIS method, which generates VR parameters for optimizing the neutron transport of an R2S calculation. Large overestimations of the photon emission density, like those happening in the mercury volume at the back of the geometry, can be further investigated to discern which nuclides contribute to the overestimation. On the other hand, because VR parameters can vary by several orders of magnitude, an overestimation or underestimation of 15% is not likely to significantly change the efficacy of the VR parameters.

6.4.2 Other Materials

The η evaluation for all the other materials can be seen in Figures 6.7 and 6.8. Figure 6.7 shows the η sweep results for beryllium in the fourth ring and the outer layer of steel from figure 6.1b. Only the front volumes are shown in this figure. For both of these materials, there is some overestimation of low irradiation times with a maximum η being $\eta = 1.22$. This means that the importance of these materials to the response of interest will be overestimated by, at most, 22% at low irradiation times.

Figure 6.8 shows the η values for the front volumes of the moderators located in the third ring in Figure 6.1b and the materials on the sixth ring in the same figure. This configuration of materials was set up to analyze how the η values of the same material would be affected by differences in flux due to neutrons passing through different materials (i.e., different moderators). In this figure, the moderators experience $\eta < 1$ at high irradiation

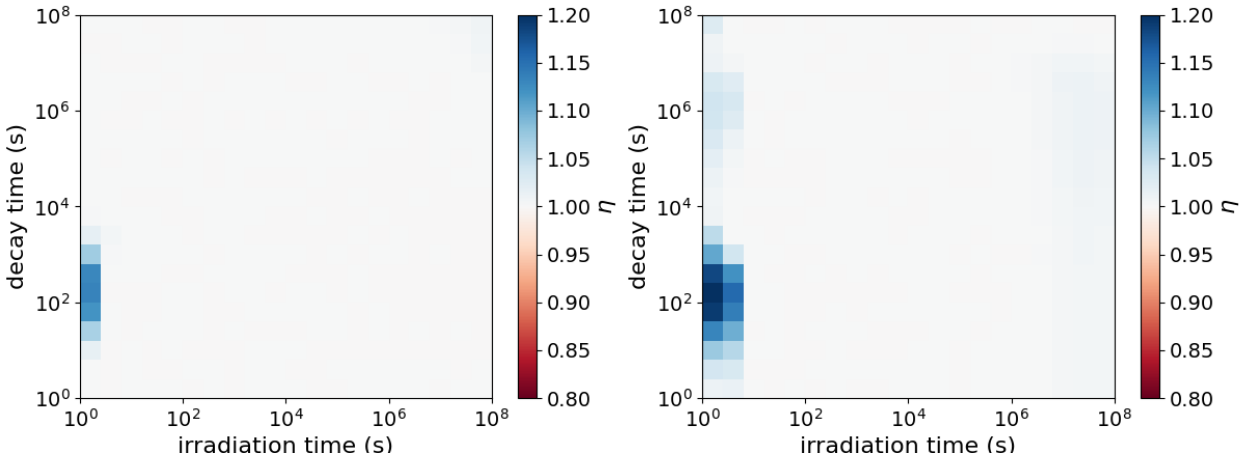

(a) Beryllium (min/max: 0.99, 1.13) *(b) SteelC (min/max: 0.99, 1.22)*

Figure 6.7: η sweep for Beryllium and SteelC front volumes

times as the flux is greater at those times. For hydrogen and hydrogen with gadolinium, the underestimation is at most $\eta = 0.84$, which means that photon emission density is underestimated by at most 20%. Water experiences $\eta < 1$ at high irradiation and high decay times with the greatest underestimation of $\eta = 0.37\%$. This is likely due to the high fluence at these irradiation times, causing high burn-up of materials or causing multiple neutron interactions.

The materials in the sixth ring mostly experience $\eta \approx 1$. With some overestimation and some underestimation at high irradiation times. The maximum overestimation at high irradiation times is $\eta = 1.07$, which means a maximum overestimation of the photon emission density of 7%. The minimum underestimation is $\eta = 0.91$, which means the photon emission density is underestimated by 9%. The SteelB material sees an overestimation at low irradiation times similar to the one seen for SteelA material. The maximum overestimation is $\eta = 1.38$, which means that at those low irradiation times, the importance of the SteelB material will be overestimated by about 40%.

Moderator	Hydrogen	Hydrogen/Gadolinium	Water	Vacuum
	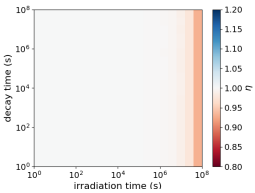	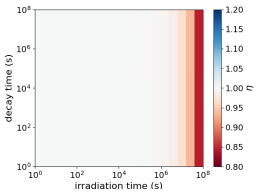	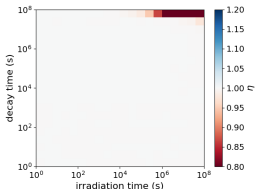	N/A
	0.93, 1.00	0.84, 1.00	0.37, 1.00	
SteelB	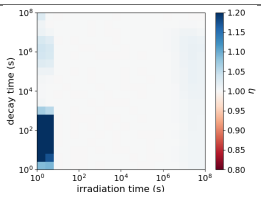	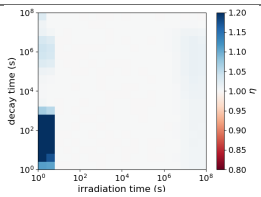	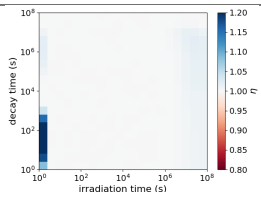	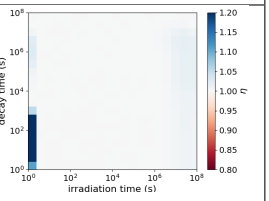
	1.00, 1.38	1.00, 1.38	1.00, 1.27	1.00, 1.35
Cadmium	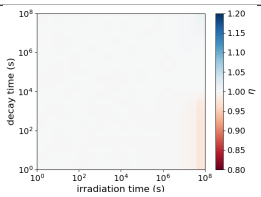	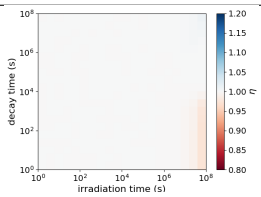	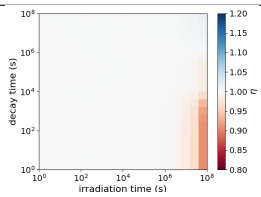	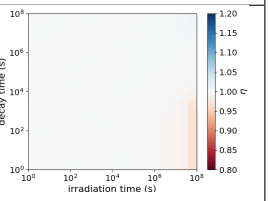
	0.98, 1.01	0.97, 1.01	0.91, 1.02	0.97, 1.01
AluminumA	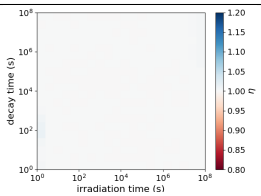	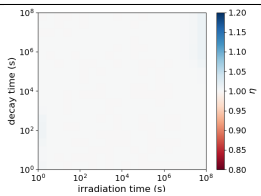	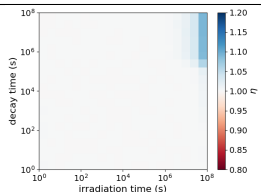	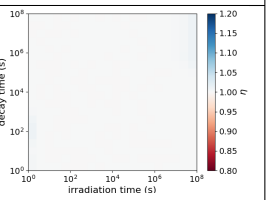
	0.99, 1.01	0.99, 1.01	0.99, 1.09	0.99, 1.01
AluminumB	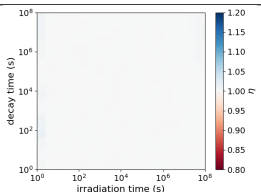	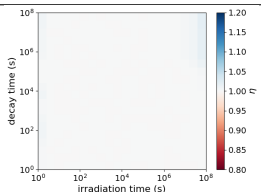	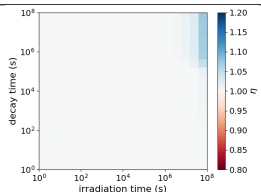	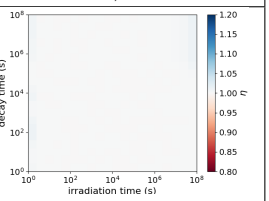
	0.99, 1.01	0.99, 1.02	0.99, 1.07	0.99, 1.01

Figure 6.8: η sweep for moderators and materials in the fifth ring

6.5 Conclusion

In this chapter, the extent to which the SNILB criteria are met for materials and spectra typical of accelerator-driven systems are explored. The test problem used for this exploration consisted of a simple 1 GeV proton source and materials typically seen in accelerator-driven systems. Different moderator materials are used in combination with other component ma-

terials in order to understand if the difference in flux experienced by these materials causes a difference in the SNILB criteria being met. The difference in flux experienced in materials is also explored by creating a geometry with four repeating sections that sit further from the source.

The quantity η was calculated for a suite of irradiation and decay scenarios. For most of these irradiation and decay scenarios and materials, η was found to be near 1. There are instances in which the SNILB criteria are violated for a material under a particular irradiation/decay scenario. Most of these violations occurred at low or high irradiation times. The maximum overestimation of photon emission density contribution for most of these violations was 38%. The one exception is the mercury volume furthest from the source, which overestimates the photon emission contributions by 200% at low irradiation times. The maximum underestimation was 20%, with the exception of water, which underestimates contributions at high irradiation times by 150%.

Chapter 7

High-Energy GT-CADIS Test Problem

A test problem was used to validate the implementation of the high-energy GT-CADIS. The test problem consists of two volumes: a mercury volume and a steel volume surrounding the mercury volume. A single detector was placed at $z = 200cm$, and a mono-directional 1 GeV disk neutron source is located at $z = -22cm$.

Two sets of VR parameters were created to optimize for the shutdown dose rate at the detector. The first set of VR parameters was created to optimize all neutron energy groups, and the second was done by optimizing only the neutron energy groups in the cross-section table range (up to 25 MeV). The VR parameters created by optimizing all neutron energy groups will be referred to as high-energy GT-CADIS, and the VR parameters created by optimizing the neutrons with energy less than 25 MeV will be referred to as the low-energy GT-CADIS. These two sets of VR parameters were generated to understand the improvement on an R2S calculation obtained when using low-energy GT-CADIS to generate neutron VR parameters for neutrons of energies less than 25 MeV, and the benefits obtained when using high-energy GT-CADIS.

7.1 Problem Description

The geometry for this problem is shown in Figure 7.1. The geometry consists of two volumes. The outer volume is a rectangular prism of dimensions 14 cm x 48 cm x 211 cm containing a steel material with compositions as defined in Table 7.1. The second volume is a mercury

volume with prongs with material composition defined in Table 7.2. The main body of the mercury volume has dimensions of 10 cm x 44 cm x 60 cm, and each of the prongs is 10 cm x 12 cm x 125 cm.

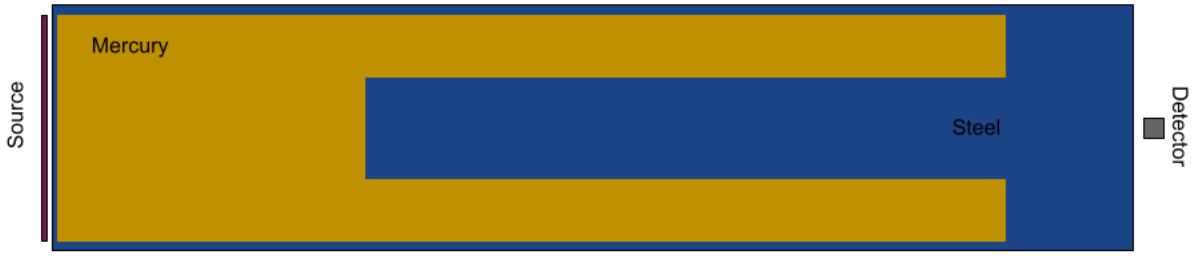

Figure 7.1: Cross-sectional view at $x = 0$ of test problem geometry

ZAID ZZZAAA	**Steel weight %**	**ZAID ZZZAAA**	**Steel weight %**
6000	0.08	26058	0.18
14028	0.91	27059	0.10
14029	0.05	28058	8.07
14030	0.03	28060	3.11
15031	0.04	28061	1.35
16032	0.03	28062	0.43
24050	0.73	28064	0.11
24052	14.07	42092	0.37
24053	1.60	42094	0.23
24054	0.40	42095	0.39
25055	1.98	42096	0.41
26054	3.74	42097	0.24
26056	59.12	42098	0.60
26057	1.42	42100	0.24

Table 7.1: Steel material composition

A 1 GeV disk mono-directional neutron source is located on the left side of the geometry. A detector is located on the right side of the geometry, where theSDR is calculated. The detector is a 4 cm x 4 cm x 4 cm cube. The photon dose rate is calculated at the detector after the irradiation schedule shown in Table 7.3 and a decay time of 106 days.

ZAID ZZZAAA	**Mercury atomic %**
80196	0.15
80198	9.97
80199	16.87
80200	23.10
80201	13.18
80202	29.86
80204	6.87

Table 7.2: Mercury material composition

Period (days)	Mean Power (kW)	Period (days) cont.	Mean Power (kW) cont.
14	0.00	7	0.00
7	682.23	7	0.00
7	731.39	7	0.00
7	770.78	7	0.00
7	770.93	7	0.00
7	675.72	7	185.59
7	533.22	7	888.73
7	1002.40	7	821.50
7	1158.50	7	1116.80
7	1118.00	7	811.60
7	1007.80	7	1083.60
7	875.56	7	1173.70
7	0.00		

Table 7.3: Test problem irradiation schedule

7.2 Generating GT-CADIS Weight Windows and Biased Source

To optimize the neutron transport of an R2S calculation, two implementations of the GT-CADIS method were used. The first implementation, named low-energy GT-CADIS, optimizes neutrons up to 25 MeV. The 25 MeV threshold is used because this is the highest neutron energy typically found in cross-section libraries used for high-energy problems. The second, named high-energy GT-CADIS, optimizes neutrons up to 2 GeV. This implementation uses a combination of cross-section libraries and production rates previously discussed.

For both workflows, the deterministic adjoint photon transport was done with ADVANTG

3.2 and the ENDF/B-VII.0 cross-section library, which has 47 photon energy groups. In order to keep as many variables as possible similar, both deterministic adjoint neutron transports were performed with the HILO2K cross-section library. HILO2K has 83 neutron groups between 10^{-5} eV and 2 GeV. For the low-energy GT-CADIS, the HILO2K library was truncated to 42 neutron energy groups, with the highest neutron energy being 25 MeV. For the high-energy GT-CADIS, all 83 neutron groups were used.

The adjoint photon source was chosen as a tally at the detector with flux-to-dose conversion factors created for SNS [24]. A mesh of size 7 x 24 x 44 was used for this deterministic adjoint photon transport. The adjoint photon flux is obtained over the previously described mesh for each of the 47 photon energy groups and for the total energy. Figures 7.2c- 7.2d show the adjoint photon flux for the photon energy groups $75 - 100$ KeV, $1.44 - 1.5$ MeV, $14 - 20$ MeV, and the total adjoint photon flux, respectively. These figures show that the important photons, for the SDR at the detector, increase as we move to the back of the geometry closest to the detectors, as expected. It also shows that higher energy photons are more important to the SDR as they are greater contributors to the total adjoint photon flux.

The photon emission density contributions from each neutron energy group and the neutron flux are needed to calculate $T(E_n, E_p)$. The neutron flux needed to calculate $T(E_n, E_p)$ does not need to be the actual flux in this test problem. The neutron flux can be an arbitrary neutron flux, as long as the flux is not so high that SNILB criteria is grossly violated and not so low that not enough activation is seen. The neutron flux calculated for the test problem in Chapter 6 was used. This neutron flux can be seen in Figure 6.2 for the Front area of the test problem. On the other hand, the calculation of photon emission density requires the net radionuclide production rate for interactions above 25 MeV. A neutron transport simulation was performed to obtain the net radionuclide production rate and the flux above 25 MeV. Figure 7.4 shows the production rate summed over all mesh volume elements, and Figure 7.3 shows the neutron flux for neutrons above 25 MeV.

The photon emission was calculated with the arbitrary flux for neutron groups below

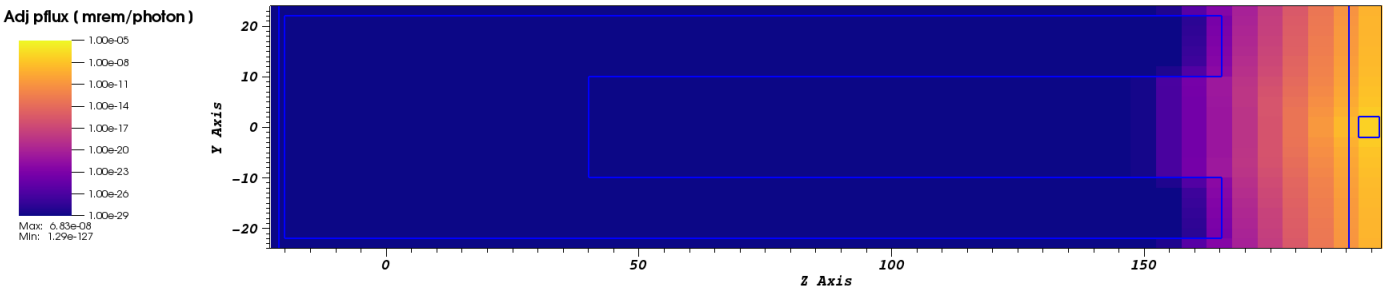

(a) Spatial distribution at $x = 0$, E_p = 75 - 100 KeV

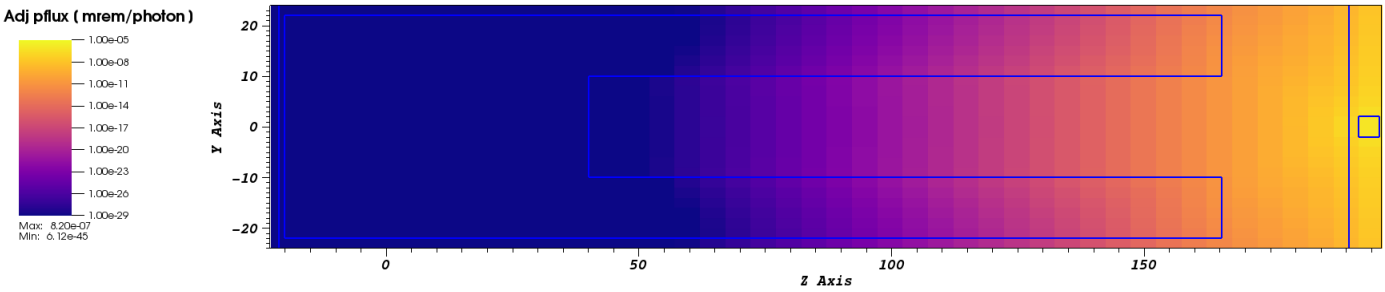

(b) Spatial distribution at $x = 0$, E_p = 1.44 - 1.5 MeV

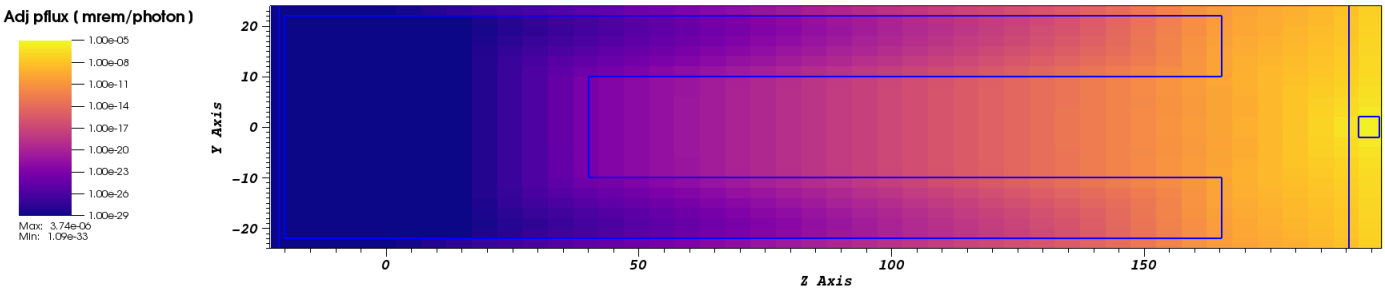

(c) Spatial distribution at $x = 0$, E_p = 14 - 20 MeV

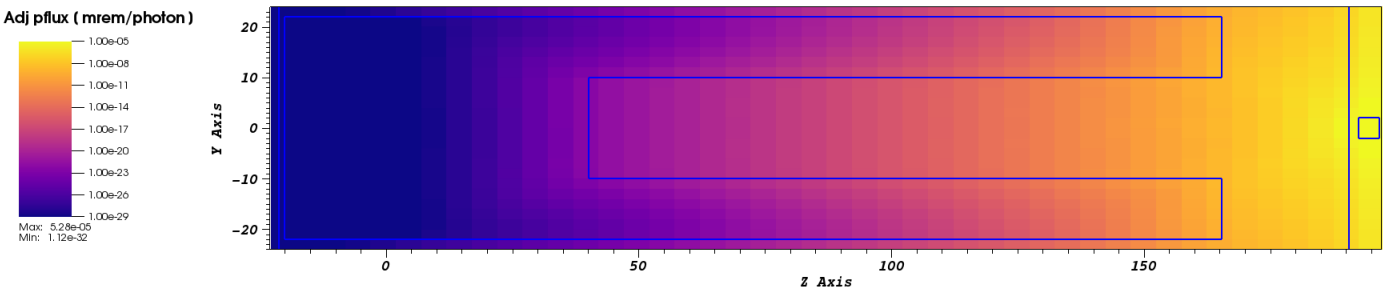

(d) Spatial distribution at $x = 0$, E_p = total

Figure 7.2: Adjoint photon flux distribution

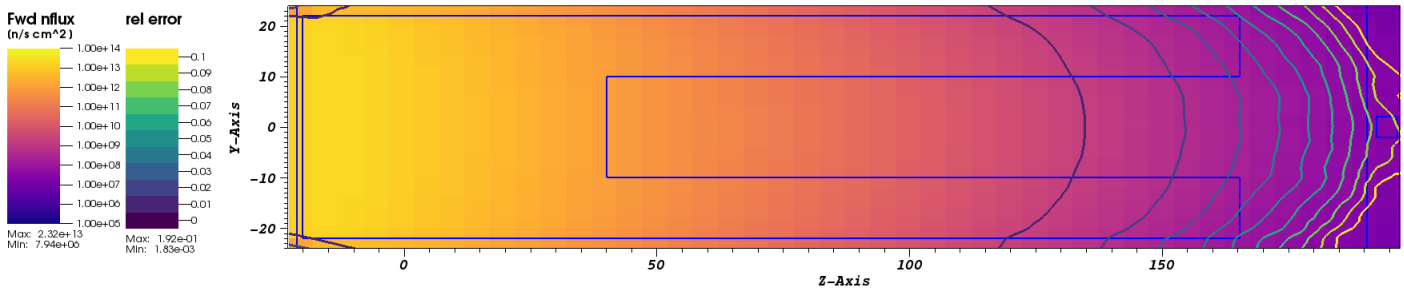

Figure 7.3: Forward neutron flux distribution x = 0, E = 25 - 2E3 MeV

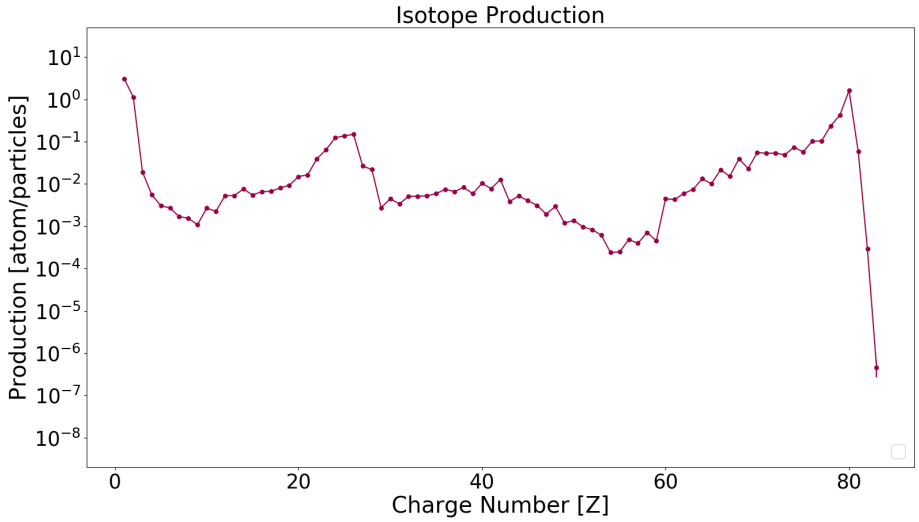

Figure 7.4: Radionuclide production rate

25 MeV and with the neutron flux and net radionuclide production rate from the neutron transport for neutron groups above 25 MeV. The photon emission density and flux were used to calculate the linearized activation operator, $T(E_n, E_p)$. $T(E_n, E_p)$ was originally calculated using the photon and neutron energy group structure used by CINDER90, as this is the format in which the neutron flux and photon emission density were calculated. $T(E_n, E_p)$ was then recast from the CINDER90 30-photon and 64-neutron energy group structure to the ENDF/B-VII.0 47-photon groups and the HILO2K 83-neutron energy groups. One important thing to note is that the neutron group structure used in the CINDER90 activation calculation has only one bin between 25 MeV and 2 GeV. This single group was recast to the HILO2K 41 groups between 25 MeV and 2 GeV. Figure 7.5 shows $T(E_n, E_p)$, which

has been summed over all photon energy groups, $T(E_n)$. Figures 7.5a and 7.5b show $T(E_n)$ for neutron energy groups $0.82 - 1.11$ MeV, and $19.6 - 25$ MeV, respectively. Both of these figures show that there are two distinct values of $T(E_n, E_p)$, which is expected as the neutron flux is the same for all mesh volume elements, and the only variable varying is the material composition. Figure 7.5b also shows that neutrons in the $19.6 - 25$ produce more photons in the steel material than in the mercury. Figures 7.5c and 7.5d show $T(E_n)$ for neutron energy groups $25 - 30$ MeV and $950 - 1000$ MeV, respectively. These figures show $T(E_n, E_p)$ varying in each mesh volume element because, in this energy range, the photon emission density is calculated with the net nuclide production rate and a neutron flux that varies in each mesh volume element. The neutrons in both of these energy bins produce more photons in the front of the geometry and decrease towards the back of the geometry.

7.2.1 Low-energy GT-CADIS VR Parameters

The adjoint neutron source is calculated using Equation 2.39. For low-energy GT-CADIS, $T(E_n, E_p)$ and the neutron flux were used for energy groups up to 25 MeV. Figures 7.6a - 7.6d show the adjoint neutron source for neutron energy groups $3.06 - 10.7$ eV, $0.82 - 1.11$ MeV, $8.61 - 10$ MeV, and $19.6 - 25$ MeV, respectively. These figures show that the neutron interactions most likely to produce important photons are located at the back of the geometry, closest to the detector of interest. These figures also show that the steel volume is more likely than the mercury volume to have neutron interaction likely to produce important photons.

The adjoint neutron source was used in Denovo for a deterministic adjoint neutron transport. Figures 7.7a - 7.7d show the adjoint neutron flux for neutron energy groups $3.06 - 10.7$ eV, $0.82 - 1.11$ MeV, $8.61 - 10$ MeV, and $19.6 - 25$ MeV, respectively. These figures show a larger adjoint neutron flux at the back of the geometry, which reinforces that the neutrons at the back of the geometry are most likely to generate photons, which might contribute to the SDR at the detector. These figures also show the adjoint neutron flux increases at the front

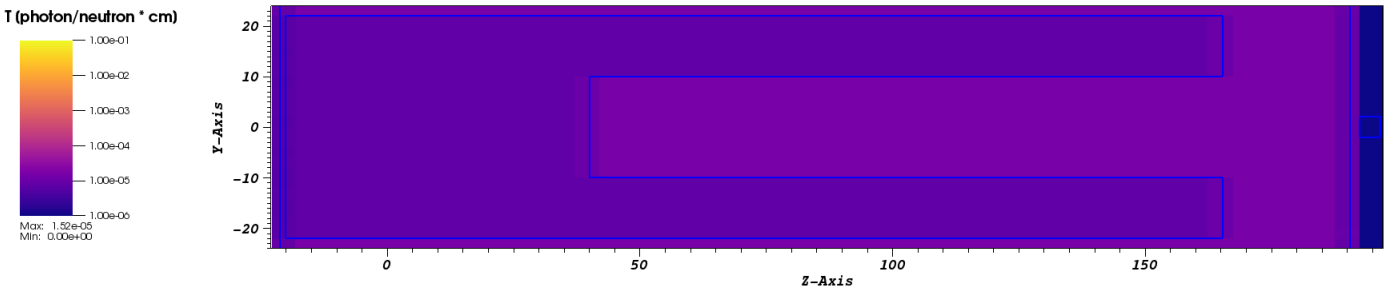

(a) Spatial distribution at $x = 0$, E_n = 0.82 - 1.11 MeV

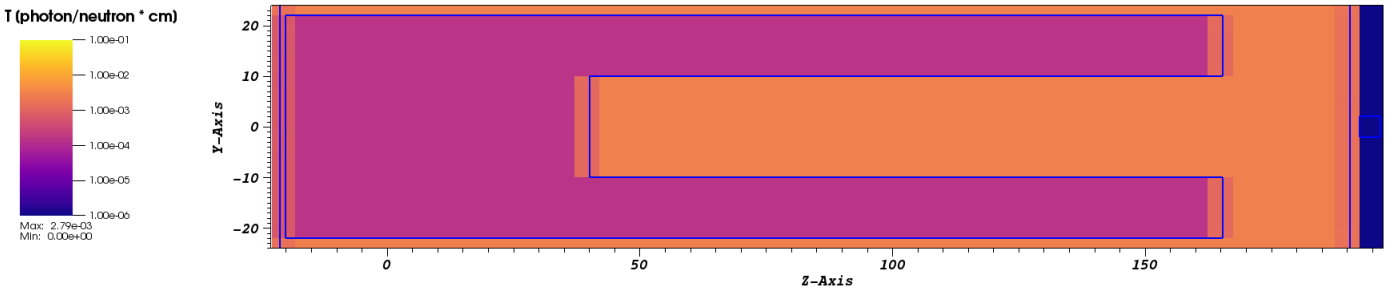

(b) Spatial distribution at $x = 0$, E_n = 19.6 - 25 MeV

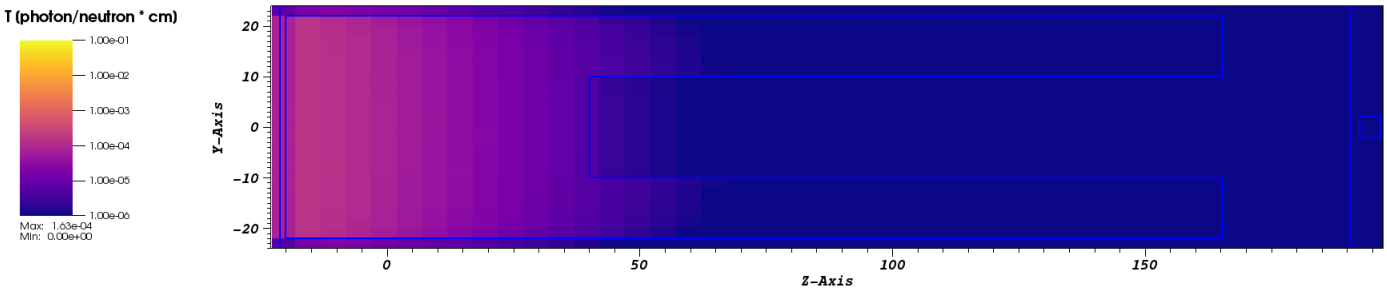

(c) Spatial distribution at $x = 0$, E_n = 25 - 30 MeV

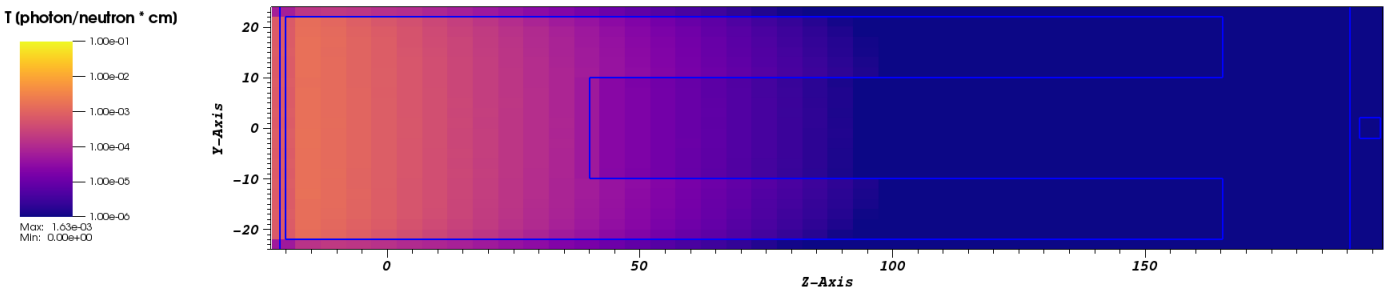

(d) Spatial distribution at $x = 0$, E_n = 950 - 1000 MeV

Figure 7.5: Linearized activation operator, T, for 180 days of irradiation and 106 days of decay

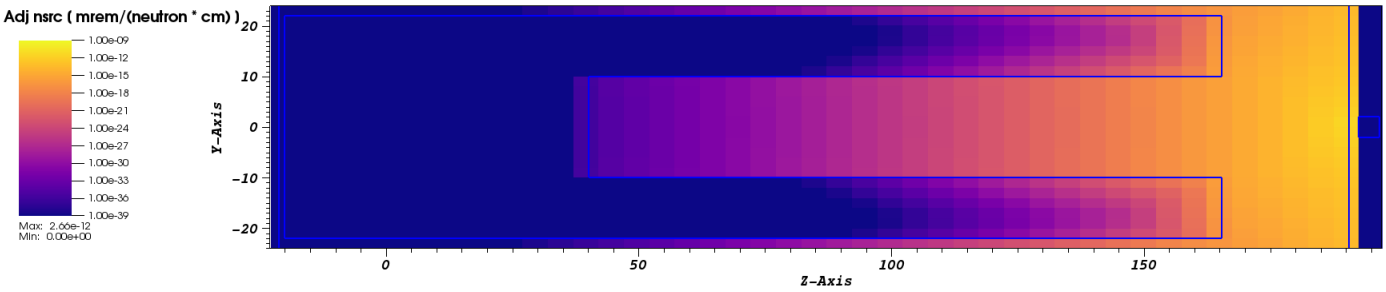

(a) Spatial distribution at $x = 0$, E_n = 3.06 - 10.7 eV

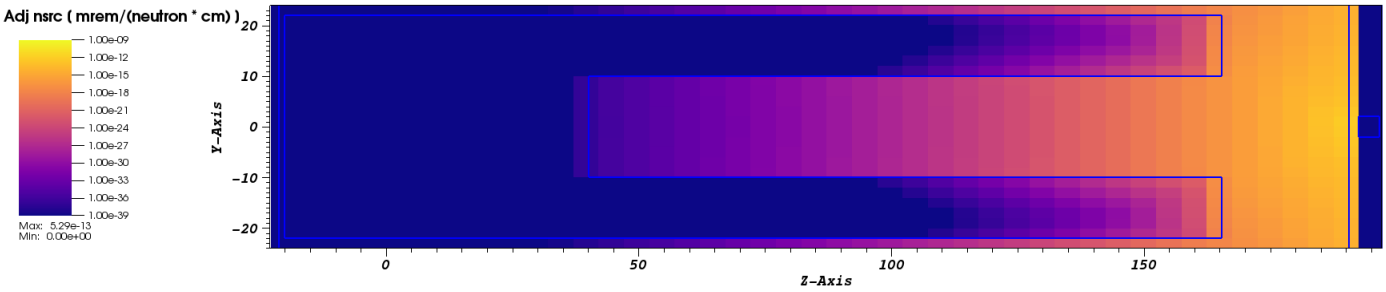

(b) Spatial distribution at $x = 0$, E_n = 0.82 - 1.11 MeV

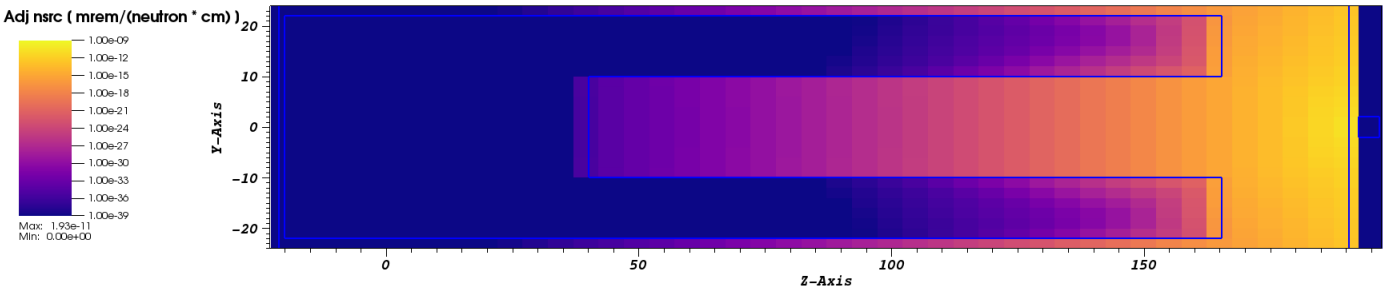

(c) Spatial distribution at $x = 0$, E_n = 8.61 - 10 MeV

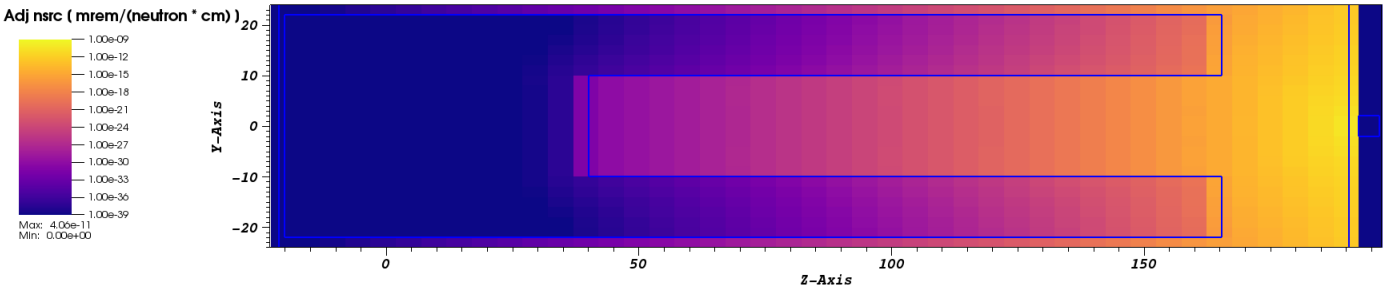

(d) Spatial distribution at $x = 0$, E_n = 19.6 - 25 MeV

Figure 7.6: Adjoint neutron source

of the geometry as the neutron energy increases. This means that higher energy neutrons are more important to the SDR.

ADVANTG 3.2 uses the adjoint neutron flux to calculate the biased source parameters and weight window lower bounds using Equations 2.28 and 2.29, respectively. The response needed in these equations is approximated by ADVANTG using Equation 2.25. The weight window lower bounds are shown in Figures 7.8a - 7.8d for neutron energy groups $3.06 - 10.7$ eV, $0.82 - 1.11$ MeV, $8.61 - 10$ MeV, and $19.6 - 25$ MeV, respectively. As expected, the weight window results mirror the adjoint neutron flux shown in Figure 7.7. All figures show a larger weight window lower bound at the front of the geometry, signifying a less important area to SDR at the detector. The largest weight window lower bounds are seen for the smallest energy group.

7.2.2 High-energy GT-CADIS VR Parameters

The adjoint neutron source for high-energy GT-CADIS is calculated using $T(E_n, E_p)$ and forward neutron fluxes for neutrons up to 2 GeV. The adjoint neutron source generated for neutron energy groups below 25 Mev are the same as for low-energy GT-CADIS, and are shown in Figure 7.6. Figures 7.9a - 7.9d show the adjoint neutron source for neutron energy groups $25 - 30$ MeV, $80 - 100$ MeV, $500 - 550$ MeV, and $950 - 1000$ MeV, respectively. The adjoint neutron source for neutron energy groups above 25 MeV is only slightly different. The reason for this is that for energy groups above 25 MeV, the linearized activation factor, $T(E_n, E_p)$, is calculated for one energy group photon emission density and flux and later cast to 40 energy groups.

The adjoint neutron source was then used for a deterministic adjoint neutron transport. Figures 7.10a - 7.10d show the adjoint neutron flux for neutron energy groups $25 - 30$ MeV, $80 - 100$ MeV, $500 - 550$ MeV, and $950 - 1000$ MeV, respectively. The adjoint neutron flux for neutron energy groups below 25 MeV is the same as for the low-energy GT-CADIS shown in Figure 7.7. These figures show that there is a significant amount of important neutrons at

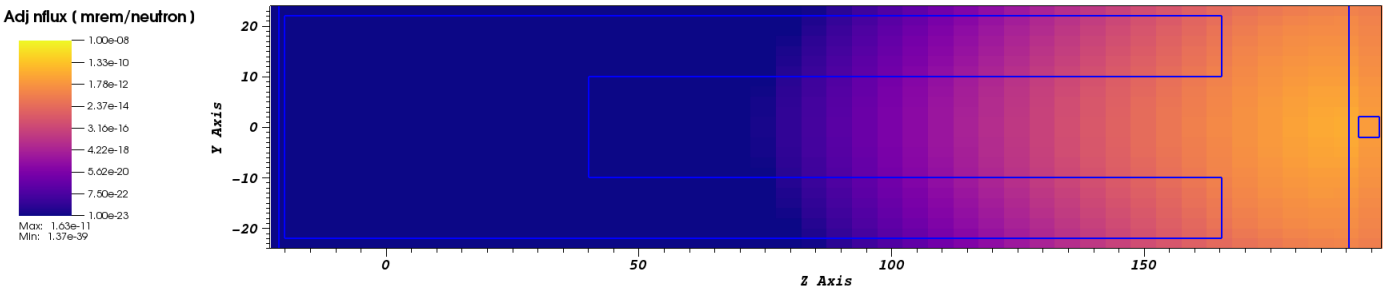

(a) Spatial distribution at $x = 0$, E_n = 3.06 - 10.7 eV

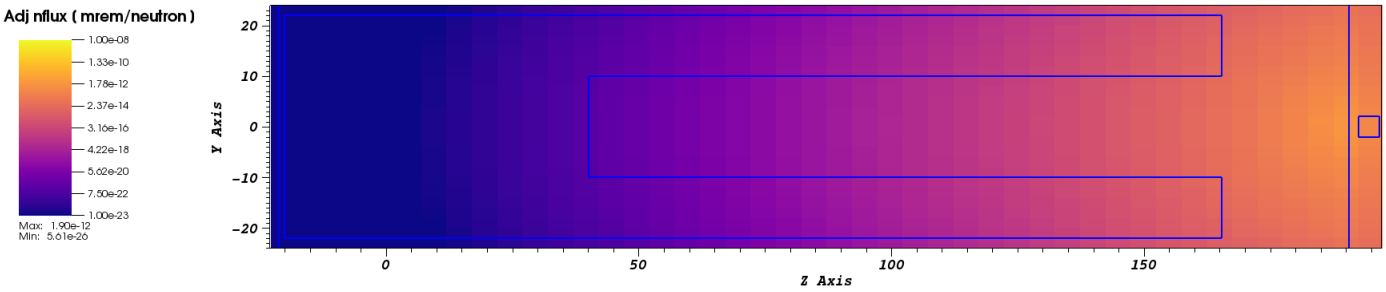

(b) Spatial distribution at $x = 0$, E_n = 0.82 - 1.11 MeV

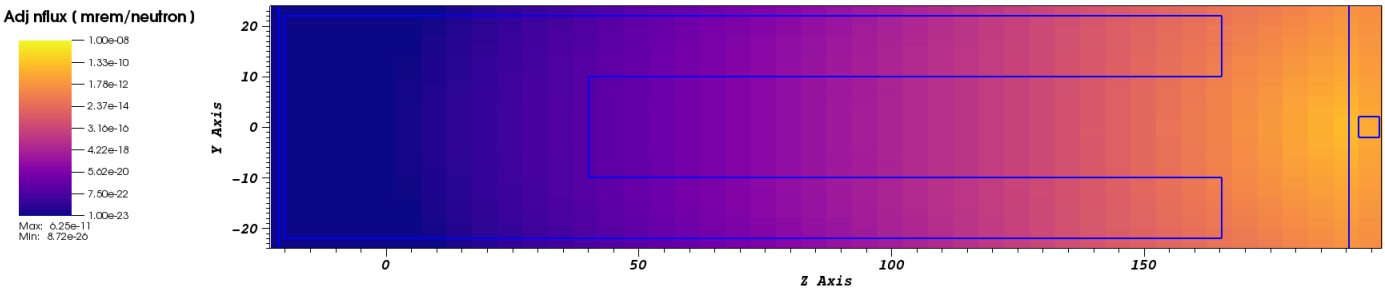

(c) Spatial distribution at $x = 0$, E_n = 8.6 - 10 MeV

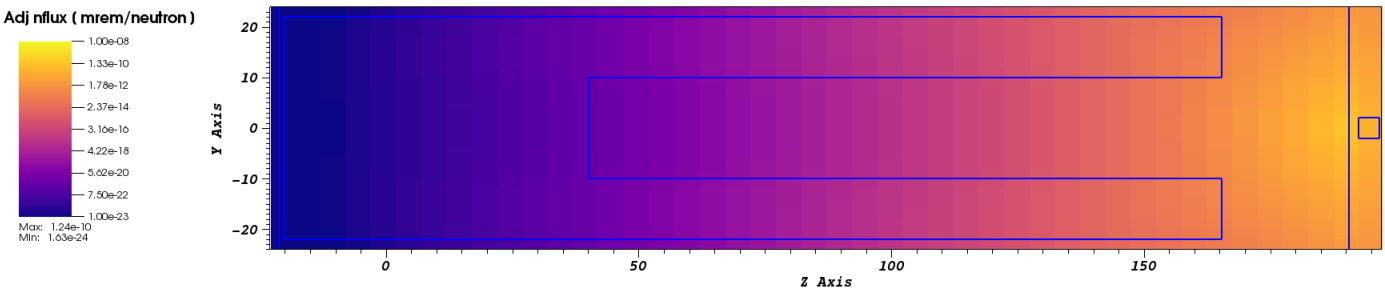

(d) Spatial distribution at $x = 0$, E_n = 19.6 - 25 MeV

Figure 7.7: Adjoint neutron flux

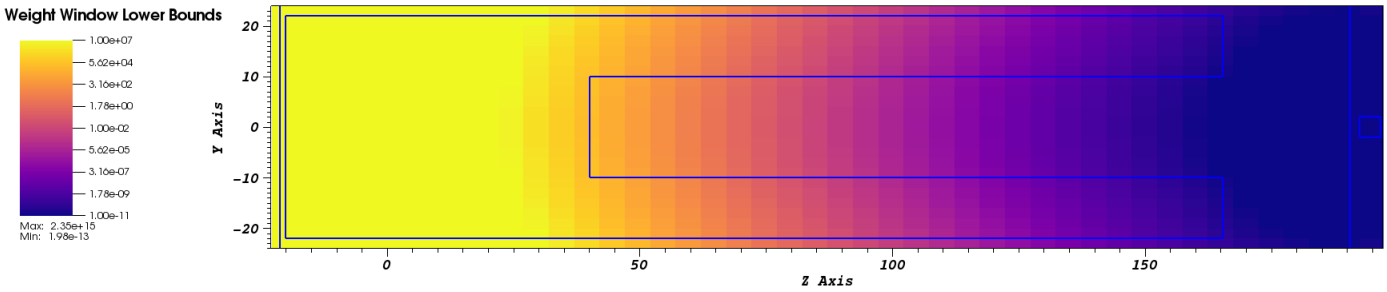

(a) Spatial distribution at $x = 0$, E_n = 3.06 - 10.7 eV

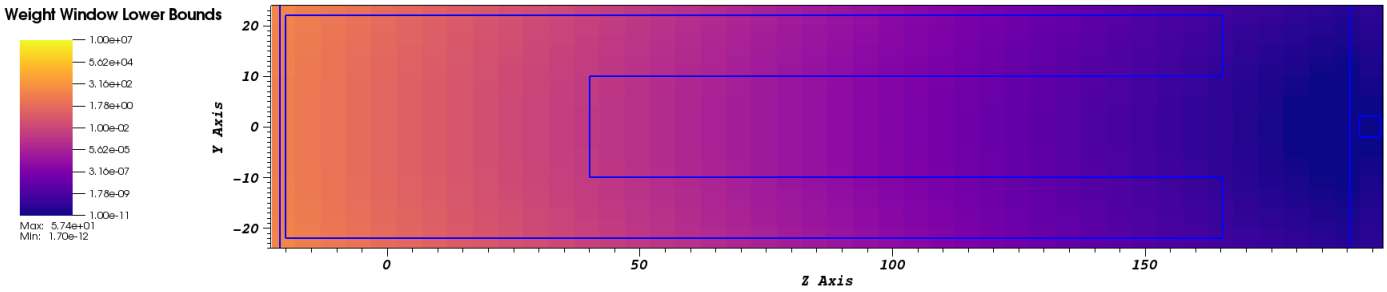

(b) Spatial distribution at $x = 0$, E_n = 0.82 - 1.11 MeV

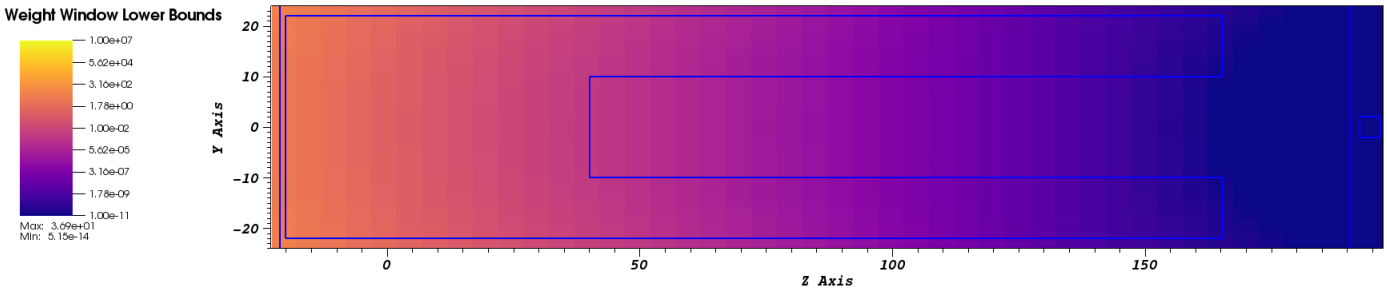

(c) Spatial distribution at $x = 0$, E_n = 8.6 - 10 MeV

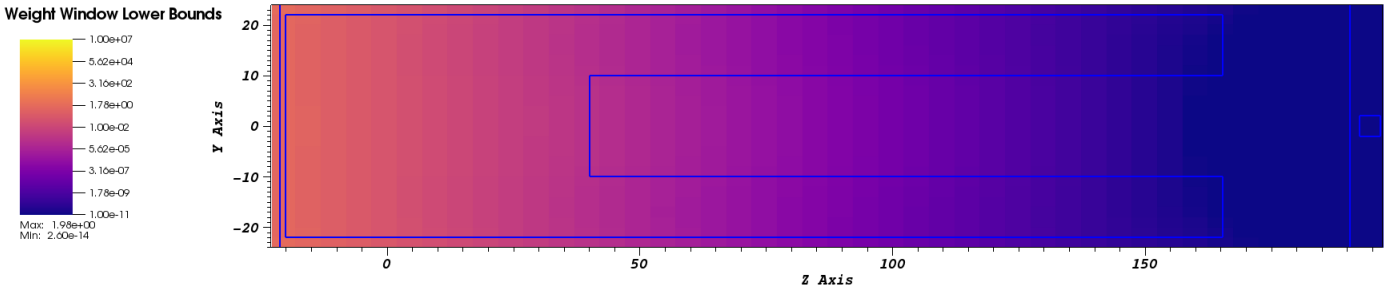

(d) Spatial distribution at $x = 0$, E_n = 20 - 25 MeV

Figure 7.8: Neutron weight window lower bounds

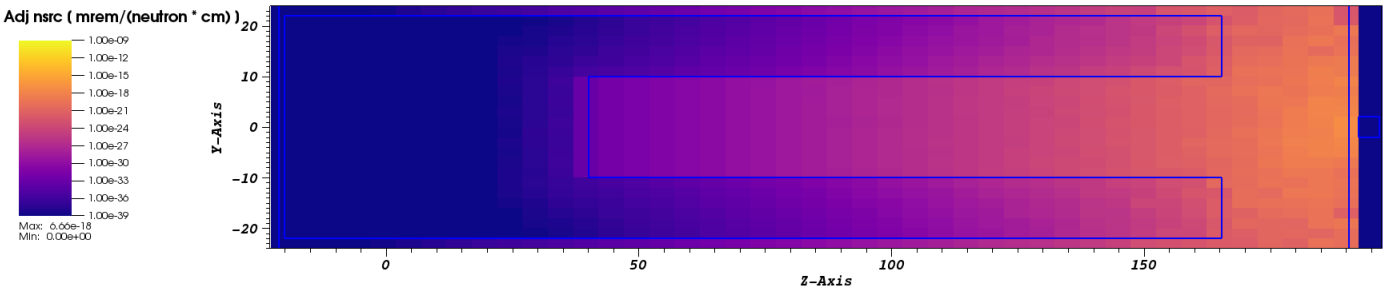

(a) Spatial distribution at $x = 0$, E_n = 25 - 30 MeV

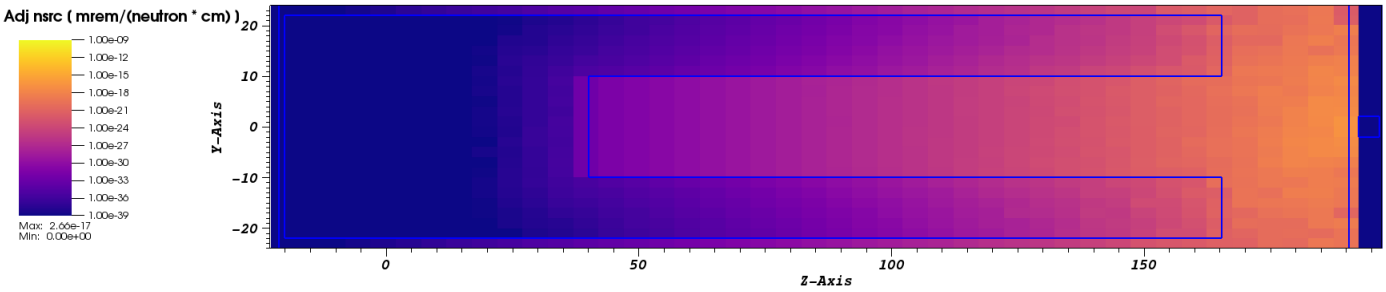

(b) Spatial distribution at $x = 0$, E_n = 80 - 100 MeV

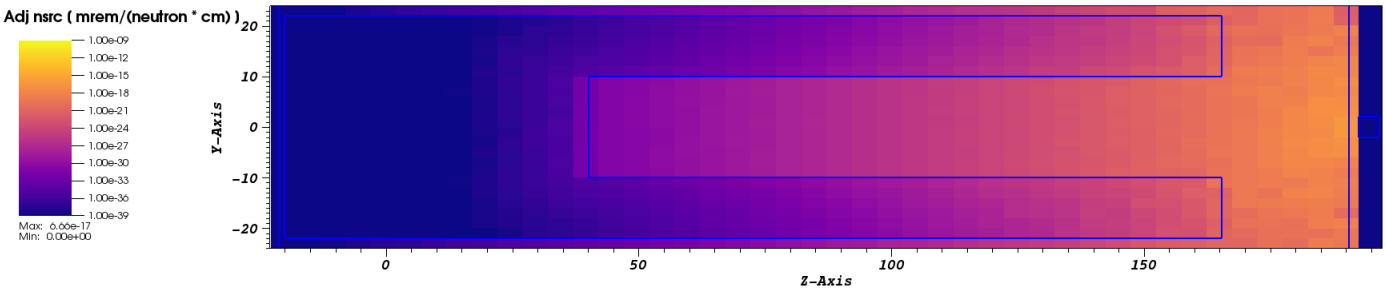

(c) Spatial distribution at $x = 0$, E_n = 500 - 550 MeV

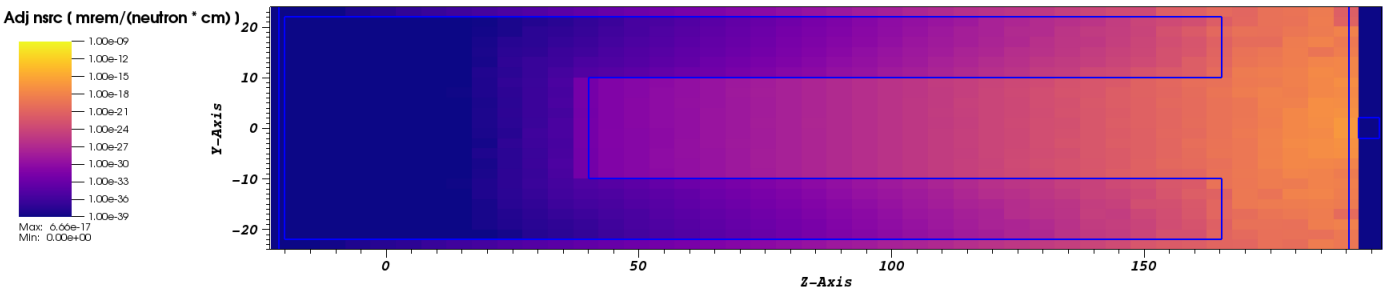

(d) Spatial distribution at $x = 0$, E_n = 950 - 1000 MeV

Figure 7.9: Adjoint neutron source for high-energy GT-CADIS

the front of the geometry close to the source. This is in contrast to the adjoint neutron flux for neutron energy below 25 MeV. This tells us that neutrons above 25 MeV are important to the SDR, particularly at the front of the geometry.

The adjoint neutron flux was then used by ADVANTG to generate weight windows lower bounds and source biasing parameters. Figures 7.11a - 7.11d show the weight window lower bounds for neutron energy groups $3.06 - 10.7$ eV, $8.61 - 10$ MeV, $80 - 100$ MeV, and $950 - 1000$ MeV. Figures 7.11a and 7.11b show the weight window lower bounds for two neutron groups below 25 MeV. Although these weight windows were generated using the same adjoint neutron flux as in the low-energy GT-CADIS workflow, the weight windows are different than in Figure 7.8. This is because the total response needed for the calculation of weight window lower bounds is generated, taking into account all neutron energies, as opposed to only neutrons below 25 MeV like in the case of the low-energy GT-CADIS.

7.3 R2S and SDR

In order to assess the advantages of the use of the VR parameters generated in Section 7.2, several R2S calculations were performed to obtain the SDR at the detector in the test problem. The first two calculations are analog R2S configurations. The first analog transport was performed with 2×10^7 particles, which is the same number of particles used for runs with VR. This analog run is a control result, as this run does not include any form of VR. The second analog run is performed with 12×10^7 particles to obtain a higher fidelity in neutron fluxes and production rates. The third and fourth calculations are an R2S with the high-energy GT-CADIS VR parameters and an R2S with the low-energy GT-CADIS VR parameters. These two configurations are chosen to inform the benefits of applying GT-CADIS VR parameters to only neutrons for which we have tabulated cross-section libraries (up to 25 MeV) and to all neutron energies using a combination of cross-section libraries and physics models. The fifth calculation is a modification of the low-energy GT-CADIS

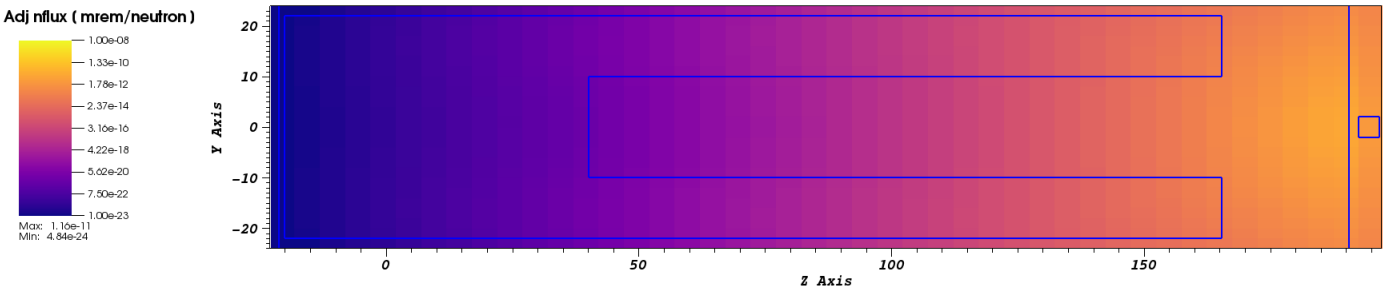

(a) Spatial distribution at $x = 0$, E_n = 25 - 30 MeV

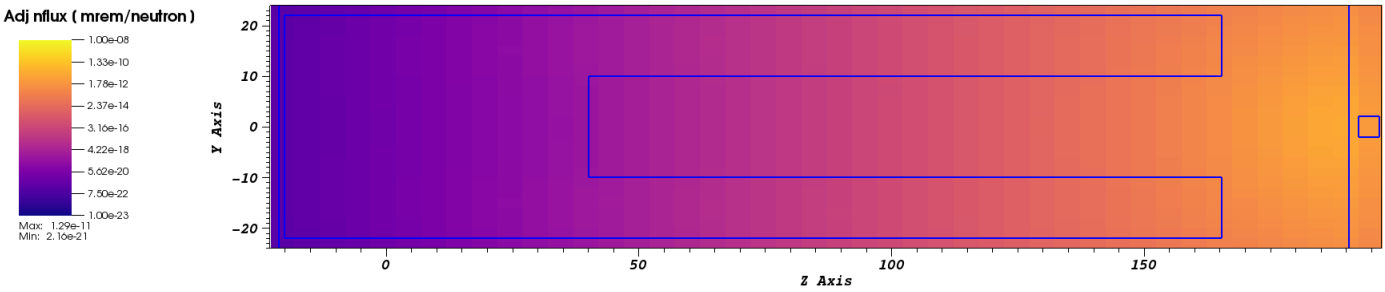

(b) Spatial distribution at $x = 0$, E_n = 80 - 100 MeV

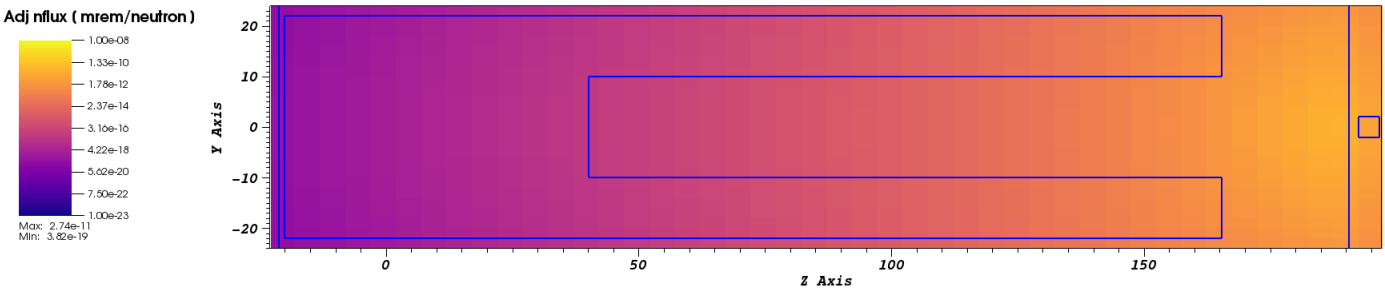

(c) Spatial distribution at $x = 0$, E_n = 500 - 550 MeV

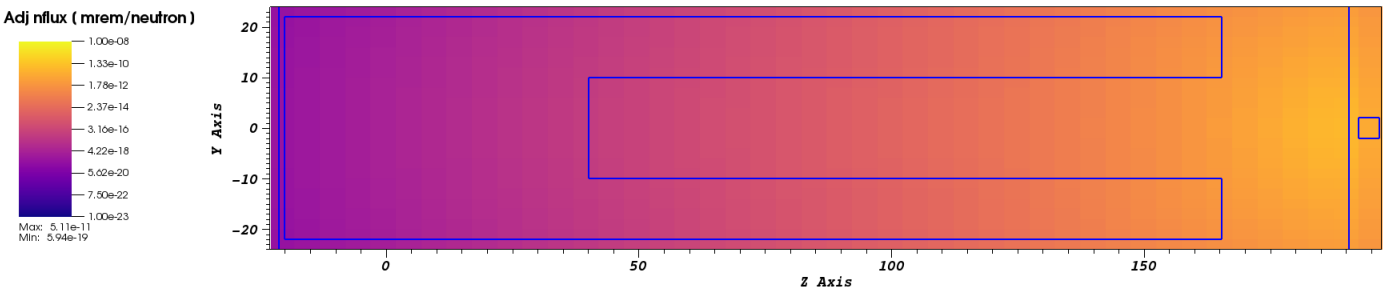

(d) Spatial distribution at $x = 0$, E_n = 950 - 1000 MeV

Figure 7.10: Adjoint neutron flux

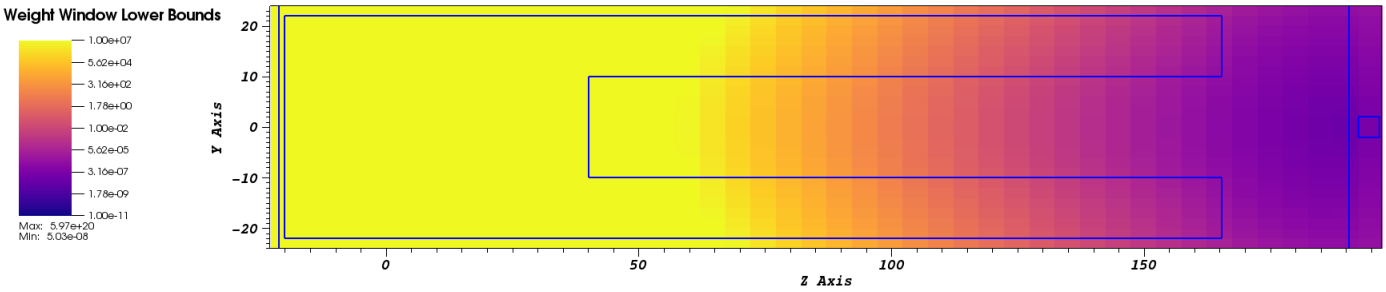

(a) Spatial distribution at $x = 0$, E_n = 3.06 - 10.7 eV

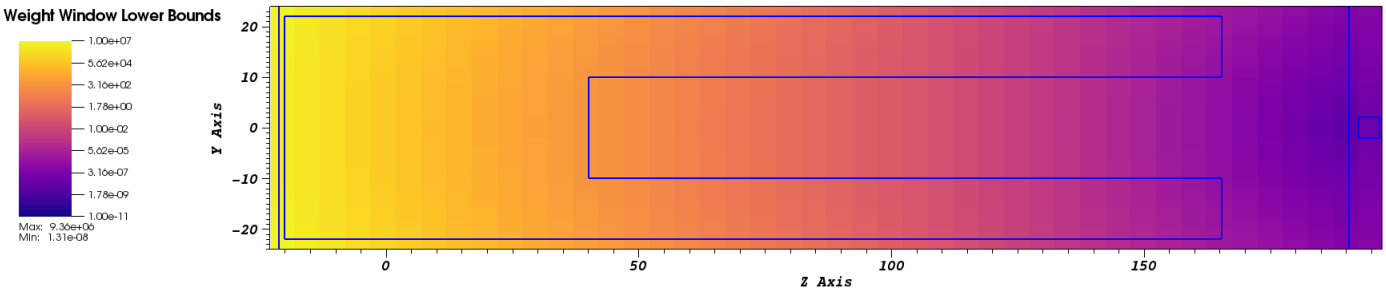

(b) Spatial distribution at $x = 0$, E_n = 8.61 - 10 MeV

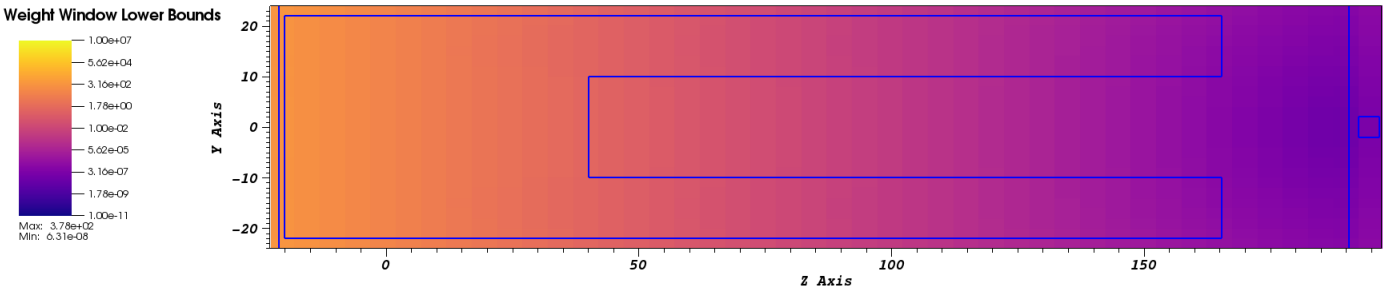

(c) Spatial distribution at $x = 0$, E_n = 80 - 100 MeV

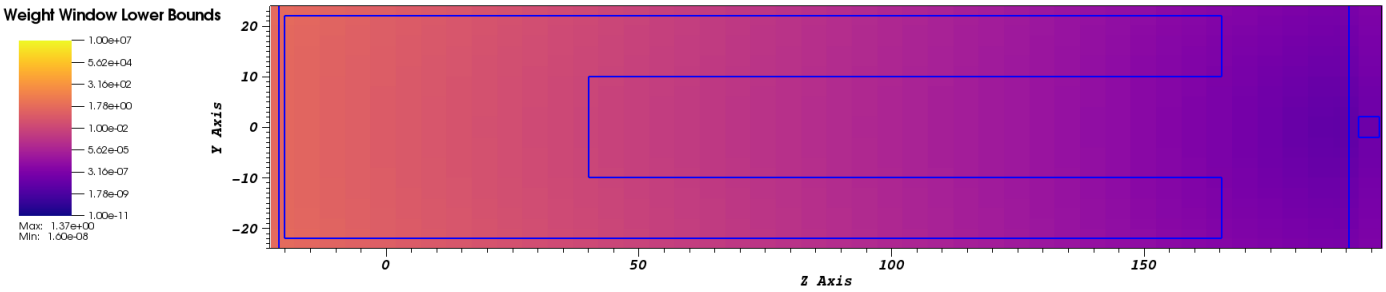

(d) Spatial distribution at $x = 0$, E_n = 950 - 1000 MeV

Figure 7.11: Neutron weight window lower bounds

calculation. This modification is needed because the neutron transport using the original low-energy GT-CADIS VR parameters is unable to finish within a reasonable time. The

modification consisted of using the total response, R, calculated from the high-energy GT-CADIS workflow as opposed to the low-energy GT-CADIS workflow. In the original low-energy GT-CADIS, the total response is approximated using the contribution from neutrons up to 25 MeV, yielding a response smaller than that for the high-energy GT-CADIS. The implications of using these responses are further discussed in Section 7.3.1.

7.3.1 Neutron Flux

A neutron transport was carried out for the five different configurations previously discussed. The one of the analog, the high-energy GT-CADIS, and the modified low-energy GT-CADIS neutron runs were performed with 2×10^7 particles. The second analog transport was performed with 12×10^7 particles. The original low-energy GT-CADIS neutron transport was not able to be completed within a reasonable time frame, and only 15×10^5 particles were transported.

The neutron transport calculation with the VR parameters generated with the original low-energy GT-CADIS indicated that a long history might be causing the stagnation of the problem. Several attempts were performed with different starting particles, and all led to the neutron transport not finishing within a reasonable time. One explanation for this long history is related to the weight windows generated for this problem. The weight windows shown in Figure 7.8 are obtained by optimizing for neutrons up to 25 MeV. This figure shows that the weight windows for the two neutron groups between $16 - 25$ MeV are lower than those generated with high-energy GT-CADIS, shown in Figure 7.11. The weight window lower bounds are calculated with Equation 2.29, which needs the adjoint neutron flux and an approximate of the response, R. ADVANTG approximates the response using Equation 2.25 with the original, unbiased source and the calculated adjoint neutron flux. The approximation of the response is a partial approximation as the adjoint neutron flux is only calculated up to 25 MeV. This means that the response for higher energy neutrons is not considered, affecting the final weight window lower bounds. Considering that there is

no weight windows treatment for neutrons above 25 MeV, imagine a neutron source particle of 1 GeV being born at the left side of the geometry with the weight of one. This high-energy neutron will then travel across the geometry, interacting with the materials and losing energy. When the particle has reached an energy of 25 MeV or less, then the weight window treatments are applied, but now this particle might have some high weight and enter a low-weight window area, causing it to split into many particles. Each of these lower-weight particles is then followed and can split even more, which can be the cause of this problem's long history.

The fifth run, or modified low-energy GT-CADIS neutron transport, was run with the weight windows generated using the full response calculated with high-energy GT-CADIS. The weight windows for the energy group above 25 MeV were set to 0. This ensured that not VR was applied for neutrons above 25 MeV.

Figures 7.12, 7.13, and 7.14 show the neutron flux with the corresponding error for each of the five runs. Figure 7.12 shows the neutron flux distribution for energies $20 - 25$ MeV. These figures show that the analog runs have a relative error greater than 10% at the back of the geometry, but when high-energy GT-CADIS is used, then the relative error at the back of the geometry becomes less than 10%. It is important to note that the error in the neutron flux at the front of the geometry is higher with the use of high-energy GT-CADIS than analog. This is expected as the neutrons in this region are less likely to contribute to the SDR at the detector at the back of the geometry. This is further supported by the adjoint neutron source shown in Figure 7.9a. Figure 7.12d shows the neutron flux with low-energy GT-CADIS after only 15×10^3 particle were transported, so the relative error in the whole geometry is greater than 10%. Figure 7.12e shows the neutron flux with modified low-energy GT-CADIS. This figure shows that more particles are moving to the back of the geometry, and the relative error is improving compared to the analog transport, suggesting that the VR is favoring particles important to the SDR response at the detector.

The neutron fluxes for energies above 25 MeV are shown in Figure 7.13. The high-energy

GT-CADIS neutron flux shown in Figure 7.13c shows less than 10% relative error for most of the geometry. Figure 7.13e shows relative errors similar to that of analog. This is expected as no weight windows are being applied in this energy region.

Lastly, Figure 7.14 shows the total neutron flux and relative error of each of the five neutron transports. The plots in this figure show that the high-energy GT-CADIS has a low relative error at the back of the geometry where neutrons are most important. It also shows that for the modified low-energy GT-CADIS, there is some variance reduction, but it is not as pronounced as the high-energy GT-CADIS variance reduction.

These neutron flux plots have shown that the statistical error for high-energy GT-CADIS is reduced for the important neutron regions. This is further corroborated by the neutron transport FOM shown in Figure 7.15, where it is shown that the neutron transport FOM is increased by up to 10^5 times that of the analog at the back of the geometry. The opposite is seen at the front of the geometry, where the neutrons are not as important to the SDR at the detector.

The low-energy GT-CADIS has some challenges that can be remedied if a more complete response approximation is used. Although, in this case, the full response was available, this is not likely the case in many circumstances. Because the partial response low-energy GT-CADIS was not able to run more than 15×10^3 particles, the rest of the R2S run will not be included in this work.

7.3.2 Photon Source

The neutron flux and the net nuclide production rates were used in an activation calculation to obtain the photon emission density. This photon emission density was then converted into a mesh photon source using the computational tools described in Chapter 3. Figures 7.16 and 7.17 show the mesh photon source generated for the analog run with relative errors. Figures 7.16a and 7.17a show the photon source with the minimum possible relative error, and Figures 7.16b and 7.17b show the same photon source with the maximum possible

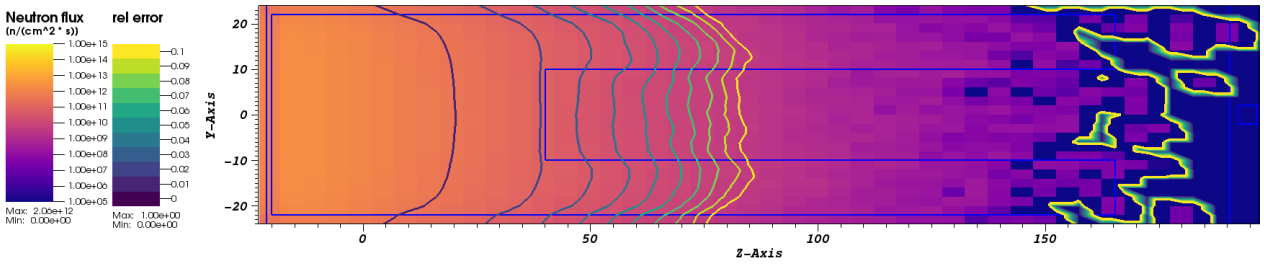

(a) Analog (2×10^7 particles)

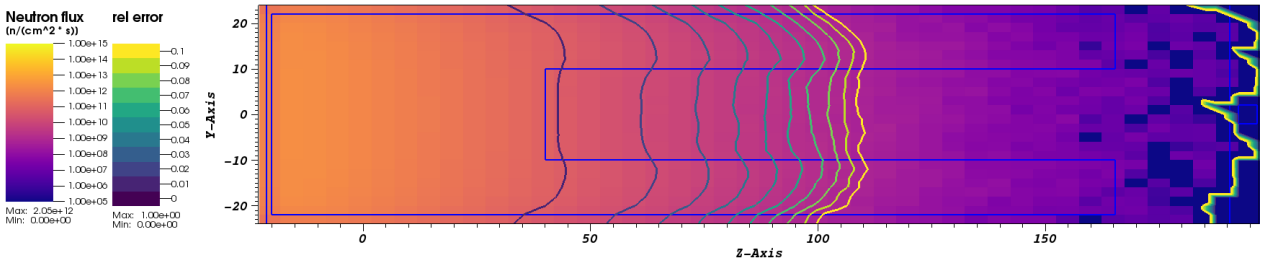

(b) Analog (12×10^7 particles)

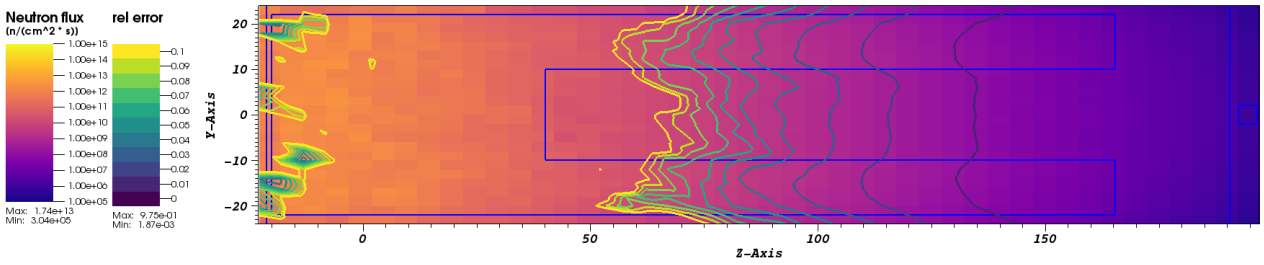

(c) High-energy GT-CADIS

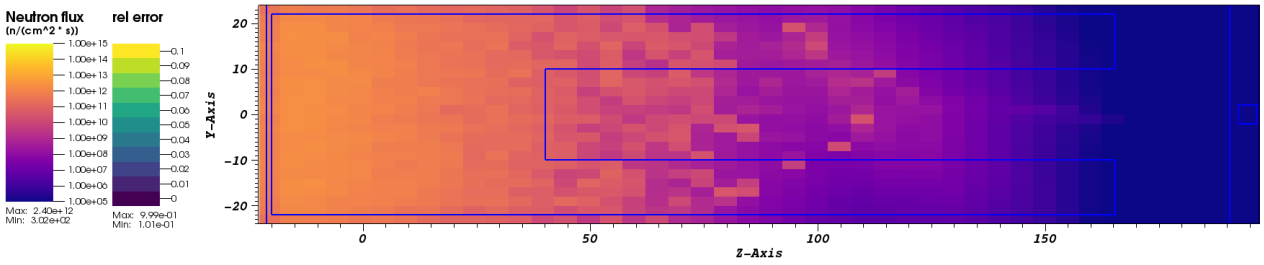

(d) Low-energy GT-CADIS, partial response

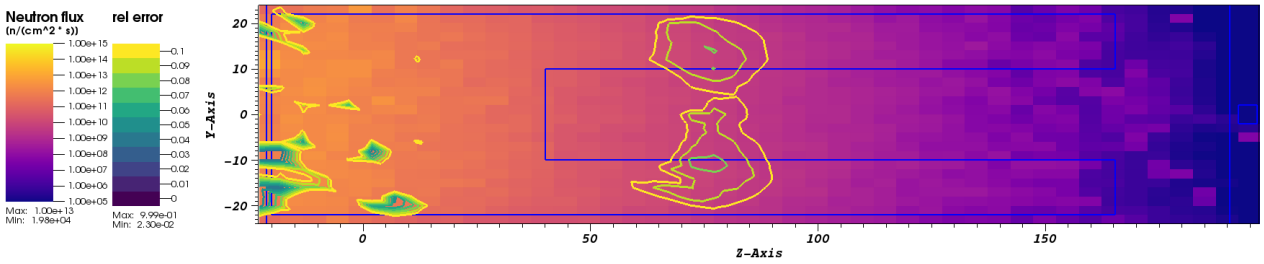

(e) Low-energy GT-CADIS, full response

Figure 7.12: Neutron flux distribution and relative error at $x = 0$, $E_n = 20 - 25$ MeV

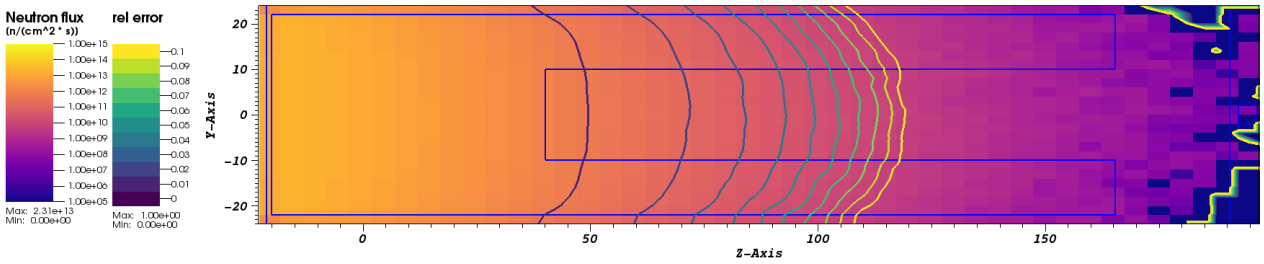

(a) Analog (2×10^7 particles)

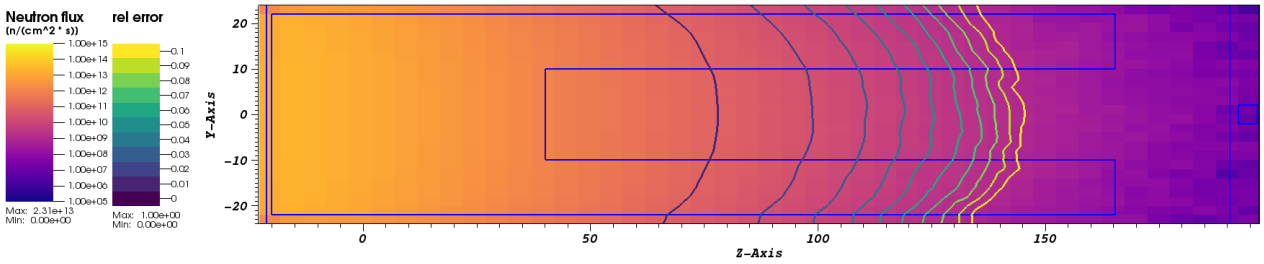

(b) Analog (12×10^7 particles)

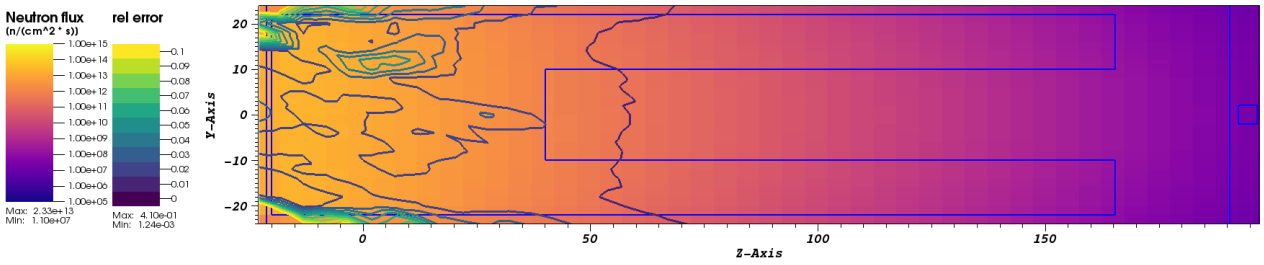

(c) High-energy GT-CADIS

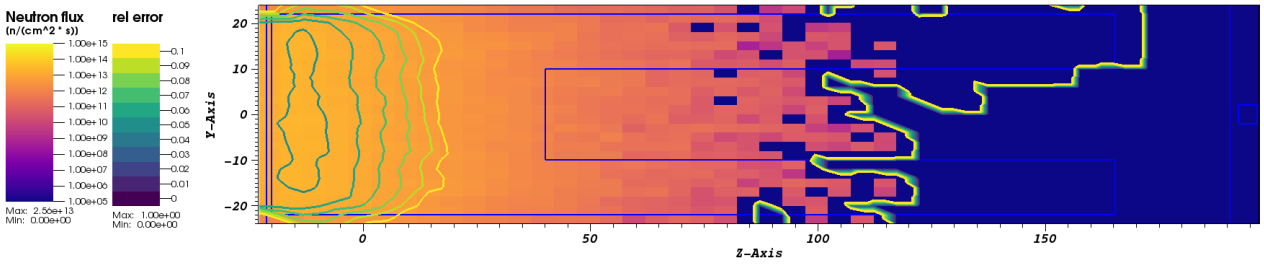

(d) Low-energy GT-CADIS, partial response

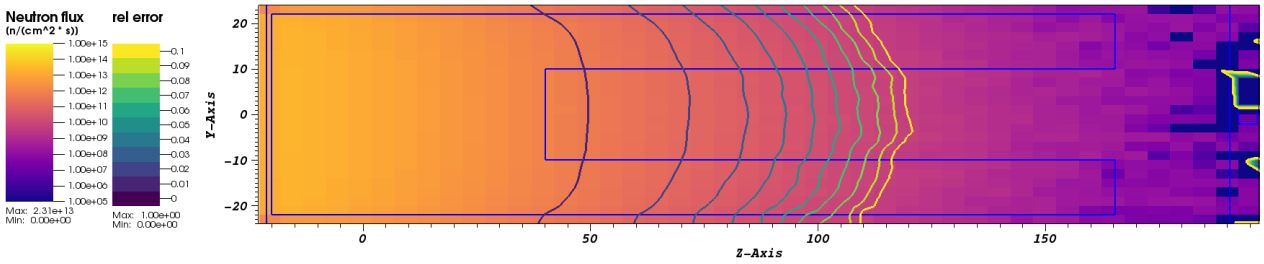

(e) Low-energy GT-CADIS, full response

Figure 7.13: Neutron flux distribution and relative error at $x = 0$, $E_n = 25\ MeV - 2\ GeV$

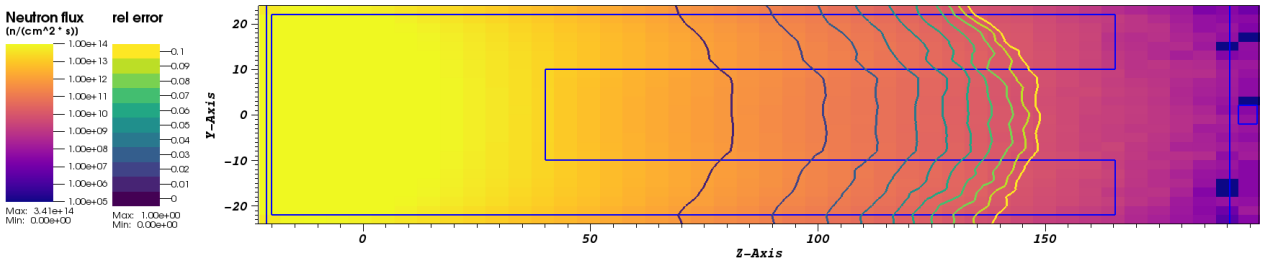

(a) Analog (2×10^7 particles)

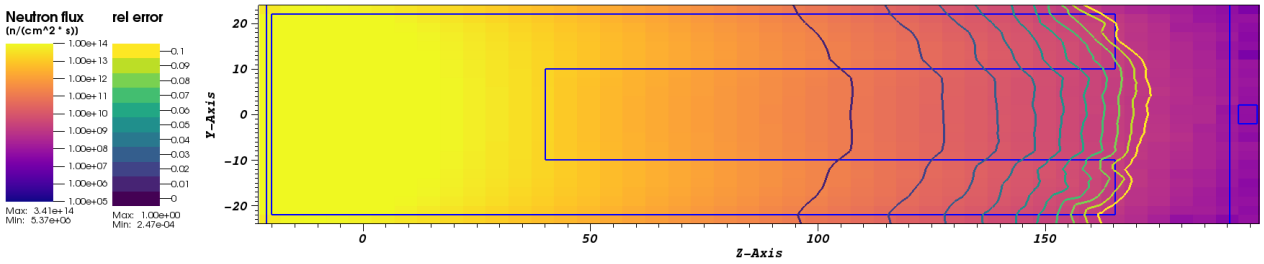

(b) Analog (12×10^7 particles)

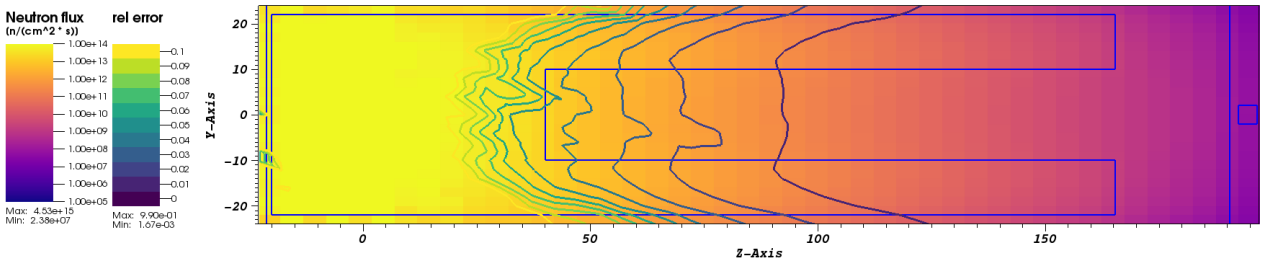

(c) High-energy GT-CADIS

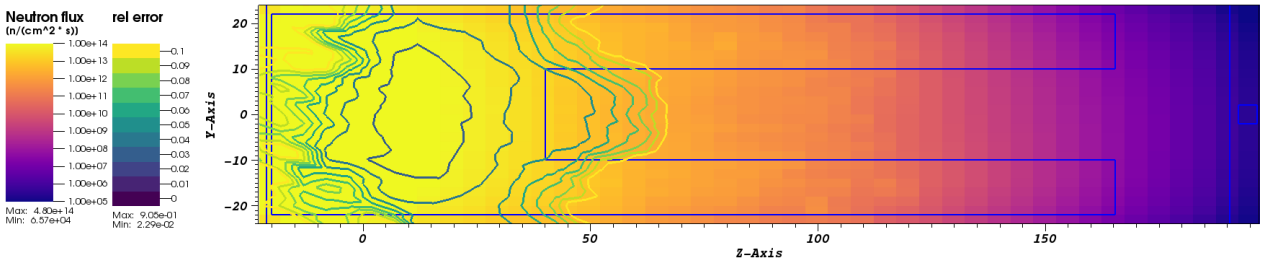

(d) Low-energy GT-CADIS, partial response

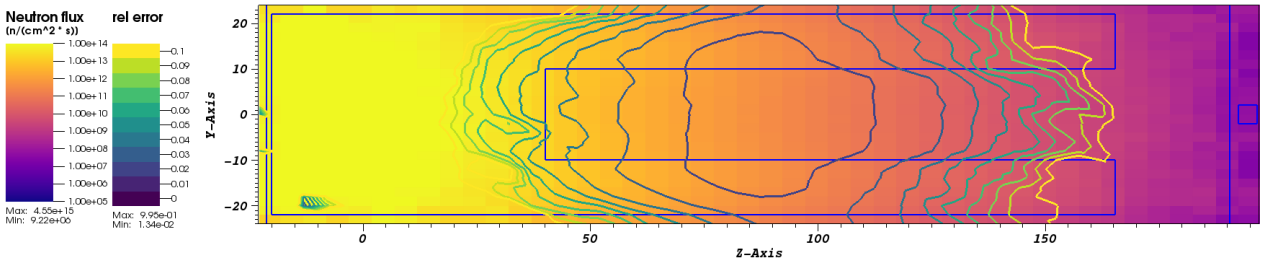

(e) Low-energy GT-CADIS, full response

Figure 7.14: Neutron flux distribution and relative error at $x = 0$, E_n = total

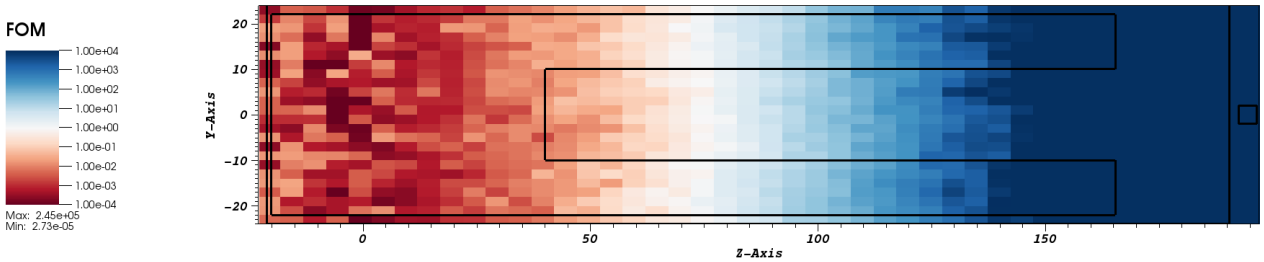

(a) Spatial distribution at $x = 0$, E_n = 20 - 25 MeV

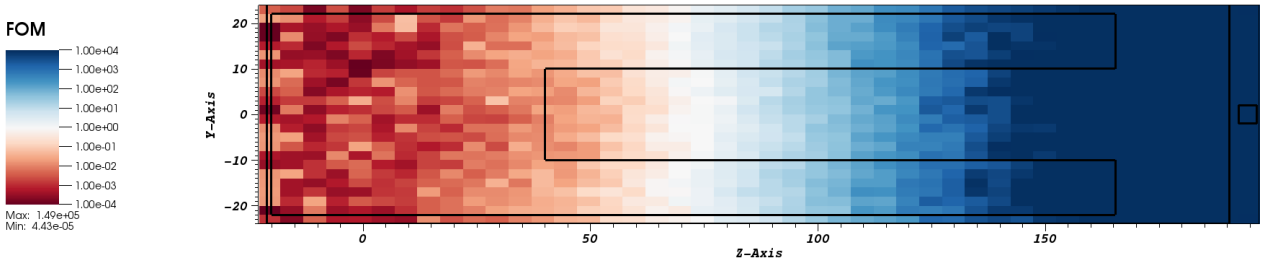

(b) Spatial distribution at $x = 0$, E_n = 25 - 30 MeV

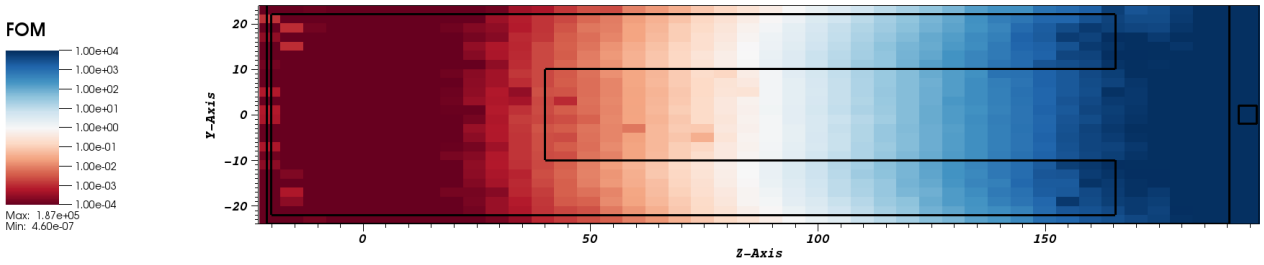

(c) Spatial distribution at $x = 0$, E_n = total

Figure 7.15: Figure of Merit ratio (high-energy GT-CADIS / analog)

relative error. Both of these relative errors were computed using the work developed by Harb et al. [20] discussed in Section 2.5.1.

Figures 7.18 and 7.19 show photon source for the low-energy GT-CADIS and for the high-energy GT-CADIS workflows, respectively. The photon source and the error for the high-energy GT-CADIS have improved at the back of the geometry when compared to the analog counterparts. A similar improvement is seen in low-energy GT-CADIS when compared to the first analog photon source, but when compared to the high-energy GT-CADIS, the photon source at the back of the geometry is not as uniform. This is expected as there are no VR being applied to the high-energy neutrons, and they end up having a higher relative error than those seen with high-energy GT-CADIS. Overall, the photon source in the high-energy GT-CADIS workflows is more uniform at the back of the geometry than the other three runs,

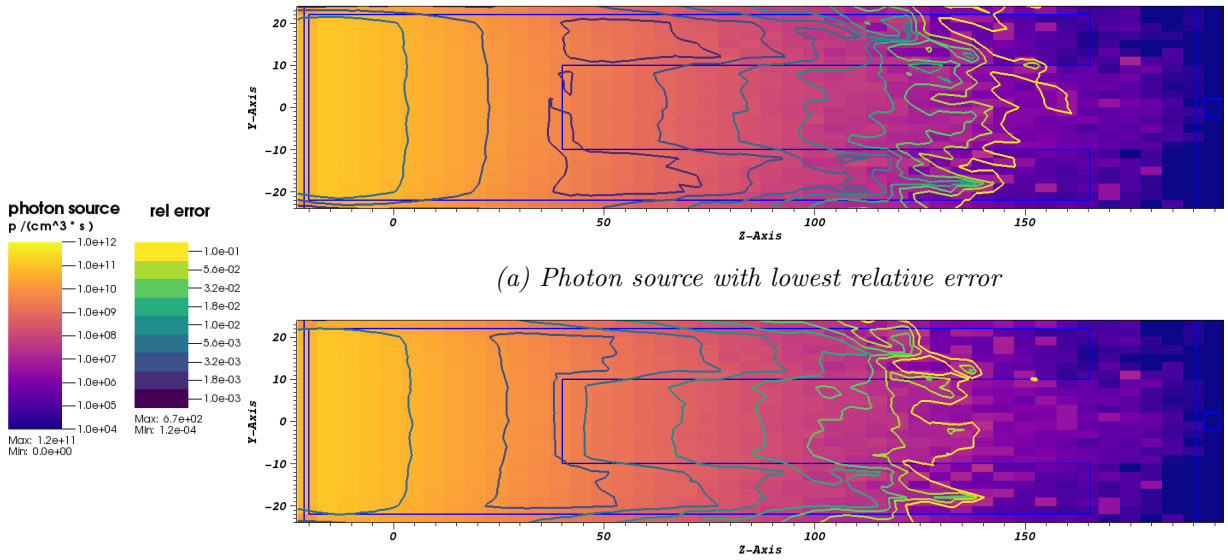

(a) Photon source with lowest relative error

(b) Photon source with highest relative error

Figure 7.16: Total photon source - analog (2×10^7)

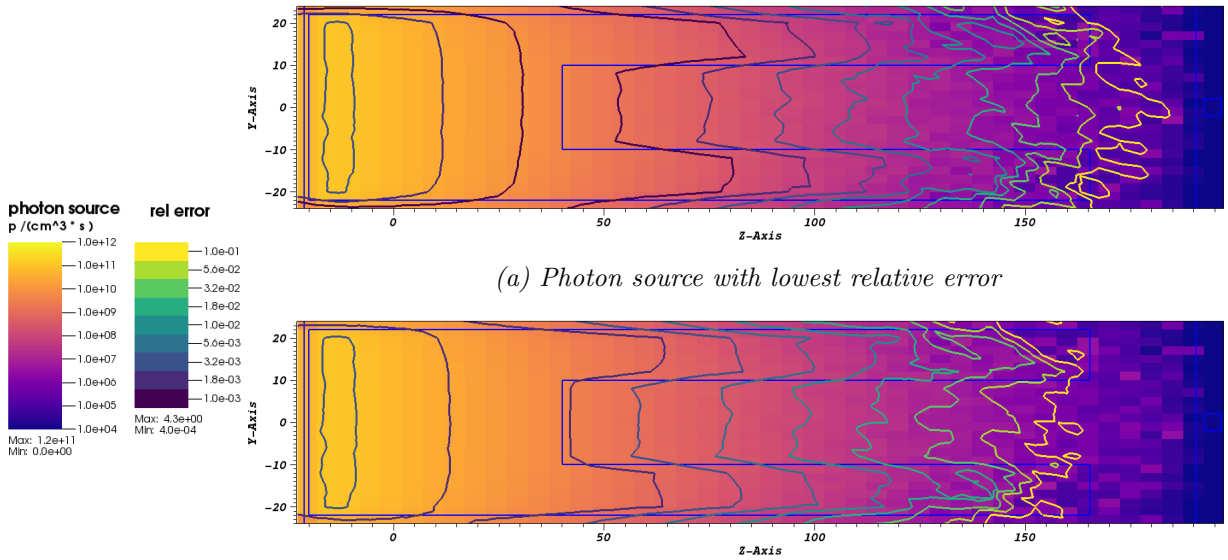

(a) Photon source with lowest relative error

(b) Photon source with highest relative error

Figure 7.17: Total photon source - analog (12×10^7)

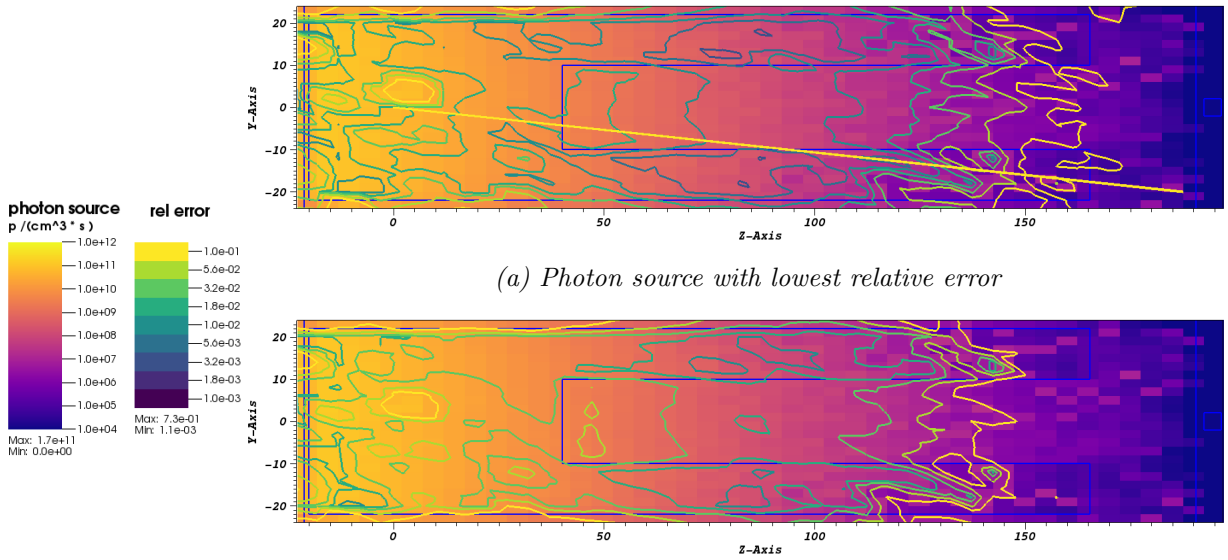

(a) Photon source with lowest relative error

(b) Photon source with highest relative error

Figure 7.18: Total photon source - low-energy GT-CADIS

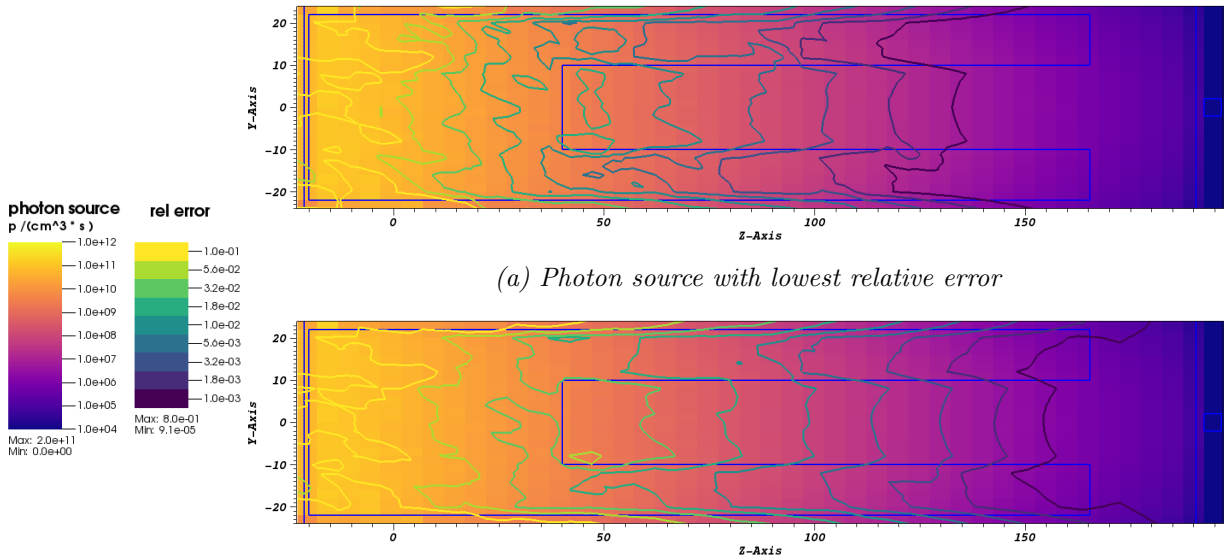

(a) Photon source with lowest relative error

(b) Photon source with highest relative error

Figure 7.19: Total photon source - high-energy GT-CADIS

which have a higher error and a spotty definition of the source at the back of the geometry.

7.3.3 Photon Dose Rate

The photon source generated is used in a photon transport to obtain the photon dose rates, which are calculated using the SNS flux-to-dose conversion rates [24]. Table 7.4 shows the photon dose rate at the detector for each of the four runs. The relative error shown in this table only accounts for the error in the photon transport and does not account for the error in the photon source. The relative error of the first analog run and the modified low-energy GT-CADIS are higher than those for the second analog with higher particles and the high-energy GT-CADIS. One potential explanation for this is the similarities of the photon source between the two runs shown in Figures 7.16 and 7.18. The photon source obtained with the longer analog run yields a slightly different source with some improvements in the uniformity of the source at the back of the geometry. This leads to a lower relative error in the photon dose rate. The photon source obtained with the high-energy GT-CADIS run has the most different source with greater uniformity of the source at the back of the geometry, and the relative error is the smallest of all runs.

The photon dose rate obtained with the high-energy GT-CADIS VR parameters is two times greater than the analog with the same number of particles and two and half times greater than the low-energy GT-CADIS. The photon dose rate obtained with the longer analog run is only 10% smaller than the high-energy GT-CADIS results. This longer analog run helps gain confidence in the high-energy GT-CADIS results since it approaches the dose rate obtained with the high-energy hGT-CADIS VR parameters.

Figure 7.20 shows photon dose rates and relative error for a tally that covers the geometry and the top and back of the geometry. This figure shows that the results for the analog run and low-energy run are very similar, and the error in the high-energy run is improved at the back of the geometry.

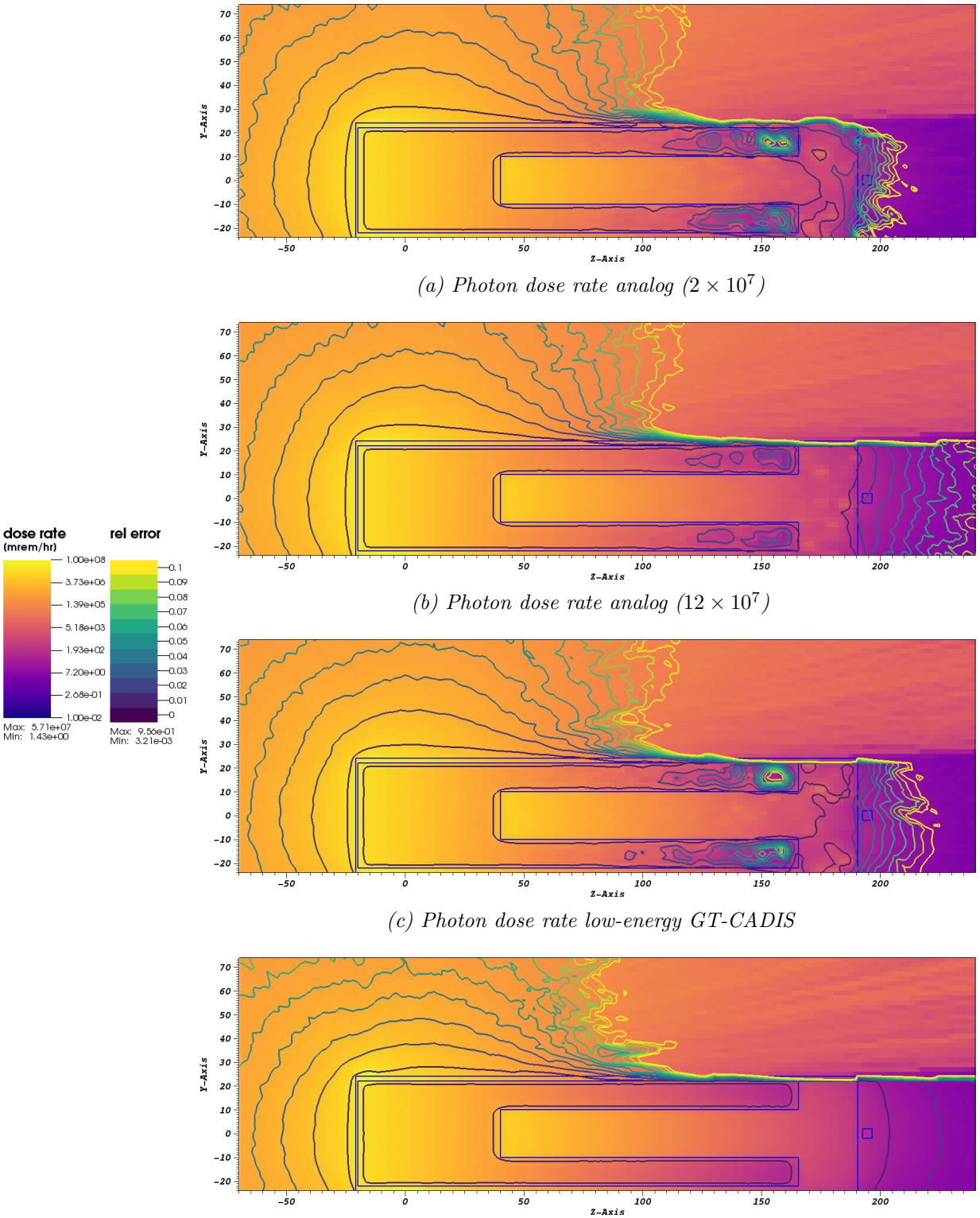

(a) Photon dose rate analog (2×10^7)

(b) Photon dose rate analog (12×10^7)

(c) Photon dose rate low-energy GT-CADIS

(d) Photon dose rate high-energy GT-CADIS

Figure 7.20: Total photon dose rate - high-energy GT-CADIS

Table 7.4: Photon dose rate

	Dose Rate [mrem/hr]	**Relative error**
analog (2×10^7)	52.0	0.0242
analog (12×10^7)	97.0	0.0101
low-energy GT-CADIS	44.2	0.0204
high-energy GT-CADIS	107	0.0030

7.4 Conclusion

In this chapter, a simple test problem was used to demonstrate the implementation of GT-CADIS for high-energy neutrons and low-energy neutrons. The test problem consisted of a 1 GeV neutron source, a mercury volume, a steel volume, and a detector. Two sets of VR parameters were generated using GT-CADIS to optimize the neutron transport of the SDR at the detector calculation. The first set of VR parameters was generated using low-energy GT-CADIS, which optimizes neutrons of energies up to 25 MeV. The second set of VR parameters was generated using high-energy GT-CADIS, which optimizes neutrons up to 2 GeV.

Several R2S calculations were performed using no VR parameters and using both low-energy and high-energy GT-CADIS VR parameters. An issue was encountered related to the low-energy GT-CADIS VR parameters generated. The weight windows and source biasing parameters generated with this workflow use only a partial approximation of the response. This is because only energy-limited neutron cross-section information is available for ADVANTG 3.2. This partial response approximation reduces the magnitude of the weight window parameters, causing the particles in the neutron transport to split multiple times. This, in turn, caused the transport calculation to stall and not finish. In order to assess how the implementation of the high-energy GT-CADIS compares to the low-energy GT-CADIS, the full response calculated with high-energy GT-CADIS was used for the low-energy GT-

CADIS.

The neutron flux for four R2S workflows (analog with 2×10^7 particles, analog with 12×10^7 particles, high-energy GT-CADIS, and modified low-energy GT-CADIS) were compared. The statistical uncertainty for both GT-CADIS workflows decreases at the back of the geometry and increases at the front of the geometry compared to the analog runs. The photon source is also affected by the use of GT-CADIS VR parameters. In the case of the low-energy GT-CADIS workflow, the R2S calculation does not have any VR in the neutron region above 25 MeV, and this affects the generation of the mesh photon source. The analog run and low-energy GT-CADIS generate a mesh photon source that is not well defined at the back of the geometry, closest to the detector. In the case of the longer analog run, the photon source is more uniformly distributed at the back of the geometry than the previous two runs but not nearly as uniform as the high-energy GT-CADIS run. The high-energy GT-CADIS generates a photon source with better statistical uncertainty and a more uniform definition at the back of the geometry. The differences in photon source translate to the SDR result and relative error at the detector. For analog with 2×10^7 particles and low-energy GT-CADIS, the SDR at the detector were 52 mrem/hr with 2.4% error and 44.2 mrem/hr with 2.0% error, respectively. The analog with 12×10^7 yielded a photon dose rate of 97 mrem/hr with 1% error, and for the high-energy GT-CADIS, the SDR at the detector was 107 mrem/hr with 0.3% error. The high-energy GT-CADIS results are much higher than both the shorter analog run and the low-energy GT-CADIS run. The longer analog run was chosen to transport 6 times the particles of the shorter analog run, and it yielded a SDR that is only 10% smaller than the high-energy GT-CADIS. The long analog result provides confidence that a longer analog run might converge to the same results as the high-energy GT-CADIS.

This chapter showed that the high-energy GT-CADIS implementation reduces the variance in the SDR at a location of interest more efficiently than with low-energy GT-CADIS when compared to an analog run. The FOM for the high-energy GT-CADIS is 10^5 times

greater in regions of importance than the FOM of analog neutron transport. It is also shown that implementing GT-CADIS using cross-sectional libraries that only partially describe the interactions of the neutron can lead to over-splitting in the neutron transport, potentially causing a neutron transport calculation to take a long time to transport all the particles.

Chapter 8

Performance of the High-energy GT-CADIS Method

This chapter demonstrates the performance of the High-energy GT-CADIS method with a simple problem. In the problem, a 1 GeV neutron source irradiates a steel box with a mercury volume inside. The SDR is measured with a single detector at the back of the steel box. The materials and irradiation scenarios are chosen to be similar to those used in accelerator-driven systems. The method described below used to demonstrate the performance of the High-energy GT-CADIS method is based on the work performed by Biondo et al. [5].

Neutron weight windows and source biasing parameters were generated using the high-energy GT-CADIS method. MC neutron transport was carried out in analog and with high-energy GT-CADIS VR parameters. For each method, MC neutron transport was carried out for four different processor times between 10^2 minutes and 10^5 minutes. For each processor time, the neutron transport was carried out for 10 trials with different random numbers to get statistically different results. This allowed for a total of 40 neutron transport runs for analog and 40 neutron transport runs for high-energy GT-CADIS. The neutron flux and the total isotope production rate were then used with CINDER to calculate the photon emission density at each processor time and each trial.

8.1 Problem Description

The geometry for this problem is the same geometry used in Chapter 7, which is shown in Figure 7.1. A simple irradiation/decay scenario was used for the activation calculation. The

photon source is calculated after a single irradiation pulse of 182 days and a decay time of 106 days.

8.2 Generation of High-energy GT-CADIS VR Parameters

In order to generate weight window lower bounds and source biasing parameters, the high-energy GT-CADIS workflow was carried out. For this workflow, the photon adjoint transport is the same as the high-energy GT-CADIS discussed in Chapter 7, which is shown in figure 7.2

$T(E_n, E_p)$ was calculated using the photon emission density generated with the irradiation schedule described in Section 8.1. Figure 8.1 shows $T(E_n)$ for several neutron energy groups. These $T(E_n)$ values are only slightly different from those shown for the toy problem in Chapter 7. In this case, $T(E_n, E_p)$ is calculated using a simpler irradiation schedule with only one irradiation time and one decay time.

The adjoint photon flux and $T(E_n, E_p)$ are used to calculate the adjoint neutron source over 83 neutron energy groups. Figure 8.2 shows the adjoint neutron source for four neutron energy groups. This adjoint neutron source is used in a deterministic calculation to obtain the adjoint neutron flux shown in Figure 8.3.

This adjoint neutron flux is used by ADVANTG 3.2 to calculate source biasing parameters and weight windows. Figure 8.4 shows the weight window lower bounds for four neutron energy groups.

8.3 Neutron Transport and SDR

In order to assess the efficacy of high-energy GT-CADIS VR parameters on the primary transport of an R2S calculation, a neutron transport was done over several processor times

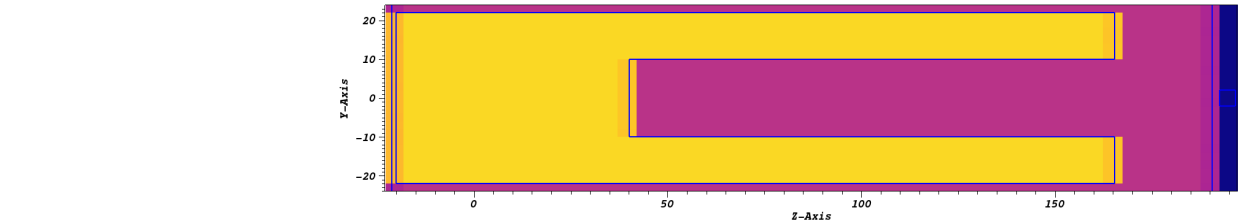

(a) Spatial distribution at $x = 0$, E_n = 3.06 - 10.7 eV

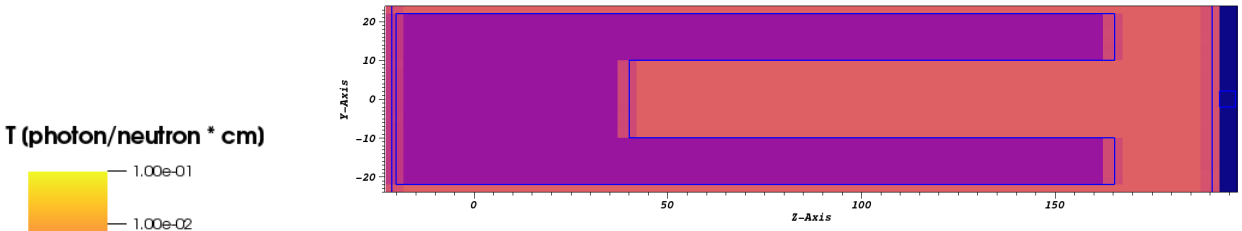

(b) Spatial distribution at $x = 0$, E_n = 8.61 - 10 MeV

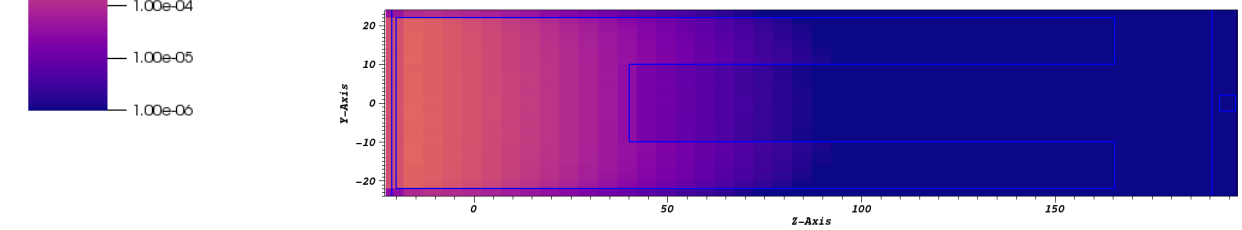

(c) Spatial distribution at $x = 0$, E_n = 80 - 100 MeV

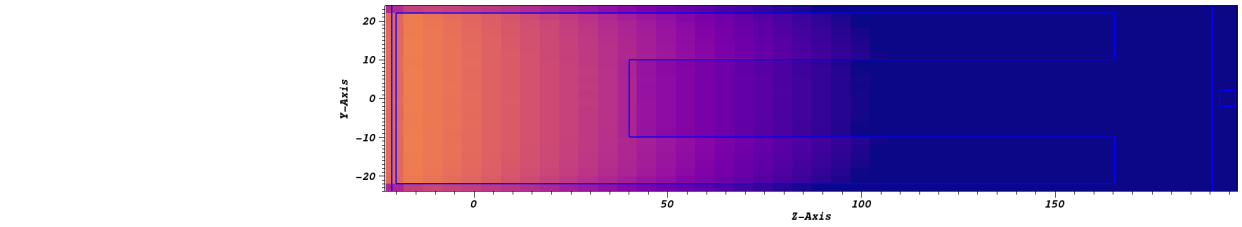

(d) Spatial distribution at $x = 0$, E_n = 950 - 1000 MeV

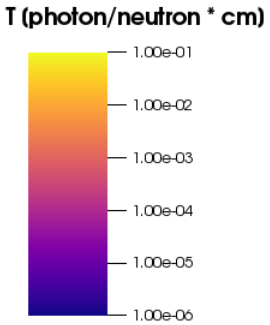

Figure 8.1: T for 182 days of irradiation and 106 days of decay

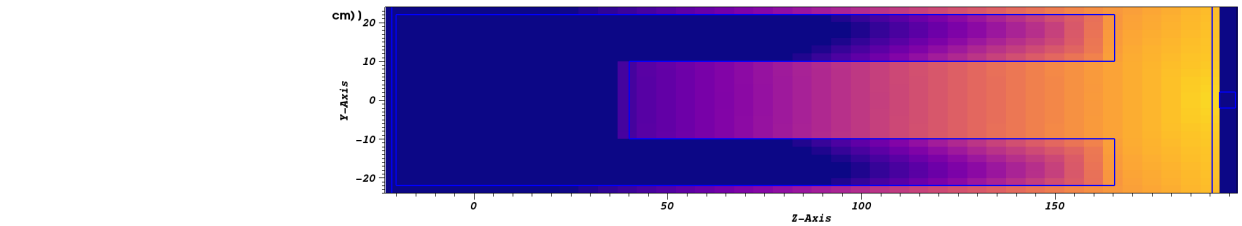

(a) Spatial distribution at $x = 0$, E_n = 3.06 - 10.7 eV

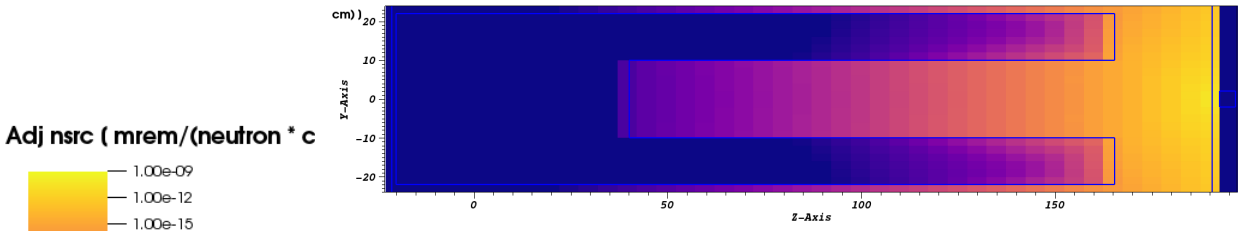

(b) Spatial distribution at $x = 0$, E_n = 8.61 - 10 MeV

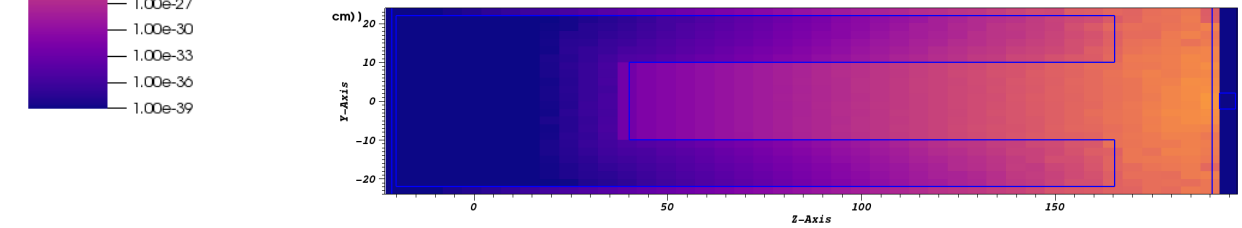

(c) Spatial distribution at $x = 0$, E_n = 80 - 100 MeV

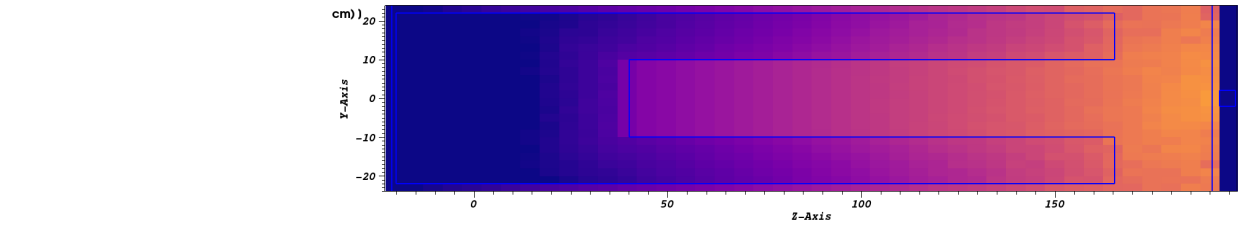

(d) Spatial distribution at $x = 0$, E_n = 950 - 1000 MeV

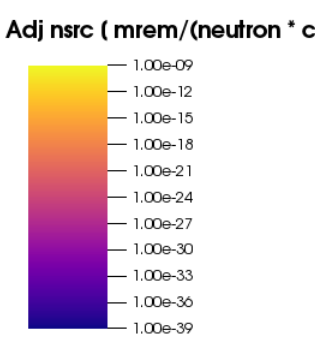

Figure 8.2: Adjoint neutron source

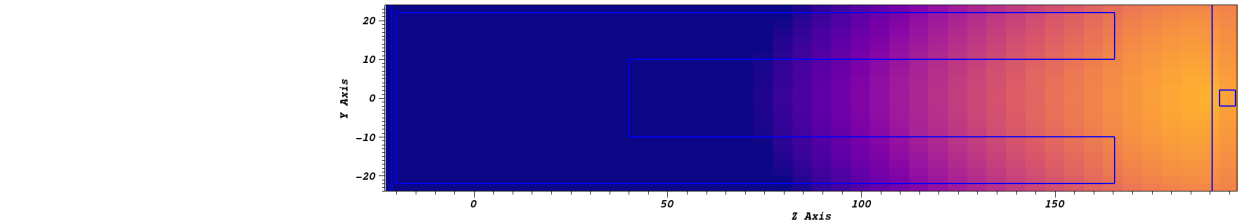

(a) Spatial distribution at $x = 0$, E_n = 3.06 - 10.7 eV

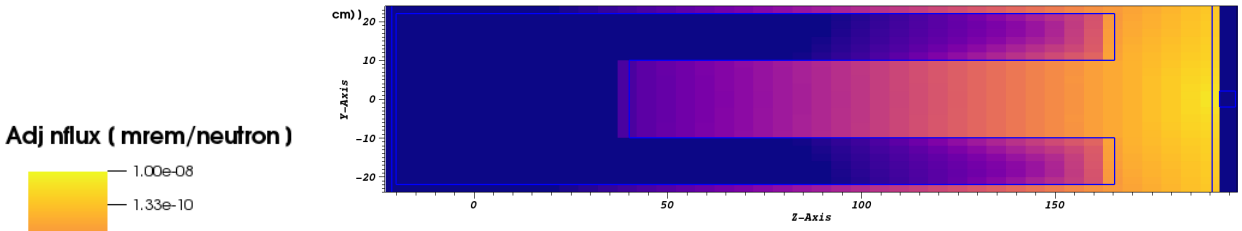

(b) Spatial distribution at $x = 0$, E_n = 8.61 - 10 MeV

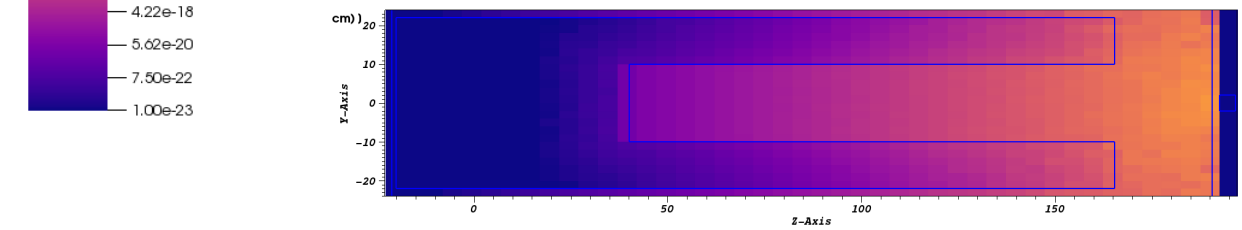

(c) Spatial distribution at $x = 0$, E_n = 80 - 100 MeV

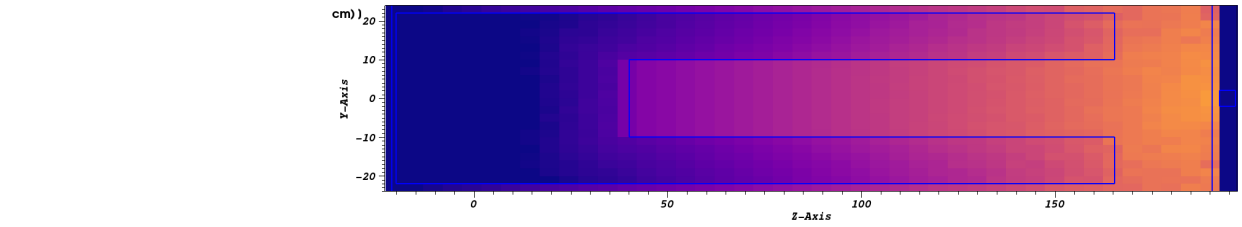

(d) Spatial distribution at $x = 0$, E_n = 950 - 1000 MeV

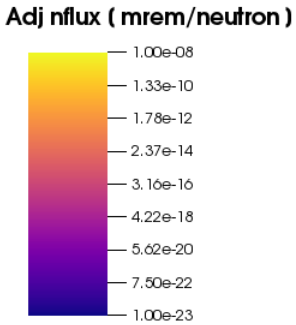

Figure 8.3: Adjoint neutron flux

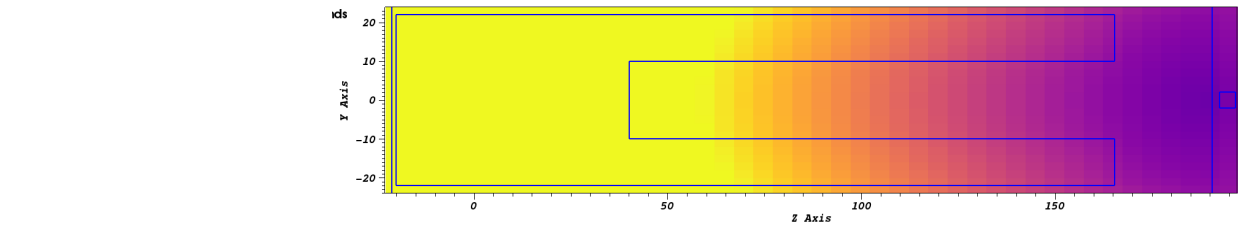

(a) Spatial distribution at $x = 0$, E_n = 3.06 - 10.7 eV

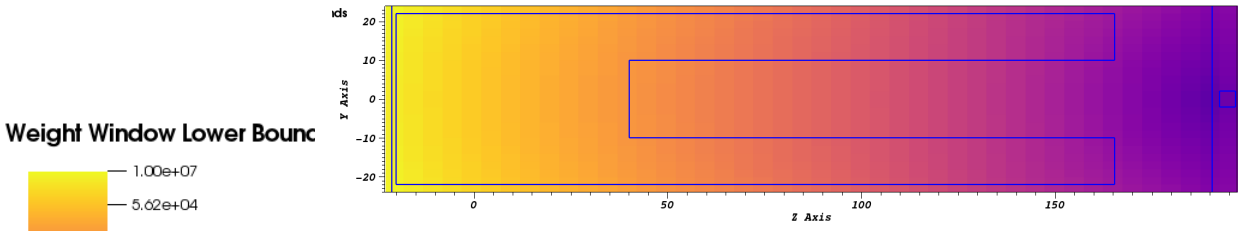

(b) Spatial distribution at $x = 0$, E_n = 8.61 - 10 MeV

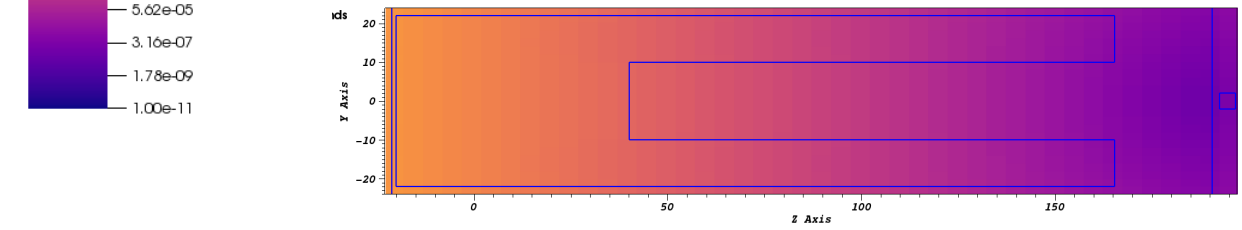

(c) Spatial distribution at $x = 0$, E_n = 80 - 100 MeV

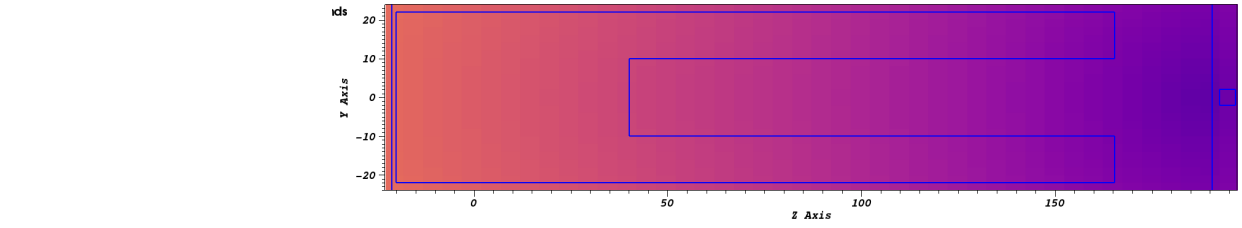

(d) Spatial distribution at $x = 0$, E_n = 950 - 1000 MeV

Figure 8.4: Weight window lower bound

for both analog and high-energy GT-CADIS methods. For this problem, four processor times were selected for this problem, ranging from 10^2 minutes to 10^5 minutes. For each processor time, ten analog and ten high-energy GT-CADIS neutron transport calculations were carried out using different random number seeds to obtain statistically independent results. The neutron flux, for neutron energies less than 25 MeV, and the net nuclide the production rate was used to calculate a photon emission density, which was used to obtain the SDR after 182 days of irradiation and 106 days of decay.

The neutron transport trials were done on identical computer hardware configurations. Each neutron transport run was run on 2 computer cluster nodes with 64 cores per node for a total of 128 MPI processes. Each neutron transport trial was run on DAG-MCNP6.2 modified to allow the use of the mesh *rnucs* tally. The processor time was estimated by specifying, in DAG-MCNP6.2, the number of particles (NPS) to be simulated rather than the processor time (CTME). The required NPS for each processor time was found by trial and error and, once found, held constant for all ten trials. This means that minor variations in processor times were observed across all trials.

The neutron flux and net nuclide production rate were obtained for each of the 80 trials (10 trials x 4 processor times x 2 methods) and used in an activation calculation with CINDER90. The activation calculation was done for an irradiation schedule of a single irradiation time of 182 days and a decay time of 106 days. The photon source distribution was obtained for each of the 80 trials and used to obtain the SDR at the detector in the back of geometry 7.1. The photon source distribution can be used in a MC photon transport to obtain the SDR at the detector. This method leads to the SDR results with statistical error from the photon transport. In order to avoid this statistical error, the SDR was calculated using Equation 2.33. The adjoint photon flux shown in Figure 7.2 was used along with the photon source distribution. The resulting SDR only has the error from the MC neutron transport and from the discretization of the deterministic adjoint transport. Because the same adjoint photon flux is used for all 80 trials, the neutron flux is the only quantity that

contributes to differences in the convergence rate.

8.4 Results

The relative error of the neutron flux for each of the two methods is shown in Figure 8.5. Figure 8.5 shows one trial for each processor time. For the analog trials, Figure 8.5 shows that the mesh volume elements at the back of the geometry do not have any tally scores. The region with tally scores propagates toward the detector as the processor time is increased. The undersampling of this region leads to an underestimation of the SDR at the detector. This is seen in the final SDR of the test problem in Chapter 7. In Table 7.4, the SDR at the detector is greatly underestimated due to a lack of tally scores at the back of the geometry during neutron transport.

For the neutron transport with high-energy GT-CADIS VR, all the mesh volume elements have tally scores even at the lowest processor time. Using high-energy GT-CADIS VR parameters leads to a decrease in the statistical uncertainty in the neutron flux, particularly at the back of the geometry. This is favorable as the adjoint neutron source shown in Figure 8.2 shows that the important neutrons for the SDR are the ones at the back of the geometry closest to the detector.

Figure 8.6 shows the SDR for each of the 80 trials. This figure shows that the SDR calculated with analog neutron transport is underestimated by all trials at short processor times and under or over-estimated at larger processor times. The underestimation of the SDR is consistent with the lack of tally scores in the back of the geometry, as seen in Figure 8.5. As the processor time increases, the SDR from the analog neutron transport has a larger spread. These results are not fully converged as there is still a significant spread among results at the largest processor time. Figure 8.6 also shows that the SDR calculated with high-energy GT-CADIS converges a lot sooner, and most results are within a few standard deviations from the converged number. This is further shown in Figure 8.7, which shows the

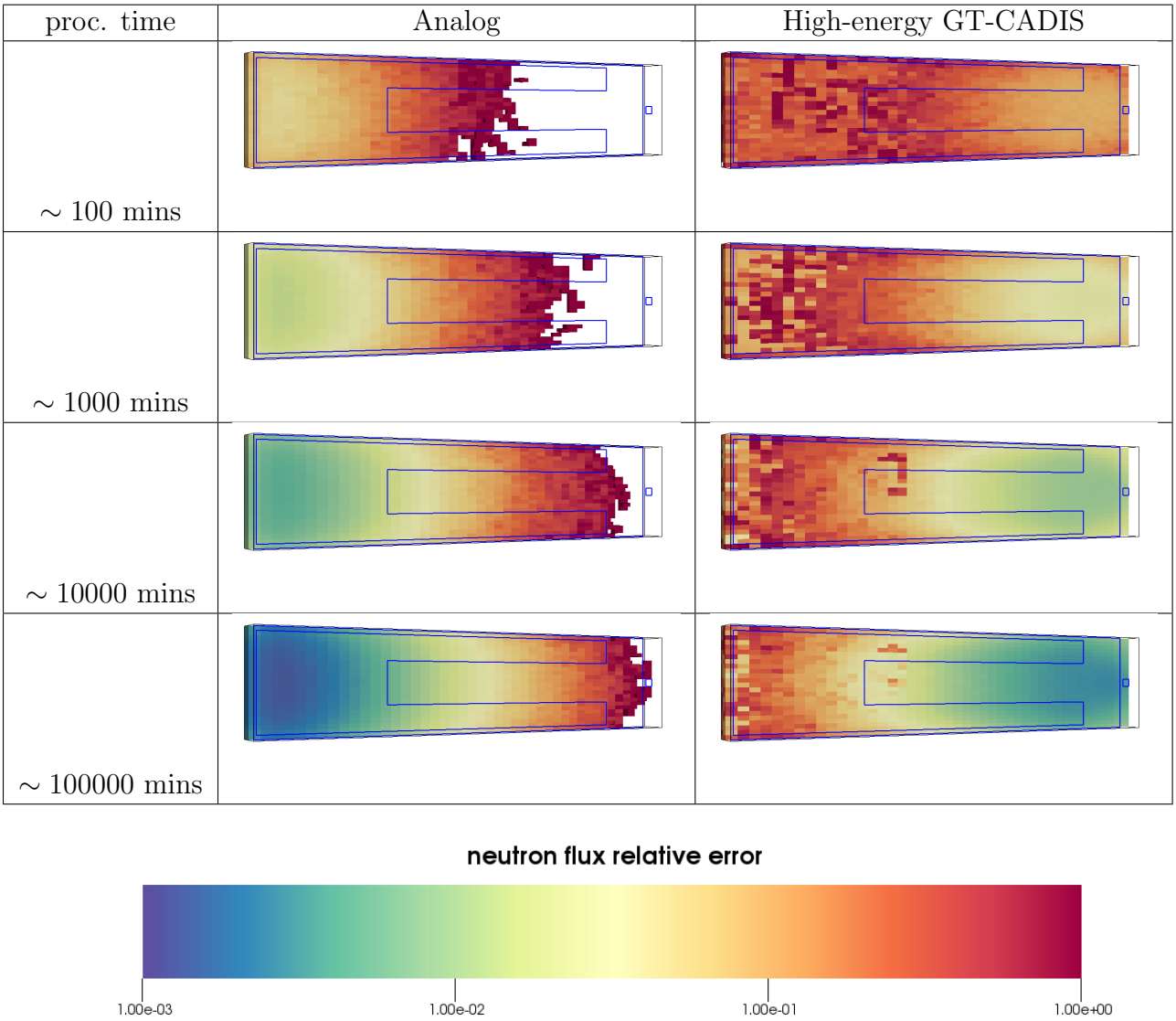

Figure 8.5: Relative error in the neutron flux

mean SDR for each of the four processor times and the standard deviation of the SDR and the standard deviation of the processor time.

To further quantify the efficacy of the high-energy GT-CADIS method, the FOM was calculated for each processor time and for each method. The FOM was calculated using Equation 2.12, the processor time, and the relative error in the flux. The uncertainty in processor time was also propagated to obtain the error in the FOM. The FOM for the analog neutron transport ranges from $1.278 \pm 0.003 \cdot 10^{-3}$ to $1.632 \pm 0.014 \cdot 10^{-5}$. The FOM

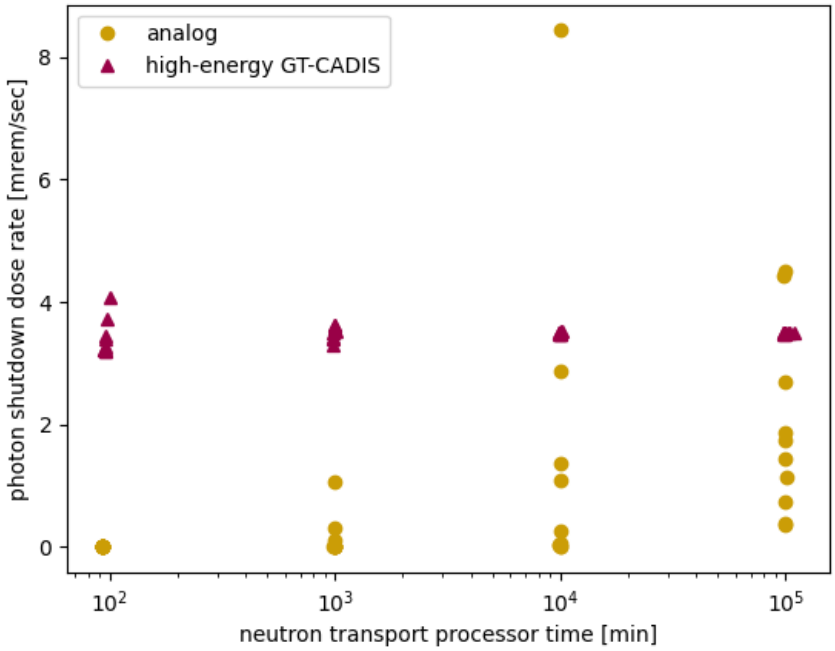

Figure 8.6: Photon SDR results over computer processor time

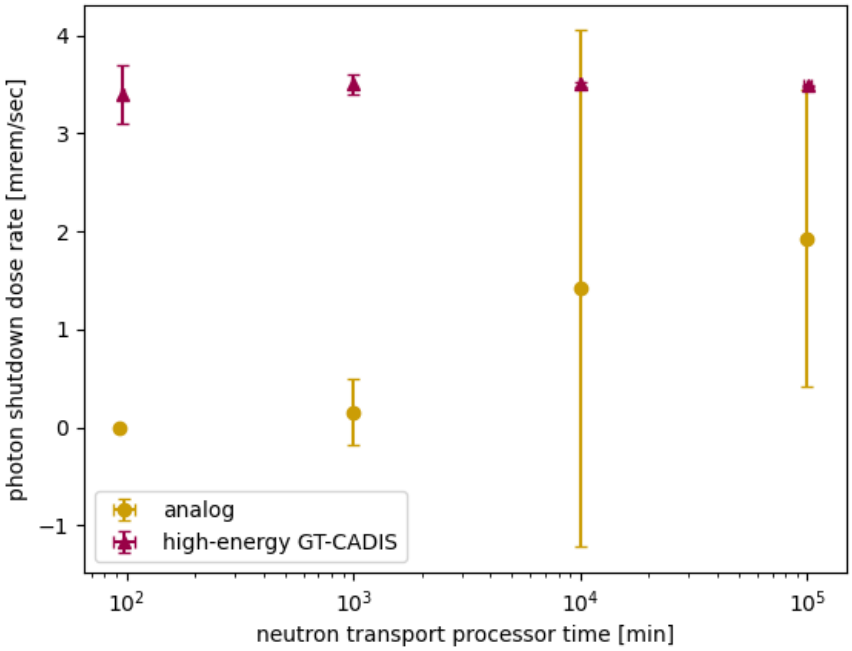

Figure 8.7: Average photon SDR results from figure 8.6

Table 8.1: Neutron transport FOM for each processor time

Time [mins]	FOM - analog	FOM HE GT-CADIS	FOM ratio [HE GT-CADIS/ analog]
100	$1.278 \pm 0.003 \cdot 10^{-3}$	1.424 ± 0.026	$4.297 \pm 0.080 \cdot 10^{5}$
1000	$2.068 \pm 0.006 \cdot 10^{-4}$	1.152 ± 0.014	$1.880 \pm 0.024 \cdot 10^{6}$
10000	$2.892 \pm 0.023 \cdot 10^{-5}$	4.474 ± 0.037	$1.979 \pm 0.023 \cdot 10^{7}$
100000	$1.632 \pm 0.014 \cdot 10^{-5}$	2.797 ± 0.109	$1.983 \pm 0.079 \cdot 10^{7}$

for the high-energy GT-CADIS ranges from 1.152 ± 0.014 to 4.474 ± 0.037. For each processor time, the FOM for analog high-energy GT-CADIS, as well as the ratio between the two, are shown in Table 8.1. The speed up for the high-energy GT-CADIS compared to the analog for the highest processor time is $1.983 \pm 0.079 \cdot 10^{7}$.

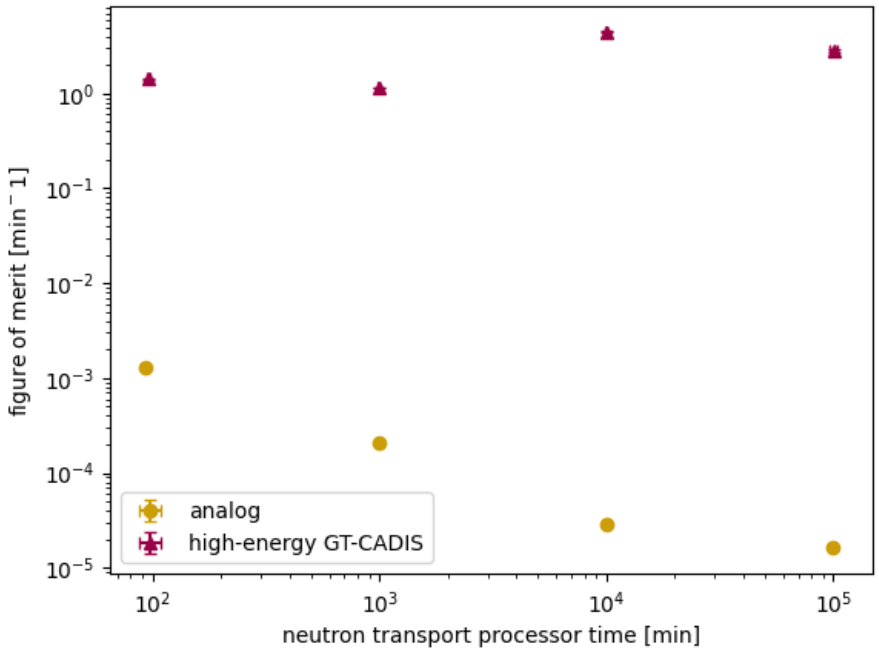

Figure 8.8: Figure of merit over neutron transport processor time

8.5 Conclusion

In this chapter, a simple problem was used to quantify the performance of the high-energy GT-CADIS compared to the analog neutron transport. The VR parameters constructed

with high-energy GT-CADIS result in faster convergence of the neutron flux in important regions. This is shown by the decrease of statistical uncertainty in the flux compared to the analog results. The SDR was calculated using these neutron fluxes for several trials in order to obtain a SDR standard deviation to be used in the calculation of the FOM. When comparing the FOM of analog transport to high-energy GT-CADIS transport, the speed up can be 10^7 times faster. This suggests that the application of high-energy GT-CADIS VR parameters is beneficial to these types of problems and can result in a significantly faster calculation of SDR in accelerator-driven systems.

Chapter 9

Full Production

In this chapter, the high-energy GT-CADIS will be used to optimize the primary transport of the R2S calculation to obtain the SDR at several detectors for a realistic full production model. The choice of SNS as the full production problem is made in order to compare to experimental results and the numerical results discussed in Chapter 3. The VR parameters are generated to optimize the neutron transport for the calculation of SDR at several detectors.

9.1 Geometry Description

The full production geometry chosen for this problem is the SNS system shown in Figure 9.1. One key characteristic of this geometry is the target assembly, which consists of a steel volume with mercury channels inside. In this problem, the target assembly will be removed, and the mercury drained after an irradiation schedule shown in Table 3.1. After 106 days, detectors are placed around the target geometry to measure the SDR at several detectors. Figure 9.2 shows the target assembly and detectors positioned around the target. This is a direct comparison to the full demonstration problem discussed in Chapter 3.

9.2 Generation of Neutron Source

Using ADVANTG for implementing the high-energy GT-CADIS has a few limitations. Two limitations are particularly relevant in this work. The first is a limitation in DENOVO, which is used for deterministic calculations. Denovo is limited to fixed-source neutron, photon, or neutron-photon coupled calculations [26]. The source for the SNS problem is a 1 GeV proton

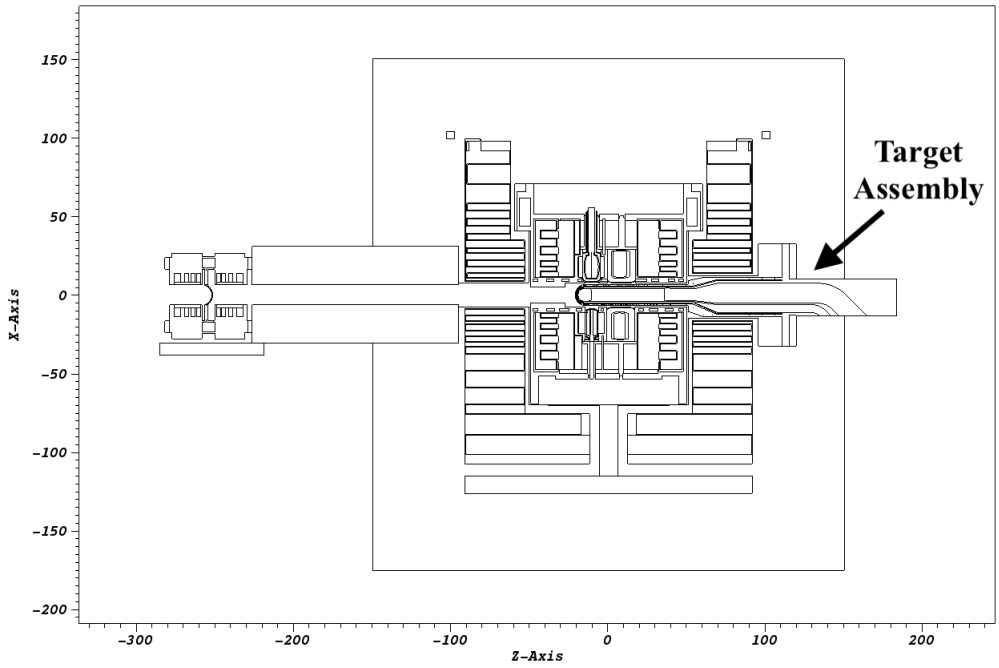

Figure 9.1: Cross-sectional view of SNS geometry at y=0

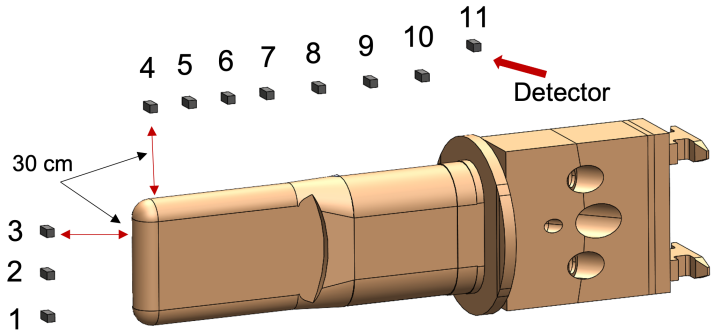

Figure 9.2: Detectors as positioned around the out-of-service target for SDR measurements

source. An extra transport step is needed to obtain a neutron source approximation from the original proton source. The second limitation is related to the geometry. ADVANTG uses MCNP5, which is limited to native MCNP geometry definitions. In order to calculate the neutron source from the proton source, an MCNP geometry with around 200 volumes in the target area is used.

An MCNP6.2 transport run was performed with 10^6 particles, and only neutron and

proton transport turned on. A *ptrac* file was obtained with position, energy, and weight information in the volumes of the target area. This *ptrac* file was processed to extract information from neutron particles that were born from a source proton and from a proton born from a source proton. The information collected was for 13.4×10^6 neutron particles, which gives an average of 13 neutrons born per source proton particle.

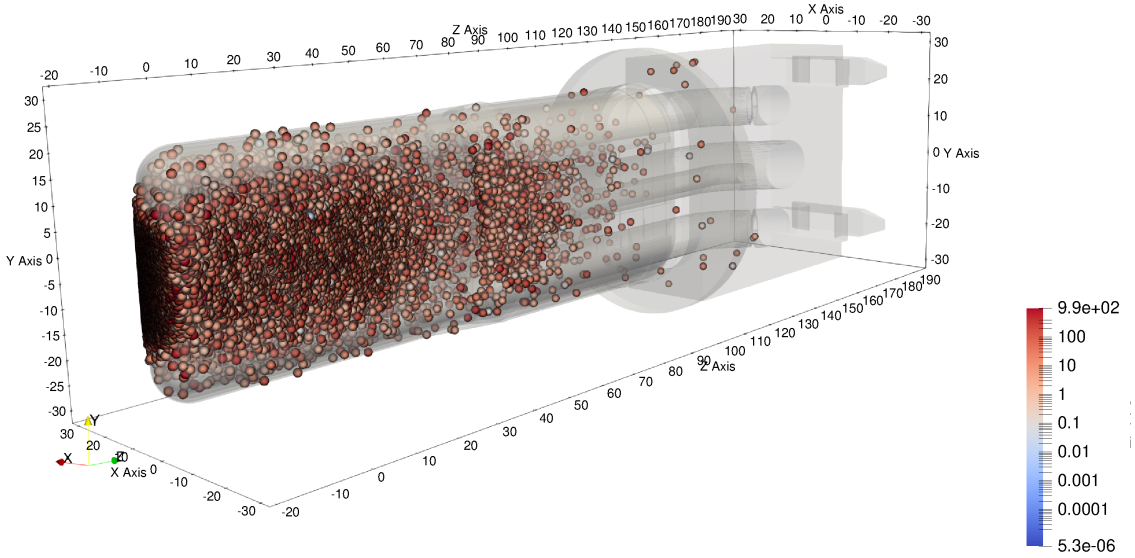

Figure 9.3: Neutrons born from source particles

Figure 9.3 shows the 13.4×10^6 neutron particles born in the target region. It also shows the distribution of energy at which the neutron was born. The energy distribution is better shown in Figure 9.4. These figures show that the neutron energy ranges from as low as 1 eV to 10^3 MeV. Figure 9.4c shows that in the z-direction, the generation of neutrons becomes less dense around 40 cm and after 80 cm. This is consistent with the fact that the mercury channels become smaller between $z = 40 - 80$ cm. It also shows that low-energy neutrons are generated at the front of the geometry, but not many make it past 40 cm, and only a few make high-energy neutrons get transported to the back of the geometry. In the x-direction, the neutrons are uniformly generated between -5 cm and 5 cm. The number of neutrons generated lessens outside this range, which is expected because the target is only defined between $z = 90 - 180$. In the y-direction, the generation of neutrons is mostly uniform, with

the lowest and highest neutron energy generated in the center of the geometry. This is likely due to the proton source definition of the proton source in the y-direction.

The information of each of these 13.4×10^6 neutron particles was used to create a cell-based neutron source. The source was created with 83 neutron energy group distribution and cell rejection for spatial distribution. This cell-based neutron source was then used in the high-energy GT-CADIS workflow to calculate the VR parameters.

9.3 Generation of VR Parameters

One set of VR parameters was generated to optimize for the SDR 106 days after shutdown. The high-energy GT-CADIS used a photon flux mesh tally with SNS specific flux-to-dose conversion factors [24] as the adjoint photon source. The tally starts above the target geometry and extends over all detectors 30 cm away from the target. The tally extends from x= -1 cm to 1 cm, y= 55 cm to 75 cm, and z= -5 cm to 140 cm. The adjoint photon transport used a mesh of 4930 mesh volume elements.

Figure 9.5a shows the adjoint photon flux for the photon energy group between $14 - 20$ MeV. Figure 9.5b shows the adjoint photon flux over all of the photon energies. These figures show that the important photons for the SDR at the detectors are those closest to the detectors and those in the first three-quarters of the geometry.

$T(E_n, E_p)$ was calculated using the neutron flux from Chapter 6 shown in Figure 6.2. The photon emission density needed for $T(E_n, E_p)$ was calculated with the neutron flux shown in 6.2 for neutrons below 25 MeV and with the net radionuclide production from an MCNP preliminary run. Figure 9.6 shows $T(E_n, E_{p,total})$, which has been summed over all of the photon energies. Figure 9.6a shows $T(E_n, E_{p,total})$ for neutron energy group $19.6 - 25$ MeV, and 9.6a shows $T(E_n, E_{p,total})$ for neutron energy group $25 - 30$ MeV. These $T(E_n, E_{p,total})$ plots show that more photons are generated per neutrons of energy $19.6 - 25$ MeV than for neutrons of energy $25 - 30$ MeV.

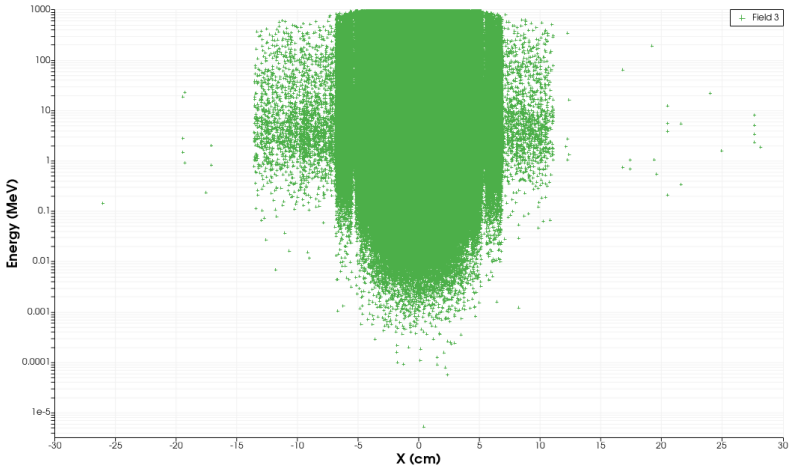

(a) Neutron energy along the x-direction

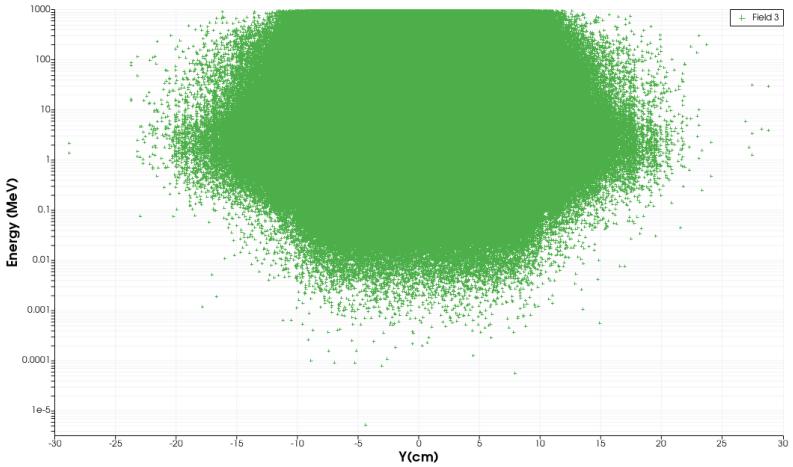

(b) Neutron energy along the y-direction

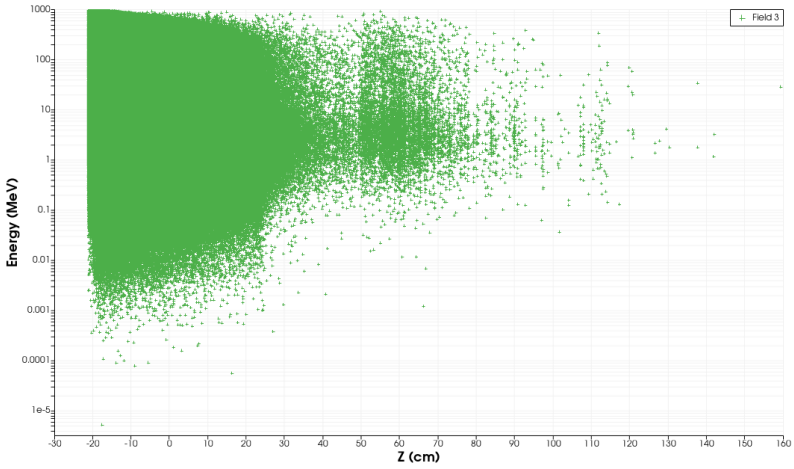

(c) Neutron energy along the z-direction

Figure 9.4: Neutron energy along each axis

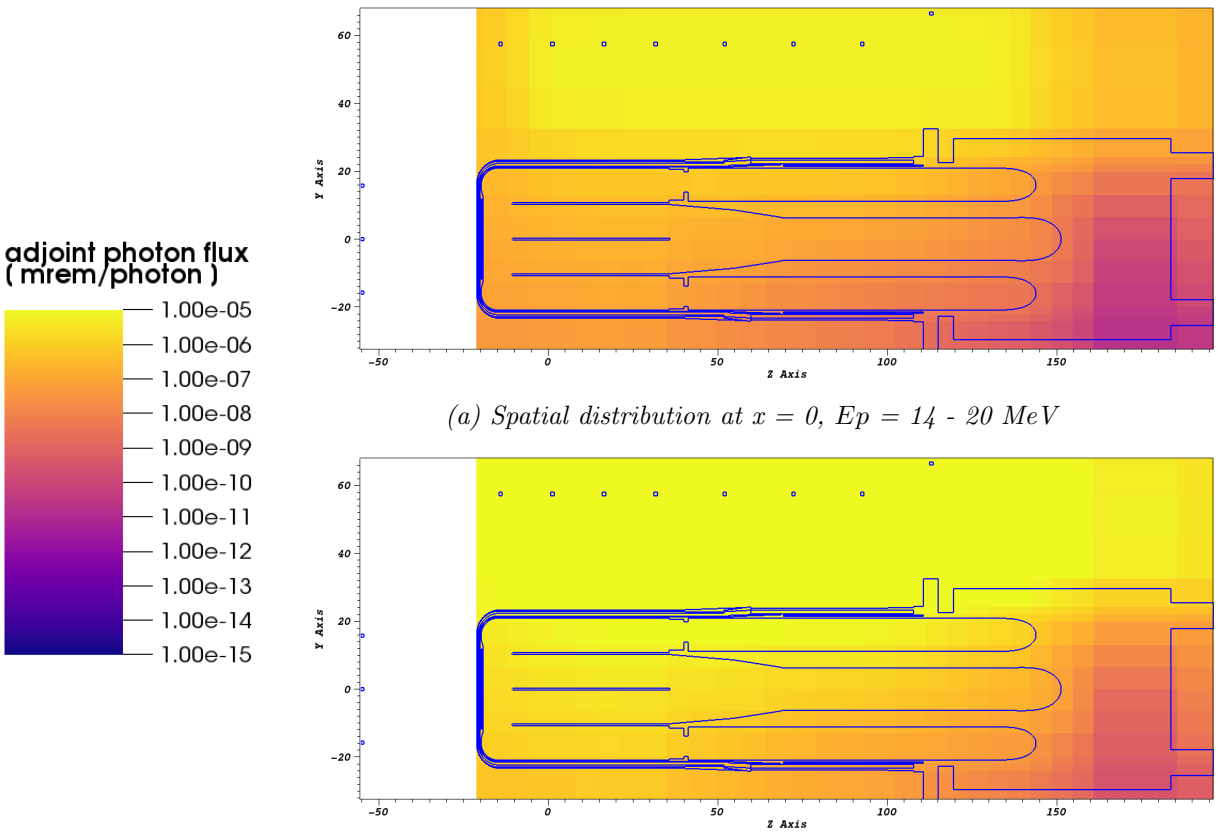

(a) Spatial distribution at $x = 0$, Ep = 14 - 20 MeV

(b) Spatial distribution at $x = 0$, E_p = total

Figure 9.5: Adjoint photon flux distribution

The adjoint photon flux was used alongside $T(E_n, E_p)$ to calculate the adjoint neutron source. Figures 9.7a - 9.7c show the total adjoint neutron source and the adjoint neutron source for $19.6 - 25$ MeV and $25 - 30$ MeV. The adjoint neutron source figures show that neutrons between $19.6 - 25$ MeV dominate the important neutrons that generate photons that are important to the SDR at the detectors. This is expected as there are more photons per neutron being generated in the $19.6 - 25$ MeV region, as shown in Figure 9.6a.

A deterministic adjoint neutron transport was performed with ADVANTG and the adjoint neutron source shown in Figure 9.7. Figure 9.8 shows the adjoint neutron flux. Figures 9.8a and 9.8b show the adjoint neutron flux for neutron groups $19.6 - 25$ MeV and $25 - 30$ MeV, respectively. In these two figures, the adjoint neutron flux is slightly higher in the top second and third quarters of the geometry. This is further shown in Figure 9.7c, which

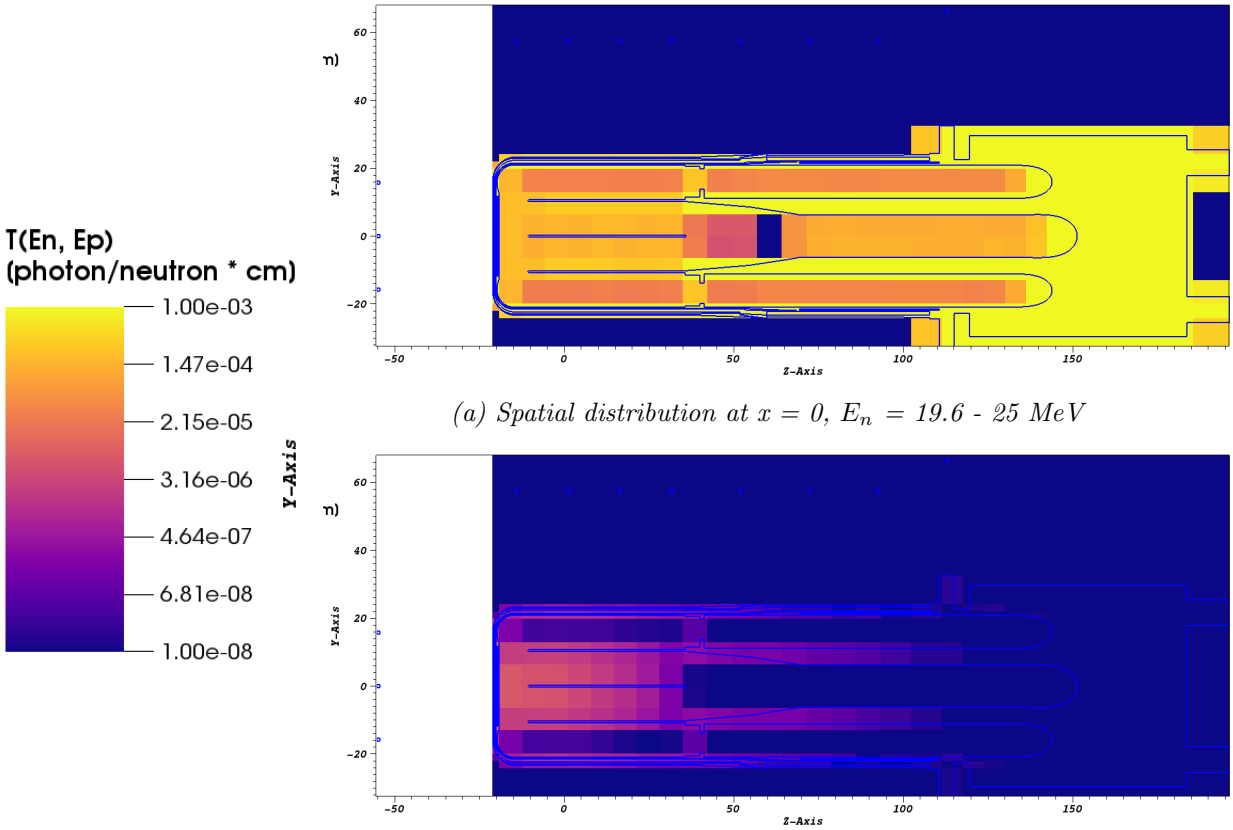

(a) Spatial distribution at $x = 0$, E_n = 19.6 - 25 MeV

(b) Spatial distribution at $x = 0$, E_n = 25 - 30 MeV

Figure 9.6: T distribution with activation after 106 days decay

shows a similar trend with the highest adjoint neutron flux in the middle top area.

The adjoint neutron flux was used in an ADVANTG CADIS run to obtain weight window lower bounds and biased source parameters. Figure 9.9 shows the weight window lower bounds for two neutron energy groups, $19.6 - 25$ MeV and $25 - 30$ MeV. Both figures show smaller weight window lower bounds at the top middle section of the geometry, signifying a region of more importance. This is expected as the adjoint neutron source shows those same regions as the important regions for the SDR at the detectors.

The high-energy GT-CADIS workflow also generated source biasing (SB) parameters for spatial probabilities in each volumetric cell and source biasing parameters for the energy probabilities. The ratio between the spatial unbiased source probability (SP) and spatial biased source probability is shown in Figure 9.10 for each volumetric cell. This figure repre-

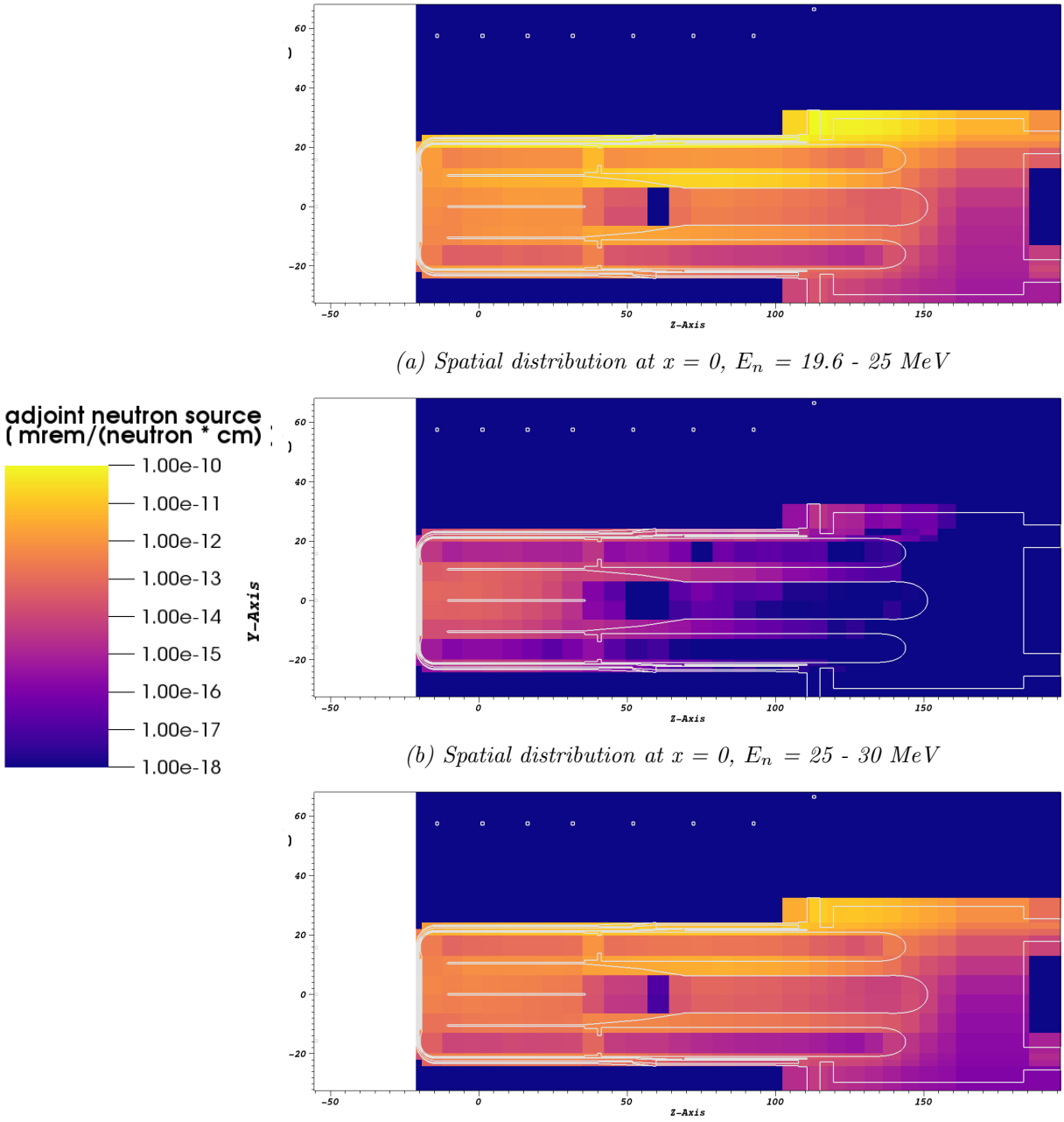

(a) Spatial distribution at $x = 0$, E_n = 19.6 - 25 MeV

(b) Spatial distribution at $x = 0$, E_n = 25 - 30 MeV

(c) Spatial distribution at $x = 0$, E_n = total

Figure 9.7: Adjoint neutron source

sents which volumetric cells are more or less important to the detector response compared to the original, unbiased source. A ratio greater than one signifies a less important volumetric cell and a ratio less than one signifies a more important volumetric cell. The ratios vary between 0.1 and 5 for all volumetric cells, indicating that volumetric cells are only about 10

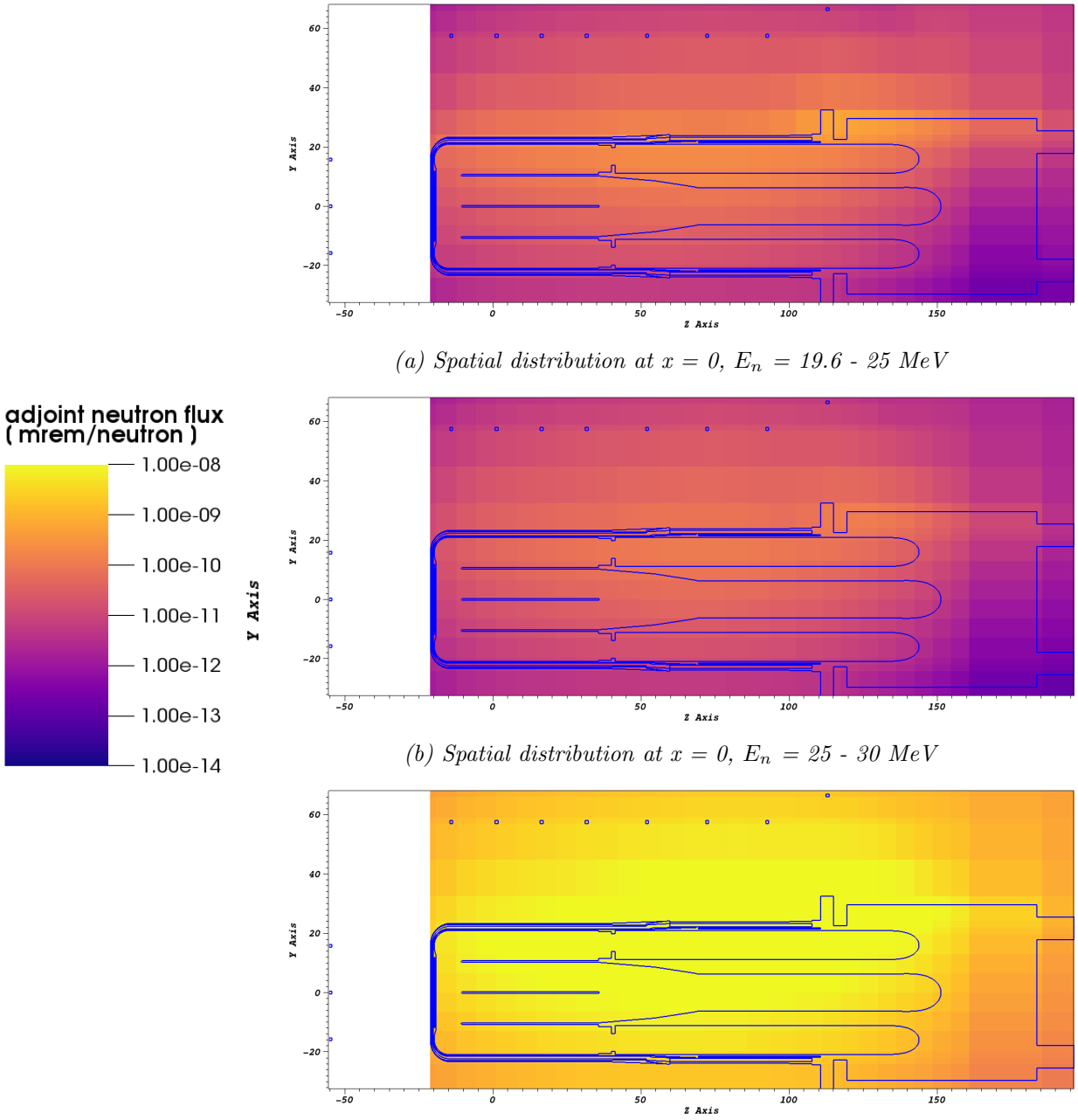

(a) Spatial distribution at $x = 0$, E_n = 19.6 - 25 MeV

(b) Spatial distribution at $x = 0$, E_n = 25 - 30 MeV

(c) Spatial distribution at $x = 0$, E_n = total

Figure 9.8: Adjoint neutron flux

times more important at most and 5 times less important.

Figure 9.11 shows the ratio of source unbiased probability to source biased probability for each cell and neutron energy group. Each color in this plot represents one of the approximately 200 volumetric cells used to define the source. This plot indicates that lower-energy

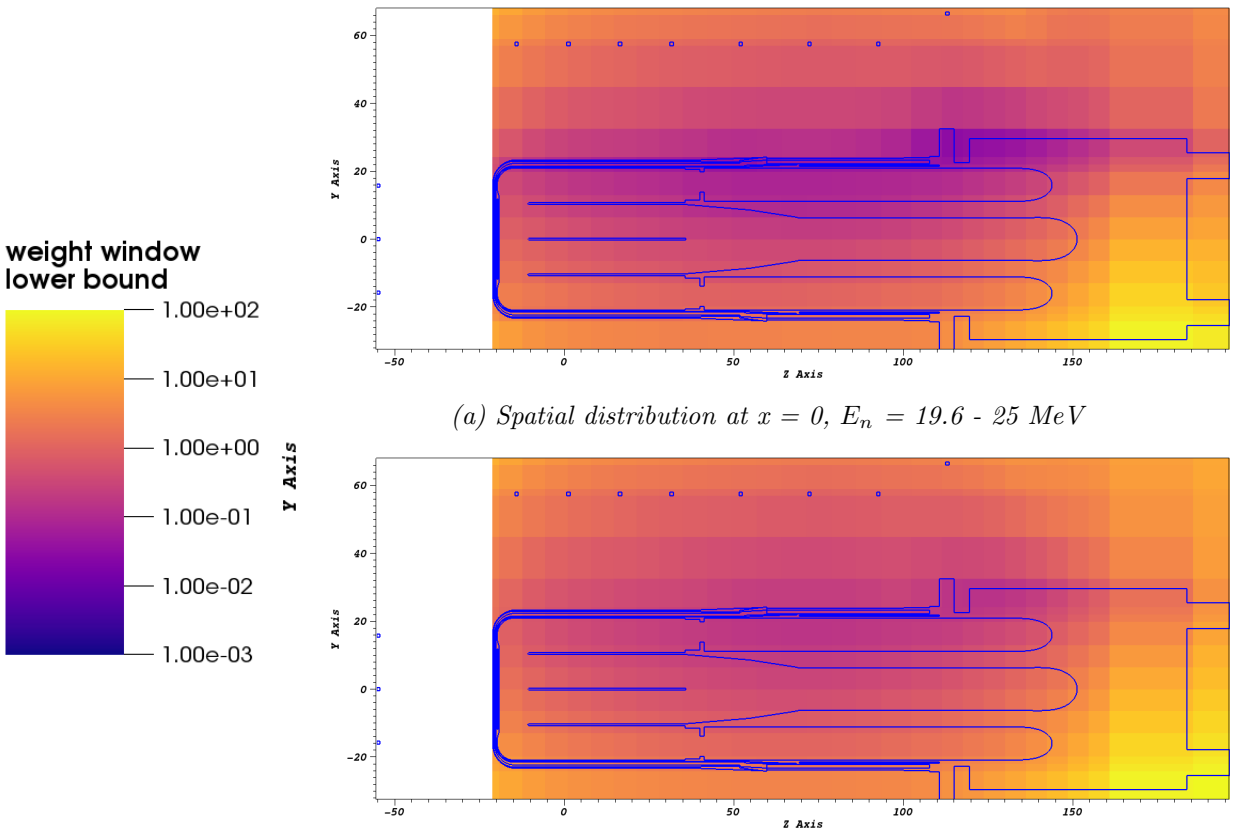

(a) Spatial distribution at $x = 0$, E_n = 19.6 - 25 MeV

(b) Spatial distribution at $x = 0$, E_n = 25 - 30 MeV

Figure 9.9: Neutron weight window lower bounds

neutrons are less important to the detector response than those described in the true, unbiased source. In contrast, higher-energy neutrons become more important to the detector response. The ratios in this plot are between 0.07 and 5, which means neutrons are at most 5 times less important and 14 more important.

9.4 Shutdown Dose Rate

Multiple R2S calculations were performed for the full SNS geometry to obtain the SDR at the detectors. The neutron transport was first set up with the neutron source created in 9.2, and the neutron weight windows and biased source parameters calculated in 9.2 were used.

The second neutron transport was set up with the original SNS 1 GeV proton source. In this case, the neutron transport was run with only the weight window lower bounds since

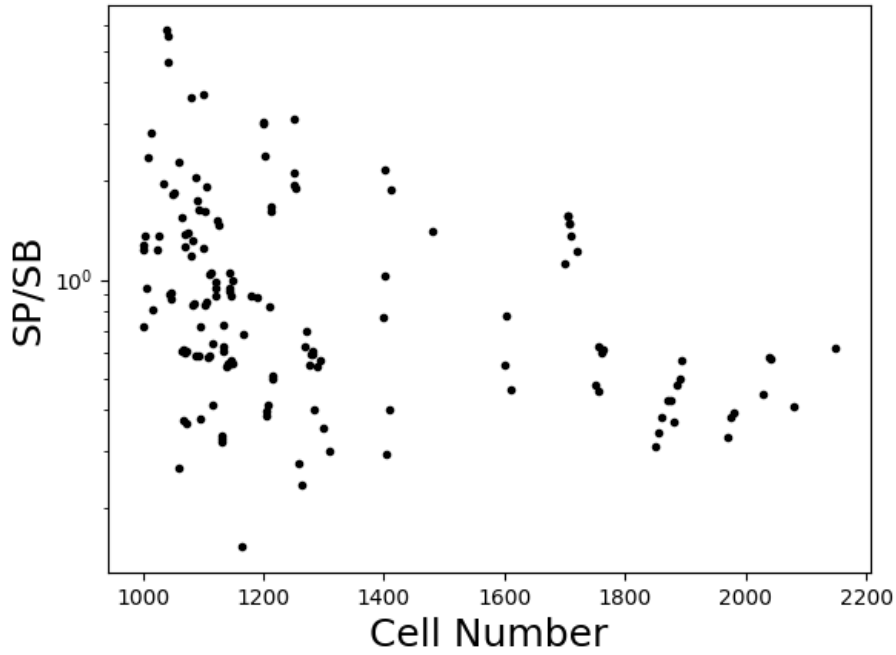

Figure 9.10: Ratio of unbiased source probability over biased probability per cell

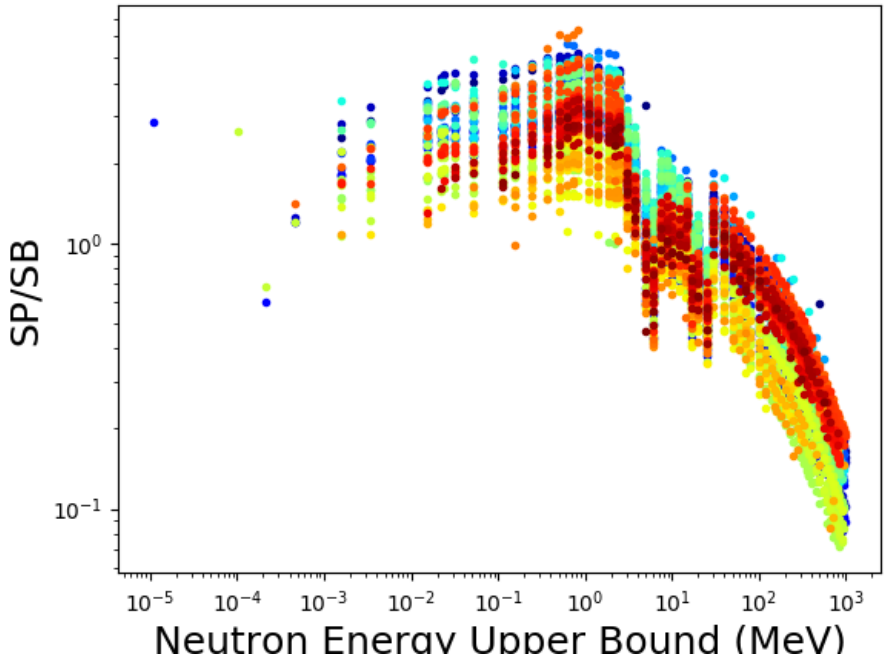

Figure 9.11: Ratio of unbiased source probability over biased probability per neutron energy per cell

the biasing parameters are generated for a neutron source and not applicable to the proton source. Three parameters informed the choice to run the neutron transport with the weight window parameters only with the original proton source: the original unbiased neutron source probability, the ratio between the biased and unbiased neutron source probabilities, and the weights of the neutrons born from protons.

Figure 9.12 shows the ratio between the unbiased and biased source probability against the unbiased source probability. This figure shows that the ratio between the biased and unbiased probabilities is between 7×10^{-1} and 6. This means that most neutrons are at most five times less important to the SDR or 14 times more important. It also shows that the more extreme cases, depicted by really low ratios, are mostly concentrated at low source probability. This is important because if the source biasing is not used to ensure that neutrons are born within the appropriate weight, then the ones more likely to split will happen with less frequency as they have a lower probability of being born. Figure 9.13 shows the weights of neutrons born from source protons. This figure shows that all neutrons born from source protons are born with a weight of 1. The neutrons being born with the same weight as the original source particles allows us to infer that using the original proton source will generate neutrons with appropriate weights to avoid over-splitting or particle termination due to inconsistencies in particle weight.

An MCNP neutron transport was performed with four different configurations:

1. Analog with neutron source and MCNP geometry
2. Analog with proton source and CAD geometry
3. High-energy GT-CADIS with neutron source and MCNP geometry
4. High-energy GT-CADIS with proton source, no source biasing and CAD geometry

Figure 9.14 shows the neutron flux for neutrons of energies up to 25 MeV for all four configurations. These plots show some differences in the relative error of the neutron flux. For

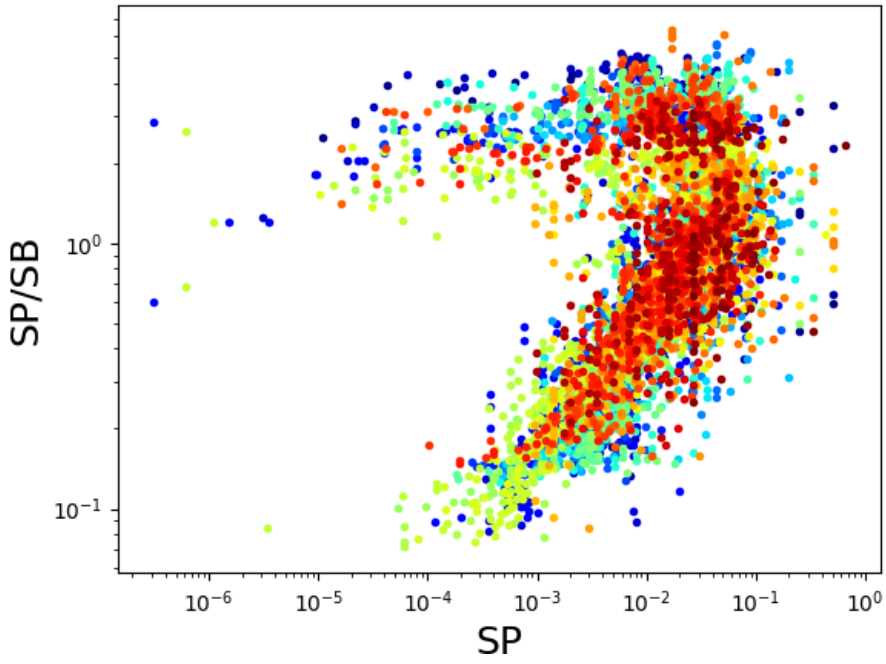

Figure 9.12: Ratio of unbiased source probability over unbiased probability per neutron energy per cell

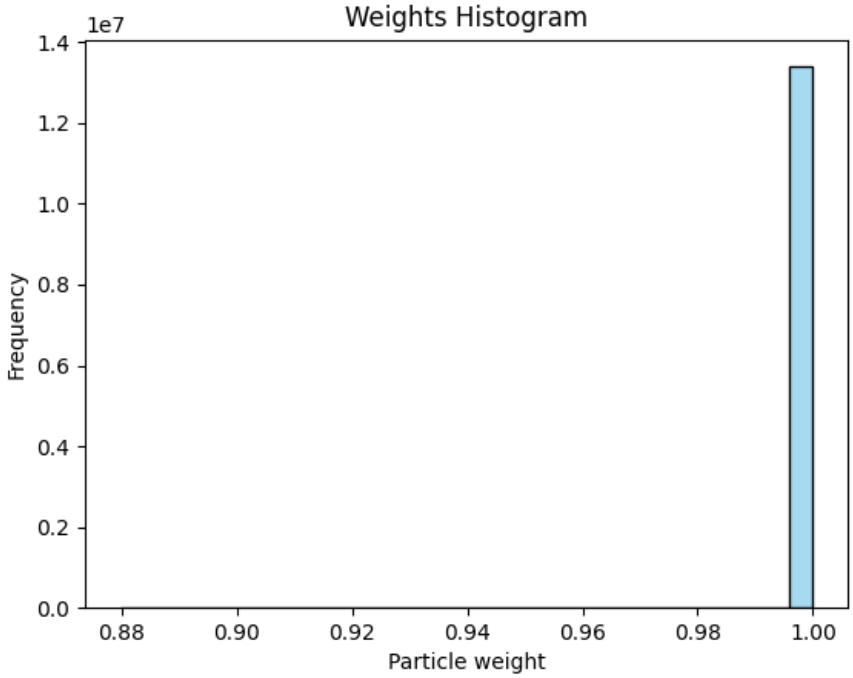

Figure 9.13: Neutron particle weight

the transport with neutron source and biasing parameters, the graphs show that the relative error is slightly better at the top of the target geometry. At the back of the geometry, the neutron flux is not as important to the SDR at the detectors, so the neutron flux relative error is greater, and less time is spent transporting neutrons in this region. For the transport with a proton source and no biasing parameters, the graphs show only a slight decrease in the relative error in the top three-quarters of the geometry. It also shows that the error at the back of the geometry is greater with VR than for the analog transport.

Figure 9.15 shows the neutron flux and statistical uncertainty for neutrons of energies above 25 MeV for all four configurations. These plots show greater differences in the relative error between the analog run and the high-energy GT-CADIS run. In the transport calculation with a neutron source, the relative error is significantly improved at the top three-quarters of the geometry. A similar trend is seen in proton source transport. The reduction of the statistical uncertainty in the neutron flux at these specific locations is important because the adjoint neutron source shown in Figure 9.7c shows that the most important neutrons for the SDR at the detector are in those same regions.

The FOM for the neutron transport was calculated using the relative error and the processor time for the analog with a proton source run and the high-energy GT-CADIS with a proton source run. Figure 9.16 shows the FOM for two neutron flux energy groups and for the total neutron flux. These figures show an increase of FOM in important regions of up to 25 times that of the analog transport.

The neutron flux and production rates are then used in an activation calculation to generate photon emission density, which is then post-processed to generate a mesh photon source. The photon source is used in a photon transport calculation to obtain the SDR at two tallies covering all detectors and the SDR at each detector shown in Figure 9.2. Figure 9.17 shows the photon dose rates at two tallies for all four configurations. It is important to note that the statistical uncertainty shown in these plots only considers the error in the photon transport and not the error in the photon source from the neutron transport.

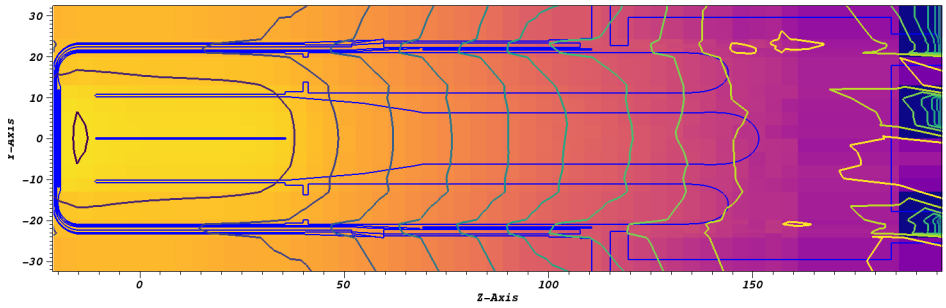

(a) Analog - neutron source

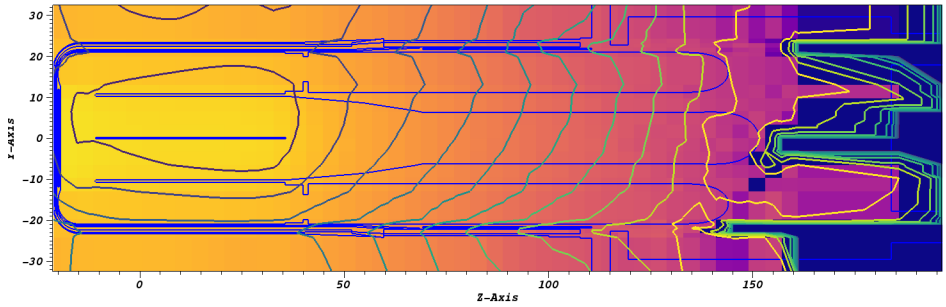

(b) High-energy GT-CADIS - neutron source

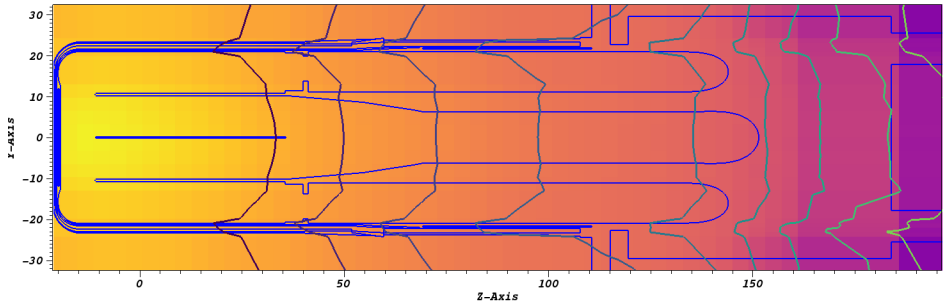

(c) Analog - proton source

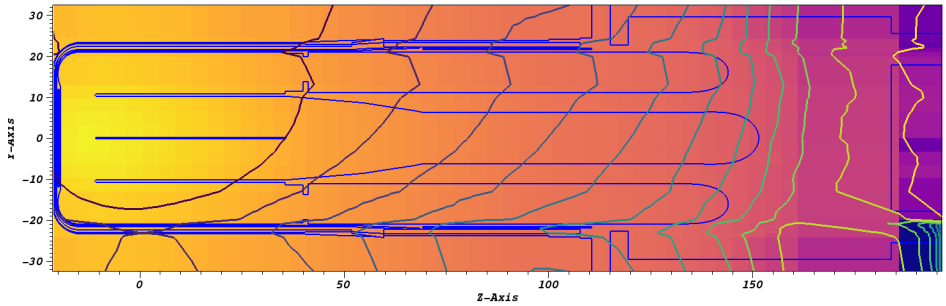

(d) High-energy GT-CADIS - proton source

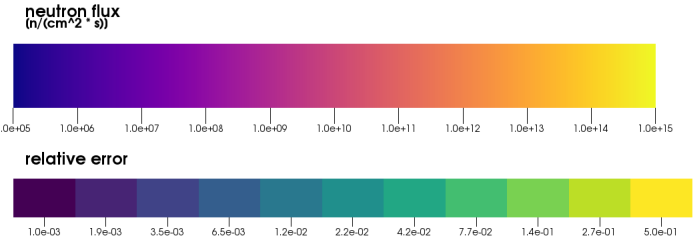

Figure 9.14: Neutron flux distribution and corresponding relative error at $x = 0$, $E_n = 0$ - 25 MeV

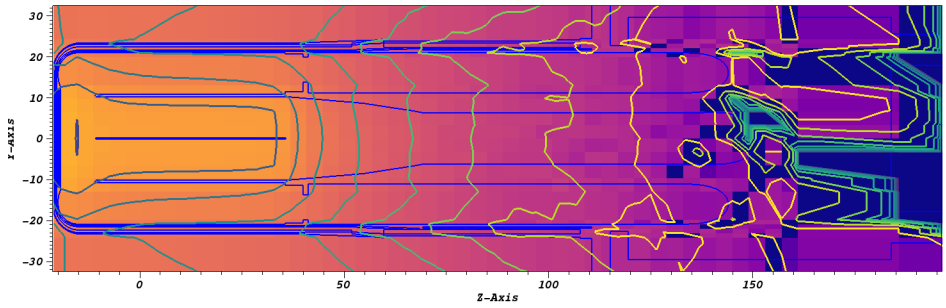

(a) Analog - neutron source

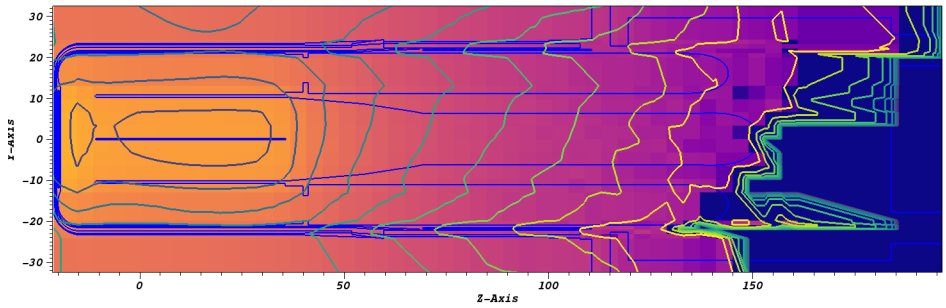

(b) High-energy GT-CADIS - neutron source

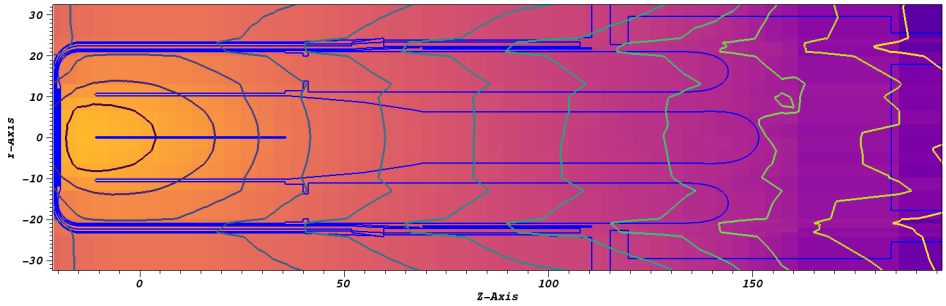

(c) Analog - proton source

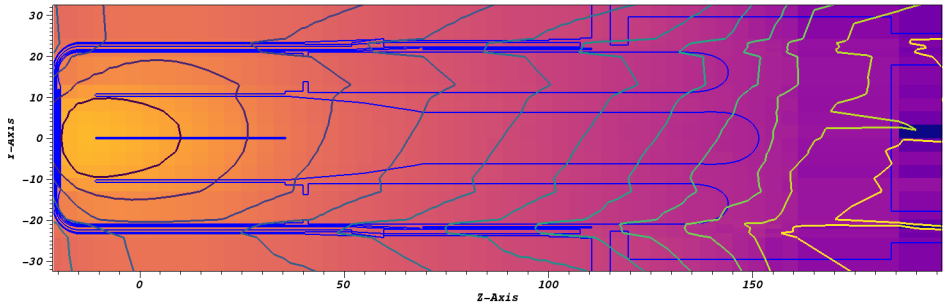

(d) High-energy GT-CADIS - proton source

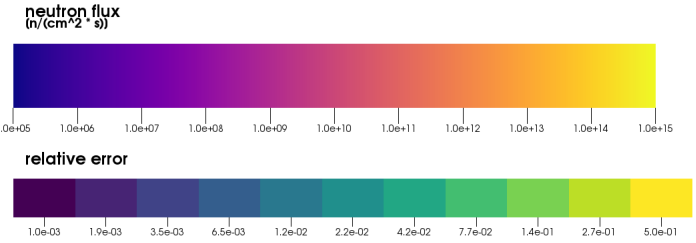

Figure 9.15: Neutron flux distribution and corresponding relative error at $x = 0$, $E_n = 25$ MeV - 2 GeV

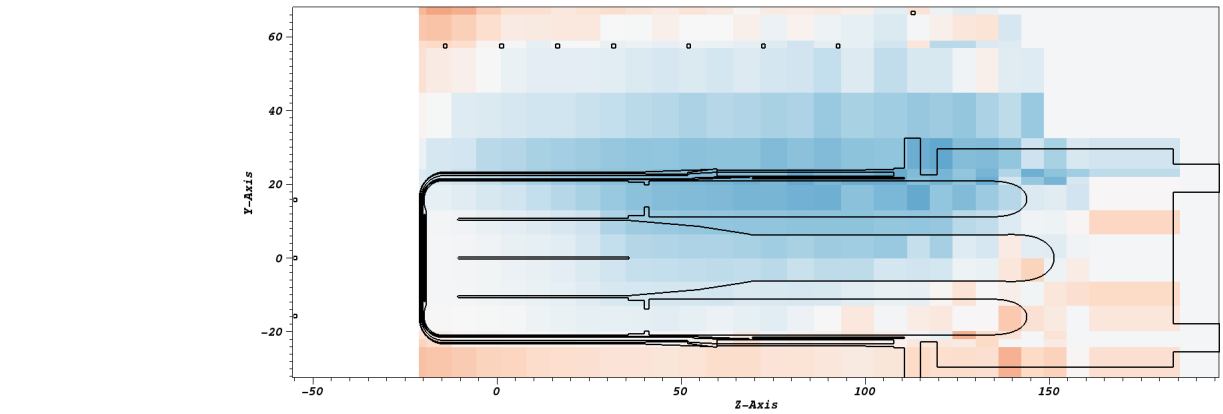

(a) Spatial distribution at $x = 0$, $E = 20$ - 25 MeV

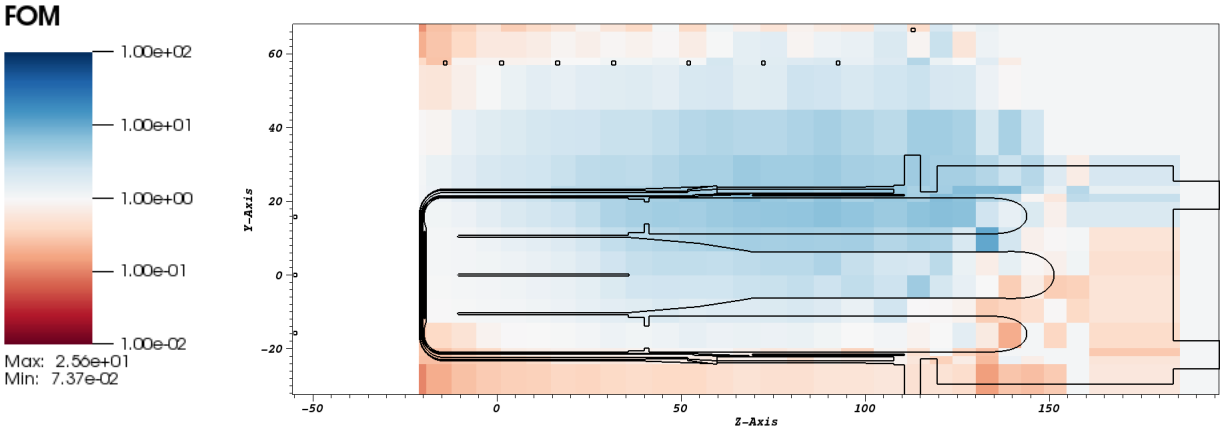

(b) Spatial distribution at $x = 0$, $E = 25$ - 30 MeV

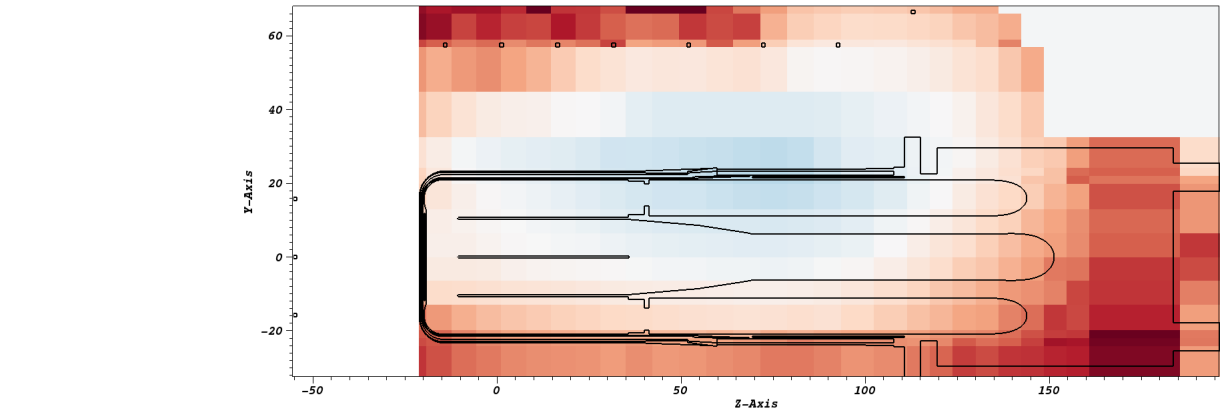

(c) Spatial distribution at $x = 0$, $E = total$

Figure 9.16: Figure of merit ratio (high-energy GT-CADIS / analog)

These figures show that minimal changes to the photon SDR are seen when high-energy GT-CADIS are applied to this problem. A similar trend is seen for the SDR at the detectors. These SDR at each of the 11 detectors for experimental, analog - neutron source, analog -

proton source, high-energy GT-CADIS - neutron source and high-energy GT-CADIS - proton source are shown in Figure 9.18. The experimental results were obtained from Popova et al. [6]. The ratio between each run and the experimental results are shown in Figure 9.19. All the ratios show a similar trend. The detectors close to the front of the target geometry, therefore closest to the source, are overestimated by around 40%. This decreases significantly for the detector at the back of the geometry, with ratios as low as 0.3.

If the experimental results are taken as the true results, then the high-energy GT-CADIS was unable to improve the SDR at the detectors at the back. Even when compared to analog, there is only a slight improvement in the neutron transport. There are a few likely reasons for this trend. The first likely explanation is that GT-CADIS is not the best suitable to improve a mesh tally. The second likely explanation is that this particular demonstration problem does not gain much from the use of VR parameters due to having sufficient scoring near the detectors and in regions important to the SDR at these detectors.

It is still important to note that the use of high-energy GT-CADIS VR parameters does increase the FOM when compared to an analog run. The increases in important regions are up to 25 time greater than the FOM from analog transport.

9.5 Conclusion

In this chapter, the high-energy GT-CADIS workflow is applied to a realistic problem. The problem consisted of generating VR parameters to optimize for detectors placed at a removed SNS target assembly. The final SDR at the 11 detectors were compared with experimental results. A total of four R2S calculations were set up. Two were analog with neutron source and proton source, and two were high-energy GT-CADIS with neutron source and proton source. The final SDR is compared with the experimental results, and most were overestimated or underestimated. Detectors 1 - 3 show some differences between the runs with a neutron source and a proton source. These differences are due to the neutron source being

approximated from the proton source. There are no significant differences in the SDR at detectors 4 - 11 for any of the runs. The application of high-energy GT-CADIS VR parameters does speed up the neutron transport. This was shown by the FOM increasing by up to 25% in important regions when compared to the FOM of the analog transport run.

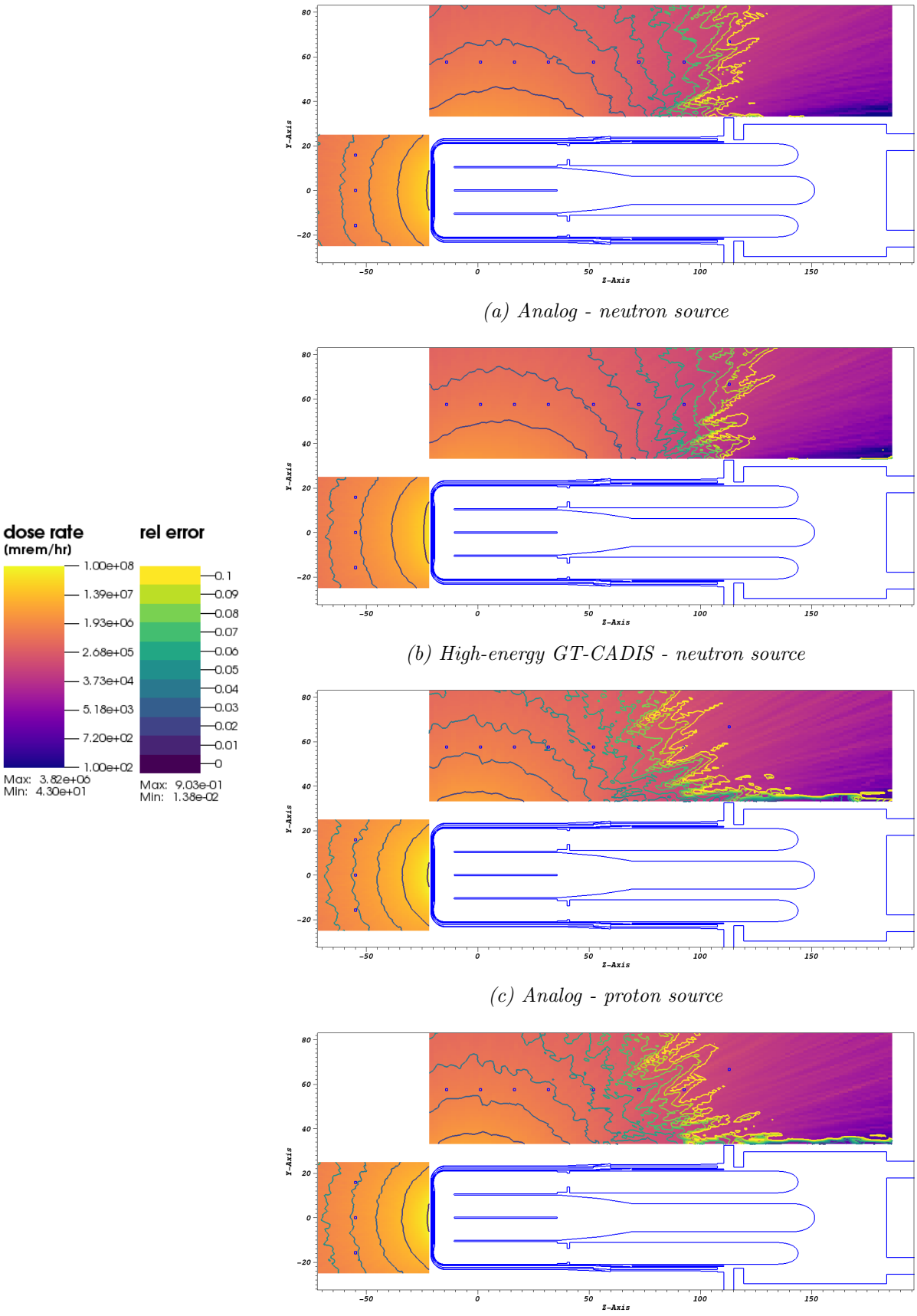

(a) Analog - neutron source

(b) High-energy GT-CADIS - neutron source

(c) Analog - proton source

(d) High-energy GT-CADIS - proton source

Figure 9.17: Photon dose rate distribution and corresponding relative error at $x = 0$

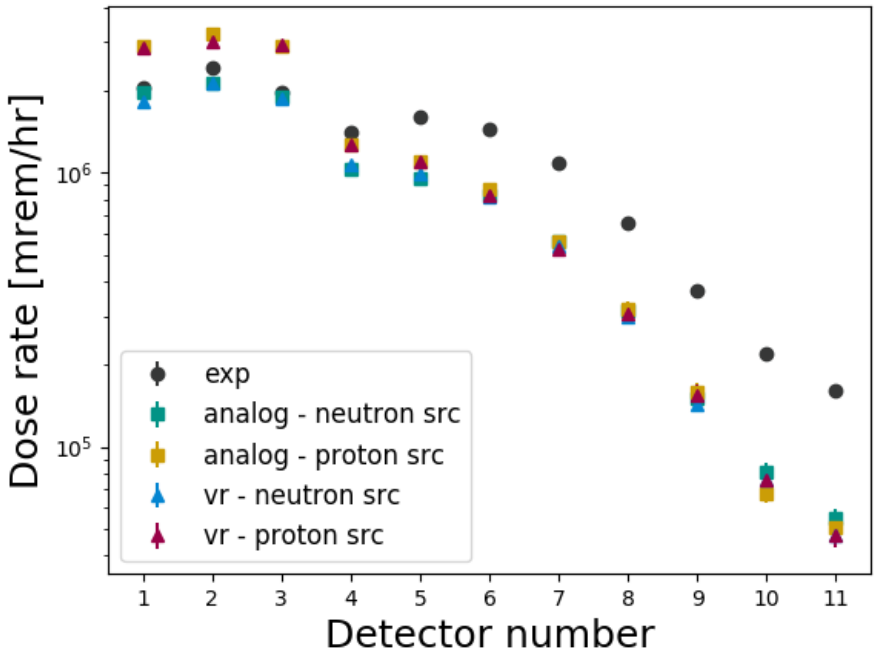

Figure 9.18: SDR at detectors

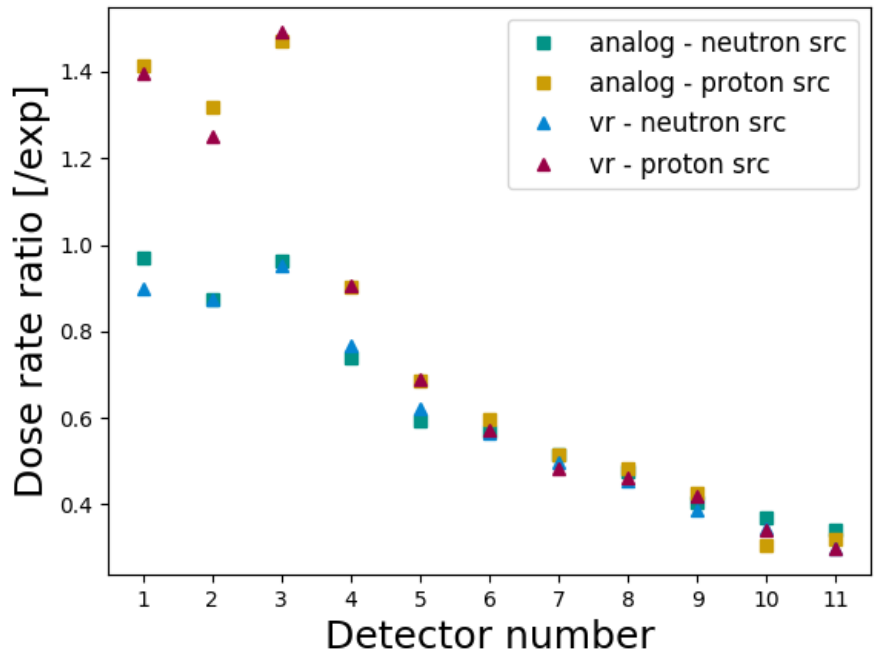

Figure 9.19: Ratio of SDR (Simulation/Experimental)

Chapter 10

Conclusion and Future Work

An implementation of the MS-CADIS method for optimizing the primary MC transport for SDR analysis for accelerator-driven systems has been investigated in this work. The MS-CADIS method provides a path to optimize the primary transport of a multi-step transport. MS-CADIS poses that an adjoint neutron source can be formulated if a quantity $T(E_n, E_p)$, which relates the neutron flux to the photon emission density, is calculated. GT-CADIS is an implementation of MS-CADIS for SDR and was implemented and validated for fusion systems. GT-CADIS provides a path to calculate $T(E_n, E_p)$ under mathematical approximations to linearize the neutron flux and photon emission density relationship.

This work starts by revisiting the MS-CADIS method to implement it and validate it for accelerator-driven systems. Chapter 4 revisits the path set forth by the original GT-CADIS implementation and expands the $T(E_n, E_p)$ equations to include the photon emission density contributions from the energy range outside cross-section libraries. This high-energy GT-CADIS implementation uses the same mathematical approximations as the original GT-CADIS to linearize the neutron flux and photon emission density relationship. These mathematical approximations lead to the SNILB criteria, which is validated for accelerator-driven systems in Chapter 6.

Chapter 6 shows that the SNILB criteria are reasonably met for materials typical of accelerator-driven systems and for a range of irradiation/decay scenarios. There are some instances where the SNILB criteria are violated for high or low irradiation times. With the simple problem used in Chapter 6, most of the violations were not of high significance. Although Chapter 6 showed that the SNILB are met for materials typical of accelerator-

driven systems, it is recommended that the SNILB criteria be evaluated for each problem to assess the efficacy of high-energy GT-CADIS for that specific problem.

In Chapter 7, a simple problem was designed to demonstrate the implementation of the high-energy GT-CADIS and compare it to an analog run and to an implementation of GT-CADIS for neutrons of energy less than 25 MeV. Chapter 7 showed that using VR parameters generated with high-energy GT-CADIS had significant improvements on the final SDR response when compared to an analog run. It also showed that applying GT-CADIS to neutrons of energies below 25 MeV had significant challenges. The first challenge is that the approximation of the response is not complete when using cross-section libraries up to 25 MeV. This leads to the weight window lower bounds being lower than expected. A smaller weight window causes particles to split multiple times, increasing the transport time and potentially preventing the transport from finishing within a reasonable time. In order to further explore this route, the full response approximation was provided, and the weight window lower bounds for energy regions above 25 MeV were set to zero. This allowed the transport to finish, and the SDR calculated with this method showed little improvement when compared to the analog run. Missing the VR for the high-energy neutrons significantly impacted the photon dose rate generated.

Chapter 8 explored the performance of the high-energy GT-CADIS method. High-energy GT-CADIS VR parameters were generated and used in the neutron transport run. The neutron transport was performed for four different processor times and repeated ten times to obtain a mean and a standard deviation. These run trials were done for both the analog and the high-energy GT-CADIS transport. The neutron flux and radionuclide production rates were used in a simple activation calculation to generate the photon emission rates. These photon emission rates were used alongside the adjoint photon flux to obtain the SDR at a detector. The neutron transport calculation with high-energy GT-CADIS showed result convergence even at the lowest processor time. In contrast, the analog transport calculation showed that even at the highest processor times, the back of the geometry had no tally scores.

This is further shown in the SDR results. The FOM was also calculated for both methods, and it showed that at the two highest processor times, the use of high-energy GT-CADIS resulted in a speed-up of 10^7 when compared to the analog run.

Chapter 9 explored the application of high-energy GT-CADIS on a full production problem. The SDR was calculated at several detectors placed around an out-of-service SNS target assembly. The SDR results were compared to experimental results and to four different transport runs. Two were analog runs with a proton source and with a neutron source, respectively. The other two were with high-energy GT-CADIS and a proton source and a neutron source, respectively. The SDR results of the numerical experiments showed only slight differences. The FOM for the high-energy GT-CADIS transport runs showed an increase in FOM in the important regions of up to 25% compared to the analog transport.

These numerical experiments showed a few places where future work is needed to improve the application of high-energy GT-CADIS. In the accelerator-driven system shown in Chapter 9, the original source is a proton source. The current implementation of CADIS is not able to generate VR parameters to optimize the protons for a SDR calculation. Another place of interest is in expanding this application to global VR like the FW-CADIS implementation.

In this work, it is demonstrated that the MS-CADIS implementation of high-energy GT-CADIS is applicable for accelerator-driven systems. The use of high-energy GT-CADIS VR parameters will result in a significant reduction of computational resources to calculate the SDR in accelerator-driven systems.

Bibliography

[1] Y. Chen and U. Fischer, "Rigorous MCNP based shutdown dose rate calculations: Computational scheme, verification calculations and applicaion to ITER," *Fusion Engineering and Design*, , *63*, 107 (2002).

[2] M. Wohlmuther, F. X. Gallmeier, and M. Brigger, "Activation of Trace Elements and Impurities: A New Ansatz for Monte Carlo Calculations," *Nuclear Technology*, **168**, *3*, 685 (2009).

[3] J. C. Wagner and A. Haghighat, "Automated Variance Reduction of Monte Carlo Shielding Calculations Using the Discrete Ordinates Adjoint Function," *Nuclear Science and Engineering*, , *128*, 186 (1998).

[4] A. M. Ibrahim, D. E. Peplow, R. E. Grove, and S. R. Johnson, "The multi-step CADIS Method for shutdown dose rate calculations and uncertainty propagation," *Nuclear Technology*, **196**, 286 (2015).

[5] E. D. Biondo and P. P. H. Wilson, "Transmutation Approximations for the Application of Hybrid Monte Carlo/Deterministic Neutron Transport to Shutdown Dose Rate Analysis," *Nuclear Science and Engineering*, **187**, 27 (2017).

[6] I. Popova, F. Gallmeier, S. Trotter, and M. Dayton, "Calculations vs. measurements of remnant dose rates for SNS spent structures," *Journal of Physics: Conference Series*, **1046**, 012013 (2018); 10.1088/1742-6596/1046/1/012013.

[7] E. E. Lewis and W. F. Miller, *Computational Methods of Neutron Transport*, Wiley-Interscience (1993).

[8] A. Haghighat and J. C. Wagner, "Monte Carlo variance reduction with deterministic importance functions," *Progress in Nuclear Technology*, **42**, *3*, 25 (2003).

[9] M. C. Team, *MCNP User's Manual: Code Version 6.1*, Los Alamos National Laboratory, manual rev. 0 ed. (2013).

[10] T. J. Tautges, P. P. Wilson, J. Kraftcheck, B. M. Smith, and D. L. Henderson, "Acceleration Techniques for Direct Use of CAD-Based Geometries in Monte Carlo Radiation Transport," *International Conference on Mathematics, Computational Methods and Reactor Physics*, American Nuclear Society, Saratoga Springs, NY (2009).

[11] G. J. Russell, "Spallation Physics - An Overview," *International Collaboration on Advanced Neutron Sources*, , *3*, 22 (1990).

[12] P. P. Wilson, "ALARA: Analytic and Laplacian Adaptive Radioactivity Analysis," (1999).

[13] W. B. Wilson, S. T. Cowell, T. R. England, A. C. Hayes, and P. Moller, *A Manual for CINDER'90*, Los Alamos National Laboratory, 07th ed. (2008).

[14] R. A. Forrest and M. R. Gilbert, *FISPACT-2005: User manual*, UKAEA FUS 514, EURATOM/UKAEA (2005).

[15] C. Petrovich, *SP-FISPACT2001: A Computer Code for Activation and Decay Calculations for Intermediate Energies. A connection of FISPACT with MCNPX*, ENEA (2001).

[16] F. Achison and H. Schaal, *ORIHET3-Version 1.12, A Guide for Users*, PSI (2003).

[17] F. X. Gallmeier and I. Remec, "The Radiation Environment for the Change-out Scenarios of the SNS Inner Plug and the Proton Beam Window Insert," *Accelerator Applications in Nuclear Renaissance* (2003).

[18] F. X. Gallmeier and M. Wohlmuther, "AARE ACTIVATION SCRIPT VERSION 2.0 USER GUIDE," (2018).

[19] X.-. M. C. Team, *A General Monte Carlo N-Particle Transport Code, Version 5: Volume I: Overview and Theory*, Los Alamos National Laboratory, manual rev. 5 ed. (2003).

[20] A. D. M. Harb and P. P. H. Wilson, "Uncertainty Quantification of the Decay Gamma Source in Mesh-Based Shutdown Dose Rate Calculations," *Fusion Science and Technology*, **79**, *1*, 1 (2023); 10.1080/15361055.2022.2115831., URL `https://doi.org/10.1080/15361055.2022.2115831`.

[21] M. Majerle, D. Leichtle, U. Fischer, and A. Serikov, "Verification and validation of the R2Smesh approach for the calculation of high resolution shutdown dose rate distributions," *Fusion Engineering and Design*, **87**, 443 (2012); https://doi.org/10.1016/j.fusengdes.2011.12.010.

[22] T. U. C. Team, "DAGMC: Direct Accelerated Geometry Monte Carlo," `https://svalinn.github.io/DAGMC/` (2021).

[23] PyNE Development Team, "PyNE: The Nuclear Engineering Toolkit," `http://pyne.io` (2011-2019).

[24] Popova, Irina, "Flux to Dose Conversion Factors," *SNS-NFDD-NSD-TR-0001-R00* (2009).

[25] T. M. Miller, D. D. DiJulio, and V. Santoro, "Application of ADVANTG Variance Reduction Parameters with MCNP6 at ESS," *Journal of Neutron Research*, **22**, 199 (2020); 10.3233/JNR-200158.

[26] S. W. Mosher, S. R. Johnson, A. M. Bevill, A. M. Ibrahim, C. R. Daily, T. M. Evans, J. C. Wagner, J. O. Johnson, and R. E. Grove, *ADVANTG—An Automated Variance Reduction Parameter Generator*, Oak Ridge National Laboratory, manual rev. 1 ed. (2015).

[27] R. A. Lillie and F. X. Gallmeier, "HILO2K: A Coupled Neutron-Photon Transport Cross-Section Library for Neutron Energies Up to 2000 MeV," (2000).